

# Applications of Principal Component Analysis for Position-Sensitive Semiconductor Detectors

by

Bennett Williams

A dissertation submitted in partial fulfillment  
of the requirements for the degree of  
Doctor of Philosophy  
(Nuclear Engineering and Radiological Sciences)  
in The University of Michigan  
2019

Doctoral Committee:

Professor Zhong He, Chair  
Professor Jeffrey Fessler  
Professor David Wehe  
Research Scientist Yuefeng Zhu

Bennett Williams

btwill@umich.edu

ORCID iD: 0000-0002-8986-6171

© Bennett Williams 2019

All Rights Reserved

## ACKNOWLEDGEMENTS

I owe a great deal of gratitude towards my advisor, Prof. Zhong He, who was willing to give me the latitude to explore concepts and ideas that traditionally fall outside of the scope of the research in the Orion Measurements Group. He was a constant source of motivation throughout the work in this dissertation, and his contributions to this work are greatly appreciated. I would also like to express my gratitude to Prof. Jeffrey Fessler, Prof. David Wehe and Dr. Yuefeng Zhu for serving on my dissertation committee. Their feedback and insight were invaluable to this work.

Members of the Orion Measurements Group - past and present - also contributed significantly to this work. Much of the work in this dissertation was made possible by the technological development and innovation from previous members, and collaboration with current members was essential for my work. In particular, I would like to recognize the contributions of Dr. David Goodman and Jiawei Xia. They were always willing to lend a critical ear for new ideas, and I value the camaraderie that we developed in our time with the Orion Measurements Group. I would also like to thank those who played a role in proofreading this work: Daniel Shy, Zhuo Chen and Matthew Petryk.

# TABLE OF CONTENTS

<b>ACKNOWLEDGEMENTS</b> . . . . .	ii
<b>LIST OF FIGURES</b> . . . . .	v
<b>LIST OF TABLES</b> . . . . .	xii
<b>LIST OF ABBREVIATIONS</b> . . . . .	xiii
<b>ABSTRACT</b> . . . . .	xv
<b>CHAPTER</b>	
<b>I. Introduction</b> . . . . .	1
1.1 Emergence of Nuclear Safeguards . . . . .	1
1.2 The Role of Gamma-Ray Spectroscopy in Nuclear Safeguards	2
1.3 Development of Position-Sensitive Semiconductor Detectors .	5
1.4 Novel Contributions to Position-Sensitive Semiconductor De-	
tector Technology . . . . .	7
<b>II. Overview of Detection and Data Acquisition Systems</b> . . . . .	10
2.1 Characteristics of Cadmium Zinc Telluride Detectors . . . . .	10
2.2 The Shockley-Ramo Theorem . . . . .	13
2.3 Data Acquisition . . . . .	22
2.4 Event Reconstruction . . . . .	25
2.4.1 Depth of Interaction and Energy Reconstruction . .	26
2.4.2 Lateral Position Reconstruction . . . . .	29
2.4.3 Reconstruction of Multiple-Pixel Events . . . . .	32
2.4.4 Reconstruction by System Response Function . . . . .	36
2.4.5 Subpixel Energy Calibration . . . . .	41
<b>III. Principal Component Analysis Methodology</b> . . . . .	43

3.1	Principal Component Analysis Theory . . . . .	44
3.2	Interpretation of Principal Components . . . . .	50
<b>IV. Energy Reconstruction by Principal Component Regression</b>		<b>54</b>
4.1	Data Preprocessing . . . . .	55
4.2	Principal Component Regression . . . . .	58
4.3	Results for Single-Pixel Events . . . . .	62
4.3.1	Selection of the Number of Principal Components . . . . .	69
4.3.2	Sensitivity to Statistical and Electronic Noise . . . . .	72
4.3.3	Comparison to Sub-Pixel Energy Calibrations . . . . .	74
4.3.4	Event Processing Time . . . . .	76
4.3.5	Adaptations for Different Incident Gamma-Ray Energy . . . . .	78
4.4	Supervised Principal Component Analysis . . . . .	81
<b>V. Adaptations for Principal Component Regression for Multiple-Pixel Events</b>		<b>90</b>
5.1	Adaptations for Multiple-Pixel Events . . . . .	91
5.2	Categorization of Two-Pixel Events . . . . .	95
5.3	Results for Two-Pixel Events . . . . .	101
5.4	Processing Time . . . . .	105
5.5	Generalization for All Multiple-Pixel Events . . . . .	106
<b>VI. Adaptations for Principal Component Regression for High-Energy Events</b>		<b>114</b>
6.1	Challenges Unique to High-Energy Events . . . . .	118
6.2	Principal Component Regression for Single-Pixel Events . . . . .	120
6.3	Principal Component Regression for Multiple-Pixel Results . . . . .	129
<b>VII. Summary and Future Work</b>		<b>132</b>
7.1	Summary . . . . .	132
7.2	Future Work . . . . .	134
<b>BIBLIOGRAPHY</b>		<b>137</b>

## LIST OF FIGURES

### Figure

2.1	Two $20 \times 20 \times 15$ mm <sup>3</sup> Redlen detectors directly coupled to ASICs.	13
2.2	Cathode weighting potential as a function of the depth of interaction and the corresponding change in weighting potential for two hypothetical interactions. . . . .	19
2.3	Collecting pixel weighting potential as a function of depth (right) for the highlighted region in the virtual detector volume (left). . . . .	21
2.4	Weighting potential as a function of position for a slice in the middle of the pixelated detector when charge carriers drift from the red to green dots (right) and the corresponding detector slice in the detector (left). The weighting potential profile in the $x - z$ plane corresponds to the solid, blue portion of the detector in the left pane. . . . .	22
2.5	Diagram of a basic charge-sensitive amplifier used for amplifying the induced charge on an electrode. . . . .	23
2.6	Measured data acquisition dead time as function of the number of digitized waveforms per event for two modes of operation. . . . .	24
2.7	Digitized signals for a generic single-pixel event under trigger +4 mode.	25
2.8	<sup>137</sup> Cs photopeak amplitude for an anode pixel as function of depth from the anode (top) and the corresponding CAR as a function of depth. . . . .	27
2.9	Energy spectrum obtained before (top) and after (bottom) applying depth corrections to data collected from a <sup>137</sup> Cs exposure. . . . .	28

2.10	Generic waveforms for a single-pixel, 662 keV event and the associated drift times for an anode-side interaction (top) and a cathode-side interaction (bottom). . . . .	30
2.11	Array of pixels (triggering pixel in the center surrounded by cardinal neighbors) and the signals induced for interactions in which the position is near the left and right pixel boundaries. . . . .	31
2.12	Weighting potential profile for an event in which a charge carrier is collected by the center pixel. . . . .	33
2.13	Anode and cathode signal waveforms for a two-pixel event with non-neighboring triggered pixels (top) and neighboring triggered pixels (bottom). . . . .	33
2.14	Photopeak centroid of two-pixel events at various degrees of separation between triggering pixels for a $^{137}\text{Cs}$ exposure. . . . .	34
2.15	Two-pixel, side-neighbor event energy as a function of the energy ratio. . . . .	36
2.16	Raw and filtered waveforms for a generic single-pixel event. . . . .	37
2.17	SRF for a generic anode channel (top) and the corresponding cathode SRF (bottom). . . . .	38
2.18	Difference in single-pixel event depth estimated by SRF and CAR for various energy ranges. . . . .	40
2.19	Single-pixel energy resolution at 662 keV, expressed in FWHM, as a function of the pixel location for traditional energy calibration (left) and subpixel energy calibration (right). . . . .	42
3.1	Generic neighbor pixel waveform for a single-pixel event. . . . .	45
3.2	Reconstructed depth of interaction as a function of the first principal component obtained from the decomposition of single-pixel event data from a generic anode pixel. . . . .	51
3.3	Eigenvector that maps data to the first principal eigenvector (top) and a sample data vector for juxtaposition (bottom). . . . .	52
3.4	Waveform vectors with excessively low and high first principal component scores (top) and the eigenvector responsible for the projections (bottom). . . . .	53

4.1	Normalized, collecting pixel waveforms as they are acquired (top) and the aligned waveforms used for PCA (bottom). . . . .	58
4.2	Correlation between reconstructed energy and the first principal component for all events (top) and for a specific depth bin near the anode surface (bottom). . . . .	59
4.3	Linear regression of energy and principal component correlation with apparent data outliers. . . . .	60
4.4	Correlation between the energy deposition estimate and principal component before (top-left with the corresponding histogram in the top-right) and after (bottom-left with the corresponding histogram in the bottom-right) projecting the data long the regressed trends. . . . .	61
4.5	Updated energy estimates as a function of the first three principal components after regressing and projecting along each systematic trend. . . . .	62
4.6	Single-pixel FWHM observed at 662 keV for each anode pixel using conventional energy reconstruction methods (left) and the FWHM after updating energy estimates according to principal component correlations (right). . . . .	63
4.7	Single-pixel FWTM observed at 662 keV for each anode pixel using conventional energy reconstruction methods (left) and the FWTM after updating energy estimates according to principal component correlations (right). . . . .	64
4.8	First five eigenvectors for an interior pixel (top) and a corner pixel (bottom). . . . .	65
4.9	Waveform vectors with excessively high and low fifth principal components for an interior pixel (top) and the corresponding eigenvector (bottom). . . . .	66
4.10	Energy resolution improvement at 662 keV for exterior and interior pixels with respect to FWHM (top) and FWTM (bottom). . . . .	67
4.11	Aggregate single-pixel event energy spectrum obtained before and after principal component regressions (left) and the pixel-specific improvements for the original and corrected energy spectra (right). . . . .	68
4.12	Cumulative explained variance of single-pixel events as a function of principal component for two anode pixels. . . . .	70

4.13	Single-pixel energy resolution metrics as a function of the number of principal component corrections. Asymptotic values are indicated by dotted lines. . . . .	70
4.14	Single-pixel FWHM as a function of pixel location obtained by sub-pixel energy calibration (left) and PCA (right). . . . .	75
4.15	Single-pixel event processing-time distributions for various reconstruction methods. . . . .	78
4.16	Processed BeRP ball spectrum obtained with PCA and SRF for the energy ranges of 300 - 450 keV (left) and 550 - 750 keV (right). . . .	80
4.17	Energy resolution as a function of incident gamma-ray energy for PCA and SRF as measured by FWHM (top) and FWTM (bottom). . . . .	81
4.18	First three eigenvectors for events collected by a single, interior pixel using unconstrained PCA (top) and the using the constrained method described in Bair et al. (bottom). . . . .	84
4.19	Comparison of the $p$ values obtained from regressions based on the unconstrained and constrained principal components as a function of the depth bin containing the corresponding events. . . . .	85
4.20	Aggregate, single-pixel energy spectrum obtained using unconstrained and constrained PCA. . . . .	86
4.21	Eigenvectors for the first three principal components obtained by unconstrained PCA (top) and Barshan's method (bottom). . . . .	88
4.22	Single-pixel energy spectra for unconstrained PCA and principal component regression via Barshan's method. . . . .	89
5.1	Sample, two-pixel observation annotated with the corresponding pixel descriptions. . . . .	91
5.2	Sample, two-pixel observation configured with a single time offset determined by the primary pixel signal (blue) and separate time offsets determined for each collecting pixel signal separately (red). . . . .	93
5.3	Difference in reconstructed depth for interactions in non-neighboring, two-pixel events as a function of the second principal component when using a single offset computed from the primary pixel signal (top) and using two, pixel-specific offsets (bottom). . . . .	94

5.4	Energy ratio as a function of the second principal component for side-neighbor events for a given primary pixel. . . . .	95
5.5	Combined, reconstructed energy of two-pixel events as a function of the first principal component for a given primary pixel. . . . .	96
5.6	Combined energy for events of a given primary pixel as a function of the first principal component for neighboring events (top) and non-neighboring events (bottom). . . . .	97
5.7	Distributions of the primary pixel depth of interaction (top-left), depth difference (top-right), lateral separation (bottom-left) and energy ratio (bottom-right) for non-neighboring, two-pixel events recorded for a single primary pixel. . . . .	98
5.8	Spearman rank correlations for principal component regressions of non-neighboring events divided by the primary pixel depth (left) and lateral separation (right). . . . .	99
5.9	Principal component regressions for three regimes of lateral separation of non-neighboring, two-pixel events for a primary pixel. . . . .	99
5.10	Spearman rank correlations for principal component regressions of neighboring events divided by the primary pixel depth (left) and energy ratio (right). . . . .	100
5.11	Principal component regressions for three regimes of energy ratio of neighboring two-pixel events for a primary pixel. . . . .	101
5.12	Processed, two-pixel energy spectra as a function of the number of applied principal component corrections. . . . .	102
5.13	Two-pixel energy spectra of a $^{137}\text{Cs}$ exposure processed by trapezoidal filtering, SRF and PCA reconstructions techniques. . . . .	103
5.14	Neighboring, two-pixel event energy resolution for each primary pixel as a function of its physical location for SRF (left) and PCA (right). . . . .	103
5.15	Neighboring, two-pixel event energy resolution for each primary pixel for PCA as a function of the resolution obtained by SRF. . . . .	104
5.16	Processing time distribution for two-pixel events under various reconstruction methods. . . . .	106

5.17	Comparison of three-pixel (top) and four-pixel (bottom) energy spectra for a $^{137}\text{Cs}$ exposure processed via trapezoidal filtering, SRF and the PCA methodology. . . . .	110
5.18	Raw waveforms acquired for a generic two-pixel event (top) and the corresponding, filtered waveforms used in calculating the trigger times (bottom). The trigger times are indicated by the dashed, vertical lines. . . . .	111
5.19	Distribution of energy deposited in individual pixels for $^{137}\text{Cs}$ photopeak events resulting in three-pixel events (top) and four-pixel events (bottom). . . . .	112
5.20	Observed, four-pixel energy resolution at 662 keV as a function of a low-energy threshold for trapezoidal filtering, SRF, and PCA reconstruction methods. Events that contain individual interactions with energy deposition below the threshold are removed and excluded from the energy resolution calculation. . . . .	113
6.1	Differential nonlinearity for reconstructed, single-pixel photopeak centroids as a function of incident gamma-ray energy for various reconstruction methods. . . . .	116
6.2	Single-pixel energy resolution as a function of incident gamma-ray energy obtained with PCA reconstruction. . . . .	117
6.3	Simulated interactions in which 500 keV (left) and 3000 keV (right) are deposited in a CdZnTe detector. The location and size of the circles indicate the location and the relative magnitude of the energy deposition, respectively. . . . .	120
6.4	Model of nonlinearity derived from the observed photopeak centroids (top) in the spectrum of single-pixel events collected by a single anode pixel (bottom). . . . .	122
6.5	Distribution of gain-corrected energy estimates produced from $1 \times 10^4$ realization of the $^{228}\text{Th}$ spectrum for various gamma-ray energies. . . . .	123
6.6	Single-pixel energy resolution as a function of incident gamma-ray energy for SRF and PCA with and without gain corrections. . . . .	124

6.7	Distribution of single-pixel energy resolution achieved by SRF and principal component regression before the application of nonlinearity compensation. The top pane displays the distribution for 860 keV photopeaks, whereas the bottom pane contains the distribution for the 1592 keV single-escape peak. . . . .	125
6.8	Gain-compensated, reconstructed energy of single-pixel, 2614 keV interactions as a function of depth for a single channel. . . . .	126
6.9	Comparison of eigenvectors generated from $^{137}\text{Cs}$ data and high-energy data for the first three principal components for an anode pixel. The first, second and third principal component eigenvectors are featured in the top, middle and bottom panes, respectively. The vertical, dotted lines separate the signals obtained from the collecting anode pixel, cathode and four neighbor pixels adjacent to the collecting pixel. . . . .	127
6.10	Single-pixel energy resolution as a function of incident gamma-ray energy for principal component regression with standard and high-energy principal components. . . . .	129
6.11	Two-pixel energy resolution as a function of incident gamma-ray energy for SRF and PCA. . . . .	130
6.12	Two-pixel energy resolution as a function of incident gamma-ray energy for PCA with a variety of modifications. . . . .	131

## LIST OF TABLES

### Table

4.1	Comparison of single-pixel event eigenvalues normalized to data vector length with and without the cathode signal included . . . . .	56
4.2	Single-pixel energy resolution at 662 keV for self-calibrated data and cross-validation results . . . . .	72
4.3	Summary of single-pixel energy resolution as a function of the events used for principal component regression . . . . .	73
4.4	Summary of single-pixel energy resolution as a function of the electronic noise added to the response variable . . . . .	74
6.1	Observed, single-pixel photopeak centroids as a function of incident gamma-ray energy as reconstructed by PCA, SRF and trapezoidal filtering . . . . .	115

## LIST OF ABBREVIATIONS

<b>NORM</b>	naturally occurring radioactive material
<b>HPGe</b>	high-purity germanium
<b>SNM</b>	special nuclear material
<b>CdZnTe</b>	cadmium zinc telluride
<b>HEU</b>	highly enriched uranium
<b>DU</b>	depleted uranium
<b>SPECT</b>	single-photon emission computed tomography
<b>PCA</b>	principal component analysis
<b>ASIC</b>	application-specific integrated circuit
<b>FWHM</b>	full width at half maximum
<b>FWTM</b>	full width at tenth maximum
<b>CAR</b>	cathode-to-anode amplitude ratio
<b>ADC</b>	analog-to-digital converter
<b>SRF</b>	system response functions
<b>WPCT</b>	weighting potential crosstalk
<b>LMA</b>	Levenberg-Marquardt algorithm
<b>SVD</b>	singular value decomposition
<b>SPCA</b>	supervised principal component analysis
<b>RAM</b>	random-access memory
<b>OLS</b>	ordinary least squares

**FFTW** Fastest Fourier Transform in the West

**MKL** Math Kernel Library

**HSIC** Hilbert Schmidt independence criterion

**RKHS** reproducing kernel Hilbert space

**ICA** independent component analysis

**PGAA** neutron-capture prompt gamma-ray activation analysis

**IDEAS** Integrated Detector Electronics AS

**INL** Idaho National Laboratory

## ABSTRACT

Although the landscape of nuclear safeguards changes as new technologies emerge, gamma-ray spectroscopy remains a fundamental component of nuclear material detection and monitoring protocols. Systems that feature pixelated, large-volume CdZnTe detectors provide a viable option for gamma-ray spectrometers owing to their portability, room-temperature operation, imaging capabilities and high-performance energy resolution. Despite recent advances in data acquisition technology, CdZnTe detector systems fail to achieve comparable energy resolution to the industry-leading performance provided by high-purity germanium detectors. This limits the utility of CdZnTe systems in gamma-ray spectroscopy, as the confidence intervals of analyses pertinent to nuclear safeguards depend heavily on energy resolution.

In order to address this deficiency in CdZnTe detector technology, a fundamentally new approach for calibrating energy is proposed. Conventional calibration methods for position-sensitive semiconductor detectors rely heavily on theoretical models. Despite years of extensive study on charge transport properties in position-sensitive semiconductor detectors, the underlying models introduce systematic error in the energy reconstruction process. Under the proposed framework, predictive models are constructed via principal component analysis in an attempt to reduce the reliance on theoretical models and human intuition.

This work provides a practitioner's account of how one can leverage information extracted by principal component analysis to improve energy resolution for position-sensitive semiconductor detectors. This methodology is adapted to address unique challenges presented by a variety of events observed in position-sensitive detectors.

For the detectors used in this work, single-pixel, two-pixel and three-pixel event energy resolution at 662 keV improve by approximately 10% relative to the leading alternative. The proposed calibration procedure is generalized to accommodate event reconstruction for gamma-rays in the entire dynamic range.

Energy calibration via principal component analysis is intended to provide a practical alternative to conventional techniques. Calibration requirements and computational time are monitored closely to ensure that the application of the proposed technique does not become overly burdensome. Calibration measurements based on principal component analysis require no more time or data than conventional methods. The processing time per detection event is significantly reduced compared to computationally-intensive alternatives under this framework, enabling the processing speed necessary for a wide variety of nuclear safeguards applications.

# CHAPTER I

## Introduction

### 1.1 Emergence of Nuclear Safeguards

The first nuclear tests conducted on July 16, 1945 in Alamogordo, NM marked a pivotal moment in the history of warfare and rapidly changed the strategic landscape. As Paul Kennedy writes in his expansive study *The Rise and Fall of the Great Powers*, the United States did not maintain a monopoly on nuclear weaponry long after the first tests in 1945 [1]. Soviet development of a nuclear arsenal quickly followed, and other European powers - namely Great Britain and France - went to great lengths to maintain pace in technological advancements of nuclear weaponry to compensate for relative deficiencies in population and manufacturing capabilities. This technology became a *de facto* prerequisite for aspiring world powers, or for those nations seeking to maintain status as a world power.

Throughout the remainder of the 20<sup>th</sup> century, global powers in the Cold War era maintained nuclear weapon capabilities primarily as a means of deterrence against threats from opposing states. Although much has changed in the international landscape since these developments, the strategy of obtaining global relevance by amassing nuclear arsenals continues into the 21<sup>st</sup> century, although not necessarily with the intent of strictly deterring states from acts of aggression. In 2007, former chairman of the Senate Armed Services Committee Sam Nunn, former United States Secre-

tary of Defense William Perry, and former United States Secretaries of State George Shultz and Henry Kissinger collectively suggested that the effectiveness of deterrence had diminished as previously non-nuclear states aggressively sought to gain nuclear weaponry [2]. In explicit references to the presiding regimes of North Korea and Iran, they argued that such states did not adhere to the constraints of deterrence and presented new challenges to national security. Among these challenges is the ability to ensure that non-state groups do not obtain nuclear weapons through illicit means. To this end, nuclear safeguards emerged as a means to maintain control of nuclear materials that could enhance the ability of non-compliant actors to achieve nuclear capabilities [3].

## **1.2 The Role of Gamma-Ray Spectroscopy in Nuclear Safeguards**

Nuclear safeguards describe the collective efforts to detect and/or prevent diversion of nuclear materials intended for such purposes. Radiation detection provides a valuable tool for these purposes. The nuclear materials in question emit gamma-ray radiation that is characteristic of material composition. If one is interested in characterizing material composition, it is not sufficient to merely detect the presence of radiation, but rather it is necessary to measure additional attributes about the emitted radiation. To distinguish illicit nuclear materials from innocuous sources or naturally occurring radioactive material (NORM), radiation detection systems ideally possess the ability to measure the energy of emitted gamma rays. Isotopes pertinent to the field of nuclear safeguards emit gamma-ray radiation of discrete and well-characterized energies that allow one to identify the isotope from which it was emitted. Several classes of radiation detectors provide such capabilities, but a select few provide the performance required to meet the demands of nuclear safeguards.

Detection system performance is evaluated by several considerations whose importance depend on specific applications. The analysis of gamma-ray energy spectra - widely referred to as gamma-ray spectroscopy (or informally as ‘gamma spectroscopy’) - relies heavily on the achievable energy resolution of a detector. The precision at which gamma-ray energy can be measured depends on the underlying mechanics of detection media for converting neutral radiation to detectable and sensible signals. Semiconductor detectors provide the optimal energy resolution among alternatives due to this consideration, whereas scintillator detectors require several conversion stages that cumulatively degrade energy resolution [4, 5]. Energy resolution becomes increasingly important for quantifying gamma-ray radiation energy in isotopes that emit several gamma rays of similar energies or materials that contain several isotopes [6, 7]. The inability to precisely measure gamma-ray energy may lead to inaccurate analyses.

Gamma-ray detectors are not only judged on the basis of energy resolution, but also by the rate at which gamma-ray radiation is detected. Gamma-ray detectors may excel at properly quantifying incident gamma-ray energy, but they must they do so efficiently to provide a significant degree of confidence in the ensuing analysis. Some applications of gamma-ray spectroscopy may be conducted in the presence of a source that emits relatively few gamma rays in a limited amount of time. In such applications, gamma-ray detectors must be able to detect and quantify a high fraction of the emitted gamma rays to reach a statistically-significant conclusion about the source.

To further complicate matters, measurements may be performed in an environment in which there are multiple sources of gamma-ray radiation. In such scenarios, it is beneficial to distinguish radiation by the source from which it was emitted [8, 9]. Radiation detectors do not inherently possess the capability to distinguish radiation in the spatial domain, but they can be configured to offer position sensitivity. If the

position at which gamma rays interact can be derived from the signals of a position-sensitive detector, algorithms based on Compton scattering kinematics, coded apertures or strategic attenuation may be performed to obtain an estimate of the spatial distributions of gamma-ray sources [10–13].

Other practical considerations such as cost and field-readiness factor into detector evaluation. The agencies and government entities that practice nuclear safeguards have finite resources to obtain and implement radiation detectors, and they must do so with cost in mind. Cost is ultimately determined by the price of the raw detection materials, associated data acquisition equipment, and the influence of patented technology. They must also consider the environments in which they perform measurements. For field applications where users must carry the detectors, instrument weight and size are important factors, and this often entails a trade-off with detection efficiency [14]. This may preclude the use of high-performance gamma spectrometers such as high-purity germanium (HPGe) detectors, which must operate with a source of external cooling.

Applications pertinent to nuclear safeguards often require gamma-ray spectroscopy. From the measured spectrum of gamma-ray energy, one can make inferences about sources of radiation from the intensity of select photopeaks. A popular method for estimating fissile content in uranium samples requires the ratio of peak intensities about the 186 and 1001 keV emissions from  $^{235}\text{U}$  and  $^{238}\text{U}$ , respectively [15]. In a similar fashion, relative intensities at characteristic, gamma-ray energies can provide valuable insight on the concentration of plutonium isotopes in a sample [16–18]. Peak ratios also help inspectors estimate spent nuclear fuel burnup in efforts to detect nuclear material diversion [19–21].

The uncertainty in peak intensity propagates to the key ratios in these analyses, and it is therefore crucial to use instruments with high-performance energy resolution and detection efficiency to reduce uncertainty in peak intensity. While peak

area uncertainty is sensitive to both of these factors, energy resolution influences the uncertainty more so than efficiency. Consider the tasks of estimating uranium enrichment and plutonium isotope concentrations of special nuclear material (SNM). Streicher et al. performed these estimations using 3-D, position-sensitive cadmium zinc telluride (CdZnTe) technology and a commercially available HPGe instrument with superior energy resolution [22]. Although the CdZnTe system is more efficient to low-energy emissions from uranium isotopes, the relative uncertainty in net count rate for the 186 keV emission is higher for the CdZnTe system (0.39% for 93% enriched highly enriched uranium (HEU) and 3.6% for 0.2% enriched depleted uranium (DU)) compared to that of an HPGe detector (0.28% and 1.3% for HEU and DU, respectively). The errors in the enrichment estimates reflect these results; the estimates obtained from CdZnTe system data reveal uncertainties of 0.02 and 10.1 weight percent for DU and HEU, respectively, whereas uncertainties of 0.01 and 2.5% weight percent were achieved with the HPGe detector. Such results provide unequivocal evidence of the importance of energy resolution for nuclear safeguards applications.

### **1.3 Development of Position-Sensitive Semiconductor Detectors**

Due to the influence of energy resolution in gamma spectroscopy, semiconductor detectors are the focus of the content in this thesis. Semiconductor detectors provide more desirable combinations of energy resolution and efficiency compared to alternative options such as scintillator devices and gaseous detectors. Due to the inherent advantages of these detectors, research and development of semiconductor detector technology remain active. The academic and scientific communities have collectively produced significant advancements to semiconductor technology in the years preceding this writing.

Although many applications require semiconductor detectors, there are select applications that require position-sensitive detector technology. Of note, position-sensitive devices have been developed for applications in ultra-high-resolution single-photon emission computed tomography (SPECT) [23–25] and single-polarity charge sensing devices. The latter refers to the development of systems that feature detection media with poor charge transport properties, which are presented in greater detail in Chapter II. This undesirable characteristic implies that the energy resolution compares unfavorably to materials with superior charge transport properties like HPGe. However, single-polarity charge sensing devices can be grown and fabricated in position-sensitive configurations suitable for imaging, and several materials under this classification can be operated at room temperature without the aid of external cooling. Furthermore, poor transport properties can be circumvented in position-sensitive devices to an extent. Given coordinates of a gamma-ray interaction, the position-specific response may be modeled with greater precision. In principle, these refined response models provide information that enhances spectral performance in detection media that were previously impeded by poor charge transport.

Research in this field has produced several iterations of position-sensitive designs for single-polarity charge sensing devices. Luke introduced the concept of coplanar grid for semiconductor detectors, which enabled estimation of the depth of interaction for gamma-ray interactions [26]. Subsequent developments of semiconductor detectors with strip electrodes provided the ability to estimate lateral position in addition to depth [27, 28]. Such configurations provided greater dimensionality to the system response model, but the resulting spectral performance was sensitive to the operating applied bias. Therefore, the implementation of strip electrodes were confined to thin detectors better suited for imaging applications rather than applications requiring high-performance energy resolution [29]. Detector electrode size was further reduced in pixelated anode designs. Interaction position could be estimated with greater

accuracy under this design, due in part to the favorable changes in detector weighting potential and the finer discretization of lateral dimensions [30, 31].

## 1.4 Novel Contributions to Position-Sensitive Semiconductor Detector Technology

The devices featured predominantly in this work contain pixelated anodes designed to achieve high-performance energy resolution and imaging capability. Although this configuration enables one to precisely model the position-specific response model in large-volume CdZnTe detectors, there is considerable room for improvement with regards to energy resolution. This criticism may seem overly disparaging considering the profound improvement in achievable energy resolution from the early inception of CdZnTe as a radiation detector to the recent work by Streicher et al. [22], but systematic error still pervades the estimation of gamma-ray energy deposition. Modern energy reconstruction techniques for position-sensitive CdZnTe detectors rely heavily on physics-based models. Even with the extensive work performed by groups from Brookhaven Radiation Detector Research and Development and this author's own affiliation, the Orion Radiation Measurement Group, there are limits to the understanding of complex charge transport processes in position-sensitive CdZnTe detectors. These limits prevent CdZnTe detector technology from achieving energy resolution predicted by semiconductor detector theory.

This work takes a fundamentally different approach to energy reconstruction that reduces the reliance on physics-based models. Instead, the methods presented in this work attempt to leverage signatures in digitized signals generated by CdZnTe detection events in hopes of estimating gamma-ray energy deposition more precisely. The method of choice makes judicious use of principal component analysis (PCA) to identify and quantify these signatures. It is not the intent of this author to completely

detach physical meaning from the energy reconstruction process. Ideally, one should be able to interpret the physical mechanisms represented by the products of the analysis. For this reason, PCA is chosen over alternative means of statistical analysis.

The proposed methods make practical use of PCA to construct predictive models for estimating energy deposition. It is applied towards a comprehensive set of gamma-ray event categories observed in pixelated CdZnTe detectors with the intent of mitigating systematic error that is otherwise neglected by conventional techniques. The PCA methodology is designed with the intent of providing a practical alternative to reconstruction methods suited for nuclear safeguards. This implies that the calibration process should not require excessive amounts of time and the algorithms used in the implementation of the PCA methodology should not be computationally intensive so that it becomes burdensome for field applications.

To properly contextualize this work, Chapter II provides a thorough description of the detection system used in these studies. It includes an overview of the CdZnTe detector technology, the underlying theory necessary to perform event reconstruction, and the conventional techniques developed by the Orion Radiation Measurement group to estimate gamma-ray interaction parameters. After the conceptual foundation for CdZnTe detector technology is established, the theory of PCA is provided in Chapter III. It emphasizes the application of PCA towards signals produced by CdZnTe devices, and it details the process by which physical processes are interpreted from the products of the analysis.

The construction of predictive models for energy reconstruction are further elaborated and demonstrated for the relatively simple single-pixel events in Chapter IV. Given the lack of complexity for single-pixel events, the content in Chapter IV serves as an effective tutorial for the data processing tasks, algorithms and practical considerations before advancing to more complex topics. Chapters V and VI elaborate the adaptations necessary to apply the PCA methodology towards multiple-pixel events

and high-energy events, respectively. They describe the unique challenges for these event categories and detail the steps taken to specifically address these concerns. Chapter VII concludes this work and proposes ways in which the PCA methodology could be further refined to address additional areas of the event reconstruction process for optimal performance.

## CHAPTER II

# Overview of Detection and Data Acquisition Systems

The overwhelming majority of the work described in this thesis was implemented and designed for use with pixelated CdZnTe detectors and the associated readout technology. These systems provide many of the ideal characteristics for gamma-ray spectrometers discussed in Section 1.2, and the underlying technology to support these systems has matured significantly over the past twenty years. A description of the components of the CdZnTe detector systems and data processing algorithms detailed in this chapter provide context for the work performed in subsequent chapters.

### 2.1 Characteristics of Cadmium Zinc Telluride Detectors

The detection material forms the foundation for gamma-ray spectrometers. It is responsible for converting neutral gamma-rays to a form of energy that can be readily sensed and quantified by readout technology. This conversion can be accomplished by many forms of gamma-ray interactions with matter; those most pertinent to gamma-ray spectroscopy are photoelectric absorption, Compton scattering and pair production.

CdZnTe belongs to a family of detection media formed by semiconductor materi-

als. It exists in the form  $\text{Cd}_{1-x}\text{Zn}_x\text{Te}$ , where  $x$  is a stoichiometric value between 0.04 and 0.2. Such materials are widely considered the preeminent choice for gamma-ray spectroscopy due in part to their ability to convert gamma-ray energy to quantifiable signals in the form of electron-hole pairs with a high degree of efficiency. The resulting statistical uncertainty in the amplitude of the signals generated by a gamma-ray interaction is lower than that of other forms of gamma-ray detection media like scintillators or gaseous detectors [32].

While semiconductor detectors benefit from the efficient conversion to electron-hole pairs, the band structure of these materials must not be too permissive. Otherwise, electron-hole pairs may be generated by an electron's inherent thermal energy. The signal generated by thermally excited electrons contributes to the underlying leakage current, and this form of noise hinders the ability to precisely measure the amplitude of the signal generated by a radiation interaction.

The degree to which a material prevents thermal excitation is inferred from the bandgap energy. Olego reported that CdZnTe can obtain a bandgap energy between 1.53 and 1.64 eV [33]. To put these values in context, insulating materials with negligible thermal excitation have bandgap energies in excess of 5 eV [4], and HPGe has a bandgap energy of 0.746 eV at 77 K [34].

HPGe detectors currently provide the best gamma-ray energy resolution. For gamma rays with an incident energy of 661.7 keV - an energy at which energy resolution is commonly measured and cited for semiconductor detectors - the achievable energy resolution is 0.13% full width at half maximum (FWHM) [35]. Granted, HPGe detectors must be operated at temperatures as low as 77 K to achieve high-performance energy resolution. During room-temperature operation, HPGe leakage current becomes excessive and severely degrades performance. CdZnTe detectors, however, achieve near-peak performance at room-temperature, as the bandgap energy remains sufficiently high to prevent excessive leakage current [36].

For the purposes of spectroscopy, semiconductor materials ideally have high charge carrier mobilities. In this context, the scalar mobility,  $\mu$ , describes a signal carrier's drift velocity,  $\mathbf{v}$ , in response to an electric field,  $\mathbf{E}$  (Equation 2.1).

$$\mathbf{v} = \mu\mathbf{E} \tag{2.1}$$

As explained in more detail in Section 2.2, the movement of carriers generates the signal from which energy deposition is estimated. Carriers drifting in materials with low mobility are more susceptible to trapping and recombination, two mechanisms by which signal carriers are stopped. The resulting reduction in the signal amplitude degrades estimates of the energy deposition even further.

The superior carrier mobility in HPGe,  $3.6 \times 10^4$  and  $4.2 \times 10^4 \frac{cm^2}{V-s}$  for electrons and holes, respectively, are significant reasons as to why HPGe is widely touted as the gold standard for gamma-ray spectroscopy [34]. The same attributes for CdZnTe are far lower; the electron and hole mobility measured for Cd<sub>0.8</sub>Zn<sub>0.2</sub>Te are 1350 and 120  $\frac{cm^2}{V-s}$ , respectively [37]. The hole mobility is low in absolute terms and relative to the electron mobility. For this reason, CdZnTe detectors are considered single polarity charge sensing devices.

Due in part to the low mobility values in CdZnTe, detectors are predominantly fabricated in two configurations whose performance is not sensitive to the poor mobility: thin, planar devices and/or pixelated detectors of varying thickness. The latter devices are position-sensitive. While this does not mitigate the trapping of hole carriers, it allows one to compensate for it with detailed system response functions. This process is described in more detail in Sections 2.4.1 and 2.4.2.

The detectors used in this work are  $20 \times 20 \times 15 \text{ mm}^3$ , featuring an  $11 \times 11$  array of pixelated anodes with a single planar cathode (Figure 2.1). The pitch between anodes

pixels is a relatively large 1.72 mm, which suits the detectors well for detecting and localizing gamma-ray interactions within a wide dynamic range between 20 keV to several MeV. While there are several vendors that can accommodate this design, those grown and fabricated by Redlen Technologies are used predominantly in this work [38].

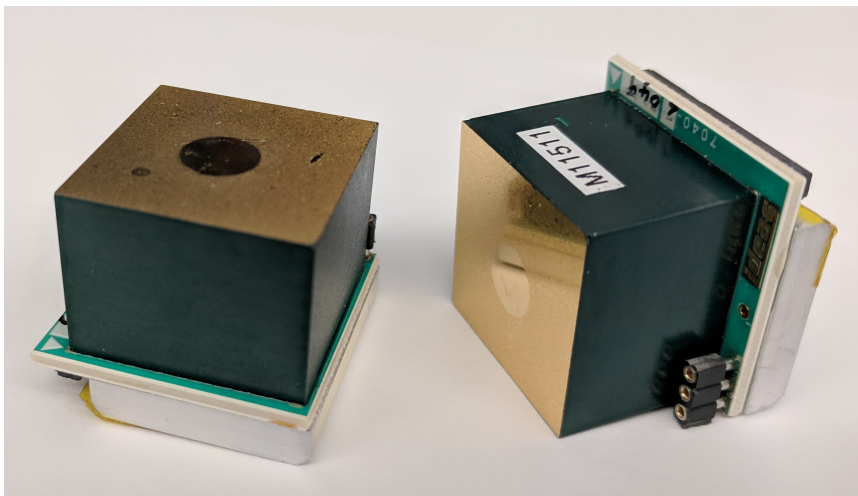


Figure 2.1: Two  $20 \times 20 \times 15 \text{ mm}^3$  Redlen detectors directly coupled to ASICs.

## 2.2 The Shockley-Ramo Theorem

The means by which detector electrodes sense signal carriers are modeled by the Shockley-Ramo theorem. This theorem describes how deposited energy translates to a measurable signal. The eponymous theorem was originally developed separately by Shockley [39] and Ramo [40] in 1938 and 1939, respectively, to model the induced current on conductors produced by electrons moving in vacuum. The implication of this theorem for semiconductor detectors was later published by He in 2001 [29]. Theorem II.1 reproduces the results most pertinent to the work in this thesis.

**Theorem II.1** (Shockley-Ramo Theorem). *The charge induced,  $Q$ , on an electrode by a signal carrier with charge  $q$  corresponds to the following relationship*

$$Q = -q\Delta\phi_0(\mathbf{x}) \quad (2.2)$$

The weighting potential,  $\phi_0(\mathbf{x})$ , is only a function of the geometry of the electrodes within a device. For devices in which there are several electrodes, the charge induced on one electrode is independent of all other electrodes.

The proof of the Theorem II.1 depends on the following lemma.

**Lemma II.2.** *During a time span between  $t_0$  and  $t_f$ , the change in energy stored within the electric field is independent of the electric field imposed by the capacitance of the electrodes,  $\mathbf{E}_0$ . It is only a function of the electric fields created by the space charge,  $\mathbf{E}_\rho$ , and the moving charge,  $\mathbf{E}_q$ . Let  $\mathbf{E}_1 = \mathbf{E}_\rho + \mathbf{E}_q$ .*

$$\begin{aligned} \frac{1}{2}\varepsilon \int_{\mathcal{D}} [\mathbf{E}_0(t_f) + \mathbf{E}_1(t_f)]^2 - [\mathbf{E}_0(t_0) + \mathbf{E}_1(t_0)]^2 dV \\ = \frac{1}{2}\varepsilon \int_{\mathcal{D}} \mathbf{E}_1(t_f) \cdot \mathbf{E}_1(t_f) - \mathbf{E}_1(t_0) \cdot \mathbf{E}_1(t_0) dV \quad (2.3) \end{aligned}$$

Consider a semiconductor device  $\mathcal{D}$  with  $N$  electrodes held at potential  $V_i$  for  $i \in \{1, 2, \dots, N\}$  and relative permittivity  $\varepsilon$ . At a time  $t_0$ , a charge carrier is generated, and it begins to drift under the influence of electrical bias. In this system, there are three components of the electric field: the electric field generated by the capacitance of electrodes ( $\mathbf{E}_0$ ), residual space charge within device  $\mathcal{D}$  ( $\mathbf{E}_\rho$ ) and the field imposed by the moving charge ( $\mathbf{E}_q$ ). As a matter of convenience,  $\mathbf{E}_1$  is the summation of the latter two electric fields,  $\mathbf{E}_\rho$  and  $\mathbf{E}_q$ . It is equivalent to the electric field in  $\mathcal{D}$  when all electrodes are held at ground by the power supplies.

Each component of the electric field is superimposed to form the cumulative elec-

tric field,  $\mathbf{E}$ . While charge moves in the time segment  $[t_0, t_f]$ , the energy stored in the electric field changes according to Equation 2.5.

$$\Delta U_{\mathbf{E}} = \frac{1}{2}\varepsilon \int_{\mathcal{D}} \mathbf{E}(t_f)^2 - \mathbf{E}(t_0)^2 dV \quad (2.4)$$

$$= \frac{1}{2}\varepsilon \int_{\mathcal{D}} (\mathbf{E}_0(t_f) + \mathbf{E}_1(t_f))^2 - (\mathbf{E}_0(t_0) + \mathbf{E}_1(t_0))^2 dV \quad (2.5)$$

The electric field  $\mathbf{E}_0$  is sensitive only to the geometry of the electrodes and the potentials at which they are held; it is independent of the moving charge and space charge. As a result,  $\mathbf{E}_0$  does not change in the time frame  $[t_0, t_f]$ .

$$\begin{aligned} & \frac{1}{2}\varepsilon \int_{\mathcal{D}} (\mathbf{E}_0 + \mathbf{E}_1(t_f))^2 - (\mathbf{E}_0 + \mathbf{E}_1(t_0))^2 dV \\ &= \frac{1}{2}\varepsilon \int_{\mathcal{D}} 2\mathbf{E}_0 \cdot \mathbf{E}_1(t_f) + \mathbf{E}_1(t_f) \cdot \mathbf{E}_1(t_f) - 2\mathbf{E}_0 \cdot \mathbf{E}_1(t_0) - \mathbf{E}_1(t_0) \cdot \mathbf{E}_1(t_0) dV \end{aligned} \quad (2.6)$$

This equation can be simplified further by evoking the relationship between potential and the electric field in Equations 2.7 and 2.8 and Green's first identity, which relates the flux through the surface of an electrode,  $S_i$ , to the volume integral of the divergence in Equation 2.9 [41].

$$\mathbf{E}_0 = -\nabla\phi_0 \quad (2.7)$$

$$\mathbf{E}_1 = -\nabla\phi_1 \quad (2.8)$$

$$\int_{\mathcal{D}} \phi_1 \nabla^2 \phi_0 + \nabla\phi_1 \nabla\phi_0 dV = \oint_{\partial\mathcal{D}} \phi_1 \nabla\phi_0 \cdot d\mathbf{S}_i \quad (2.9)$$

From the boundary conditions of device  $\mathcal{D}$ , the Laplacian of the potential field

generated by electrode capacitance must be 0. Furthermore, the electrodes are effectively grounded when only  $\mathbf{E}_1$  is present; the potential  $\phi_1$  evaluated on the surface of the electrodes for such a configuration is 0. These conditions yield the simplification of Equation 2.9 and confirm Lemma II.2.

$$\int_{\mathcal{D}} \mathbf{E}_0 \cdot \mathbf{E}_1 dV = \int_{\mathcal{D}} \nabla \phi_1 \nabla \phi_0 dV = 0 \quad (2.10)$$

$$\begin{aligned} \frac{1}{2} \varepsilon \int_{\mathcal{D}} [\mathbf{E}_0(t_f) + \mathbf{E}_1(t_f)]^2 - [\mathbf{E}_0(t_0) + \mathbf{E}_1(t_0)]^2 dV \\ = \frac{1}{2} \varepsilon \int_{\mathcal{D}} \mathbf{E}_1(t_f) \cdot \mathbf{E}_1(t_f) - \mathbf{E}_1(t_0) \cdot \mathbf{E}_1(t_0) dV \end{aligned} \quad (2.11)$$

**Lemma II.3.** *Let  $V_i$  represent the potential on the  $i^{\text{th}}$  electrode that occupies space on the surface of device  $\mathcal{D}$ . During  $[t_0, t_f]$ , the work exerted by the power supplies and the work performed by the electric field  $\mathbf{E}_0 + \mathbf{E}_1$  on the moving charge  $q$  is equal to the change in energy stored within the electric field of device  $\mathcal{D}$ .*

$$\sum_i^N V_i \Delta Q_i - \int_{t_0}^{t_f} q (\mathbf{E}_0 + \mathbf{E}_1) \cdot \mathbf{v} dt = \frac{1}{2} \varepsilon \int_{\mathcal{D}} \mathbf{E}_1(t_f) \cdot \mathbf{E}_1(t_f) - \mathbf{E}_1(t_0) \cdot \mathbf{E}_1(t_0) dV \quad (2.12)$$

In this system, two additional forms of electrical work are performed: work performed by electrical power supply and the work performed on the moving charge. During device operation, all electrodes are held at constant potential by the power supply. For electrode  $i$ , electrical potential of the form  $U_{S_i} = Q_i V_i$  is present. As the charge carrier induces charge on the electrode, the potential energy of electrode  $i$

must change accordingly. The power supply performs work on the electrode to keep it at constant potential.

$$\Delta U_{S_i} = \Delta V_i Q_i + V_i \Delta Q_i = V_i \Delta Q_i \quad (2.13)$$

Work is also performed to move the charge carrier from a higher potential energy to a lower potential energy. The movement of the charge with scalar charge  $q$  is influenced by both the static electric field  $\mathbf{E}_0$  and the time-dependent components of the electric field ( $\mathbf{E}_1$ ). Equation 2.14 provides the corresponding model for electrical work for charge moving with velocity  $\mathbf{v}$ .

$$\Delta U_q = \int_{t_0}^{t_f} q (\mathbf{E}_0 + \mathbf{E}_1) \cdot \mathbf{v} dt \quad (2.14)$$

According to the conservation of energy, the summation of Equations 2.11, 2.13 and 2.14 yield Lemma II.3.

**Lemma II.4.** *Under conditions in which the electrodes of  $\mathcal{D}$  are held at ground, there is no transfer of energy from the power supply to the moving charge carrier. By the conservation of energy, the change in energy stored in electric field  $\mathbf{E}_1$  must result from interactions with the moving charge.*

$$\int_{t_0}^{t_f} q \mathbf{E}_1 \cdot \mathbf{v} dt = \frac{1}{2} \varepsilon \int_{\mathcal{D}} \mathbf{E}_1(t_f) \cdot \mathbf{E}_1(t_f) - \mathbf{E}_1(t_0) \cdot \mathbf{E}_1(t_0) dV \quad (2.15)$$

Combining the results of Lemmas II.3 and II.4, Equation 2.17 is obtained. Note that the conventional notation for Theorem II.1 does not include the potential on

electrode  $i$ ,  $V_i$ . Instead, weighting potential,  $\phi(\mathbf{x})$ , is normalized by the potential of the electrode, and it ranges between 0 and 1. Such notation yields the Shockley-Ramo theorem given by Equation 2.2.

$$\sum_i^N V_i \Delta Q_i = \int_{t_0}^{t_f} q \mathbf{E}_0 \cdot \mathbf{v} dt = \int_{\mathbf{x}(t_0)}^{\mathbf{x}(t_f)} q \mathbf{E}_0 \cdot d\mathbf{x} \quad (2.16)$$

$$= -q [\phi_0(\mathbf{x}(t_f)) - \phi_0(\mathbf{x}(t_0))] \quad (2.17)$$

For the Redlen CdZnTe detectors described in Section 2.1, bias is applied to the planar cathode surface while the anode pixels remain at a potential near ground. Applied bias on the cathode is set near 1 kV for every 5 mm of detector thickness to optimize charge drift properties and leakage current. This forms a constant electric field as a function of depth under ideal circumstances. This is represented by Equation 2.18 in which the  $C$  is a constant.

$$-\frac{d\phi}{dz} = E(z) = C \quad (2.18)$$

Due to the planar geometry, the weighting potential for the cathode may be obtained from Equation 2.19 by integrating with respect to the depth,  $z$ , and applying boundary conditions 2.20 and 2.21. The solution to Equation 2.19 is featured graphically in Figure 2.2. Recall that the mobility of holes in CdZnTe are insignificant compared to the mobility of electrons. This entails that for fixed energy deposition, the induced cathode signal provides a depth-dependent response.

$$\phi_{\text{Cathode}}(z) = -Cz + D \quad (2.19)$$

$$\phi_{\text{Cathode}}(z = \text{Cathode}) = 1 \quad (2.20)$$

$$\phi_{\text{Cathode}}(z = \text{Anode}) = 0 \quad (2.21)$$

Consider the two hypothetical gamma-ray interactions occurring at depths  $z_1$  and  $z_2$  in Figure 2.2. The electrons produced by these interactions drift from the initial depth of interaction towards the anode, at which point the cathode weighting potential has a value of 0. The starting cathode weighting potential is determined entirely by the depth of interaction. As shown in Figure 2.2, the resulting change in weighting potential is linearly proportional to the depth of interaction.

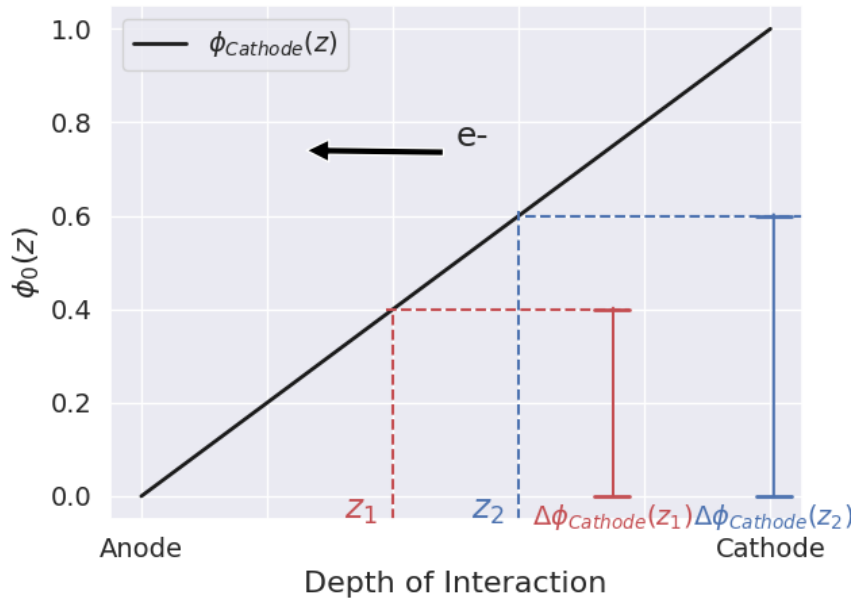


Figure 2.2: Cathode weighting potential as a function of the depth of interaction and the corresponding change in weighting potential for two hypothetical interactions.

Unlike the cathode, the individual anodes occupy only a small fraction of the opposing surface of the pixelated CdZnTe detector. If the anodes were replaced by

a single plane, the solution for its weighting potential would be equal to the linear general solution in Equation 2.19, albeit with boundary conditions 2.22 and 2.23.

$$\phi_{Anode}(z = \text{Cathode}) = 0 \quad (2.22)$$

$$\phi_{Anode}(z = \text{Anode}) = 1 \quad (2.23)$$

Denote the weighting potential solution for a planar anode by  $\phi_{Planar}(z)$  and the solution for its constituent pixels by  $\phi_i(z)$  for  $i \in 1, 2, \dots, N$ . The pixels bound to the anode surface are collectively equivalent to a planar electrode and operate under conditions 2.24, 2.25 and 2.26.

$$\phi_{Planar}(z) = \sum_i^N \phi_i(z) \quad (2.24)$$

$$\phi_{Planar}(z) \geq \phi_i(z) \quad (2.25)$$

$$\phi_i(z = \text{Anode}) = \begin{cases} 1, & \text{if pixel } i \text{ is collecting} \\ 0, & \text{otherwise} \end{cases} \quad (2.26)$$

These conditions do not imply that the weighting potential  $\phi_i(z)$  must also be linear in depth; only the collective anode is bound to the solution in Equation 2.19. Due to the exceedingly more intricate geometry for pixelated detectors, the solution for the weighting potential is more difficult to derive. Eskin, Barrett, & Barber proposed analytical solutions for the induced signal on segmented electrodes of position-sensitive semiconductor detectors [42], and numerical methods provide alternative means of modeling the weighting potential. For the purposes of this work, the 3-D weighting potential was approximated via commercially-available Ansys Maxwell software.

Figure 2.3 displays the numerical solution for a collecting pixel weighting potential. Near the cathode surface ( $z = 0$  mm according to Figure 2.3), all anode pixels are at an initial weighting potential of 0. As the charge carrier begins its drift towards the anode, the charge is effectively equidistant from all anode pixels. Thus the weighting potential is nearly equally divided among all anode pixels. As the charge nears the collecting pixel, the weighting potential becomes concentrated on the collecting pixel due its proximity to the charge. This accounts for the rapid rise in weighting potential for the collecting pixel in Figure 2.3.

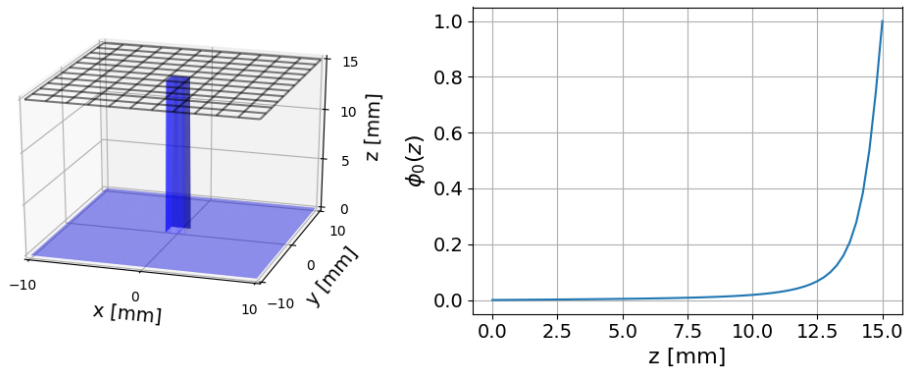


Figure 2.3: Collecting pixel weighting potential as a function of depth (right) for the highlighted region in the virtual detector volume (left).

Figure 2.4 provides a 2-D distribution of the weighting potential for a slice of the detector volume that stretches from the cathode surface to the anode surface. Charge carriers follow a path starting at the red dot and ending at the green dot. Consistent with Figure 2.3, the central pixel collects the drifting charge, which is reflected by the rapid rise in weighting potential near the point of charge collection. The remaining, non-collecting pixels remain near 0 weighting potential throughout the charge carrier drift.

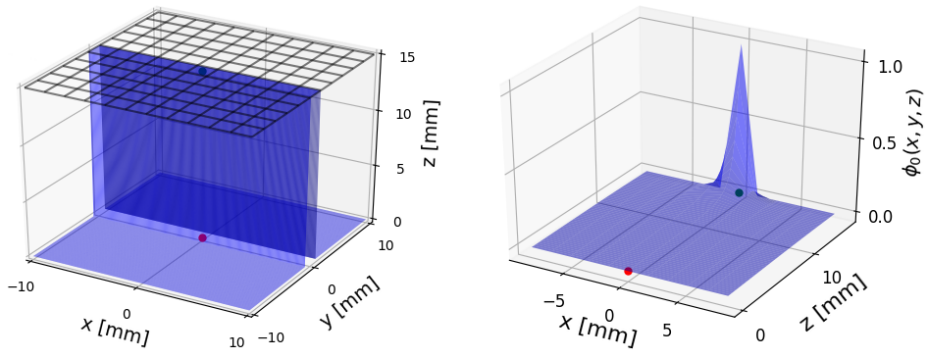


Figure 2.4: Weighting potential as a function of position for a slice in the middle of the pixelated detector when charge carriers drift from the red to green dots (right) and the corresponding detector slice in the detector (left). The weighting potential profile in the  $x - z$  plane corresponds to the solid, blue portion of the detector in the left pane.

## 2.3 Data Acquisition

Once gamma rays are generated in the detection medium, the resulting signals must be sensed, measured and recorded. The components that perform these tasks constitute the front-end and readout electronics. The former are responsible for recording the induced charge on the collecting anode(s), and the latter digitize and package event data for subsequent analysis.

This section does not focus on the development of the hardware, firmware and software that make data acquisition possible; these designs were thoroughly established and discussed in the theses by Zhu [43], Yang [44] and Streicher [45]. Rather, the intent is to introduce the core subsystems of the data acquisition system to understand the sources of measurement noise.

As charge is induced on any given electrode, the resulting current is integrated and amplified via front-end electronics. As displayed in Figure 2.5 in its distilled form, the front-end electronics associated with the CdZnTe detector system used for this work consist of a charge-sensitive amplifier and its feedback circuit. Some of the induced charge is distributed over the sensor capacitance,  $C_D$ , and the rest is distributed over

the implicit input capacitance to the operational amplifier. With the capacitor in the feedback circuit,  $C_f$ , and sufficiently high amplifier gain, the voltage gain per unit input charge is effectively  $\frac{1}{C_f}$ . For applications in which the signal must decay rapidly, a resistive component may be placed in parallel with the feedback capacitor.

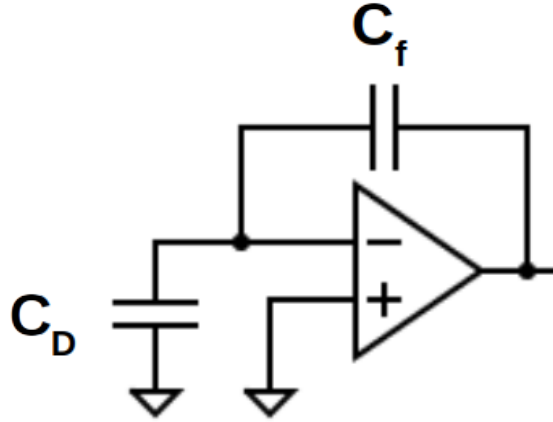


Figure 2.5: Diagram of a basic charge-sensitive amplifier used for amplifying the induced charge on an electrode.

In realistic systems, the integration time response is not instantaneous, and the voltage output is convolved with the responses of the sensor and amplifier. These components for each pixel are embedded in the application-specific integrated circuit (ASIC) dedicated to a detector. The noise of the amplifier output has several sources. There is inherent statistical noise in the voltage source that originates from the variable amount of charge carriers generated by the seminal gamma-ray interaction. One must also consider the shot and thermal noise inherent to the sensor and front-end circuitry. Unless the front-end and sensor system preserve phase, these sources combine in quadrature as they are statistically independent.

The voltage output of the amplifier circuits is sampled and stored in the ASIC capacitor bank where each waveform awaits digitization by a 14-bit analog-to-digital converter (ADC). The ADC resolution is chosen in such a way that the digitization

noise is less than that of the analog input. According to Spieler, the digitization noise for an  $n$ -bit ADC with dynamic range  $V$  is modeled by Equation 2.27 [32].

$$\sigma_v^2 = \frac{2^{-2n}V^2}{12} \quad (2.27)$$

Depending on the detector system configuration, the ADC digitizes the signals (colloquially referred to as ‘waveforms’) from between 1 and 3 ASIC modules in serial. Due to this communication bottleneck, the dead time between acquired events correlates strongly with the number of waveforms digitized as demonstrated in Figure 2.6.

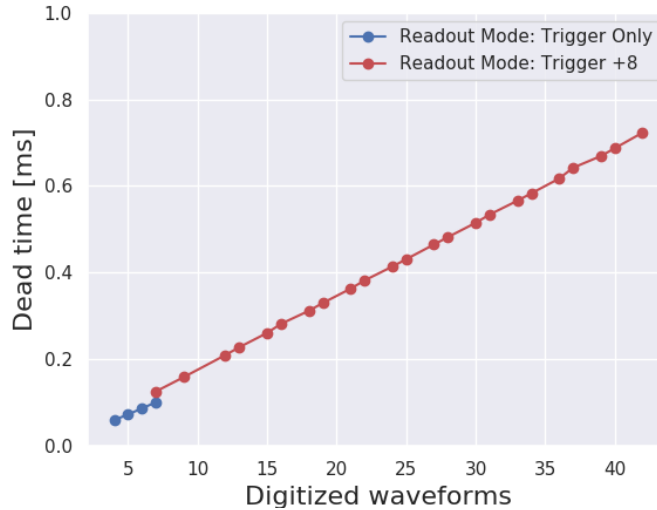


Figure 2.6: Measured data acquisition dead time as function of the number of digitized waveforms per event for two modes of operation.

To mitigate this bottleneck, only samples that are deemed pertinent to the analysis of the event are digitized in sparse mode operation. Under this mode of operation, only the triggering pixel(s) and pixels adjacent to a triggering pixel are digitized. This limits system dead time otherwise consumed by pixels with no appreciable signal. Sparse mode includes the two variants featured in Figure 2.6, and a “trigger +4” option is also available.

For the purposes of the methods presented in Chapter IV, trigger +4 is the default setting. The digitized output for a generic single-pixel event are demonstrated in Figure 2.7. This includes the waveform for the collecting anode pixel, the cathode signal and the signals from the four adjacent neighbor pixels. The sample in Figure 2.7 is representative of the expected system behavior; the cathode signal is far more receptive to interference due to its greater surface area. For this reason, system readout is triggered by anode pixel signals to minimize false triggers.

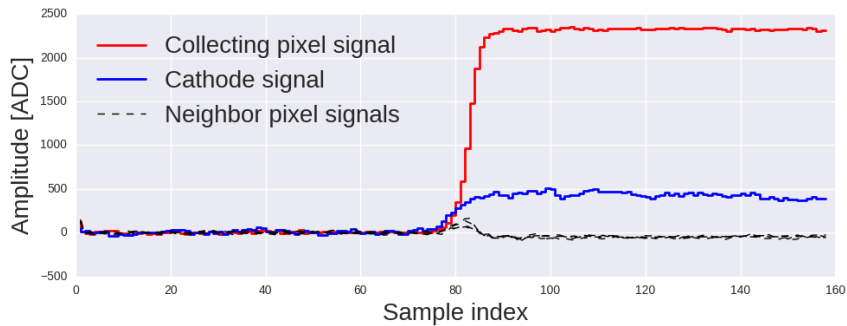


Figure 2.7: Digitized signals for a generic single-pixel event under trigger +4 mode.

## 2.4 Event Reconstruction

Event reconstruction entails the methods and algorithms designed to estimate the latent event variables - gamma-ray energy deposition and position of interaction - from observed signals. The foundational work for these methods was developed by Zhang [46] and Kaye [47]. While progress has been made in the development of event reconstruction methods since these publications, they derive heavily from the contributions from these researchers. This section provides a concise account of the conventional methods that precede the development of event reconstruction methods detailed in subsequent chapters.

While the position of a gamma-ray interaction is implicitly treated as a point estimate, it more closely approximates the center of mass of all charge carriers generated

by a single interaction. For the purposes of this work, the reconstructed position is treated as the location at which the gamma-ray interact, although this assumption is not entirely accurate. At increasingly higher gamma-ray energy, the scattered gamma ray transfers considerable energy to the recoil electron of a Compton scattering interaction [48]. Such an interaction may have displacement between the position of interaction and the point at which charge carriers are generated on the order of millimeters.

### 2.4.1 Depth of Interaction and Energy Reconstruction

As discussed in Section 2.2, the amplitude of induced signals on the cathode and - to a lesser extent - the pixelated anodes vary as a function of the depth of interaction. For this reason, depth and energy reconstruction are tightly coupled. The cathode signal amplitude is a function of both energy deposition and the depth of interaction. If only the cathode signal amplitude is observed, one obtains an underdetermined system of equations. The cathode signal alone does not provide sufficient information to estimate the depth of interaction. Due to the pixelated detector geometry and the resulting anode weighting potential (Figure 2.3), the anode signal amplitude is relatively insensitive to changes in the depth of interaction. It may be used as a normalization constant for the cathode signal amplitude to uniquely determine the depth of interaction.

This method for depth sensing in single-polarity semiconductor devices was first demonstrated by He et al. [49], and it became known as the cathode-to-anode amplitude ratio (CAR) technique. This is explicitly modeled in Equation 2.28; a cathode-side interaction tends closer to a CAR value of 1, while the CAR of an anode-side interaction evaluates closer to 0.

$$\text{CAR} = \frac{V_{\text{Cathode}}}{V_{\text{Anode}}} \quad (2.28)$$

In practice, the anode amplitude is not entirely independent of the depth of interaction, but the CAR profile it produces is monotonically increasing in depth from the anode as demonstrated in Figure 2.8. The observed CAR adheres to the expected linear relationship at high depths from the anode, but it deviates from this linear behavior insignificantly near the anode surface.

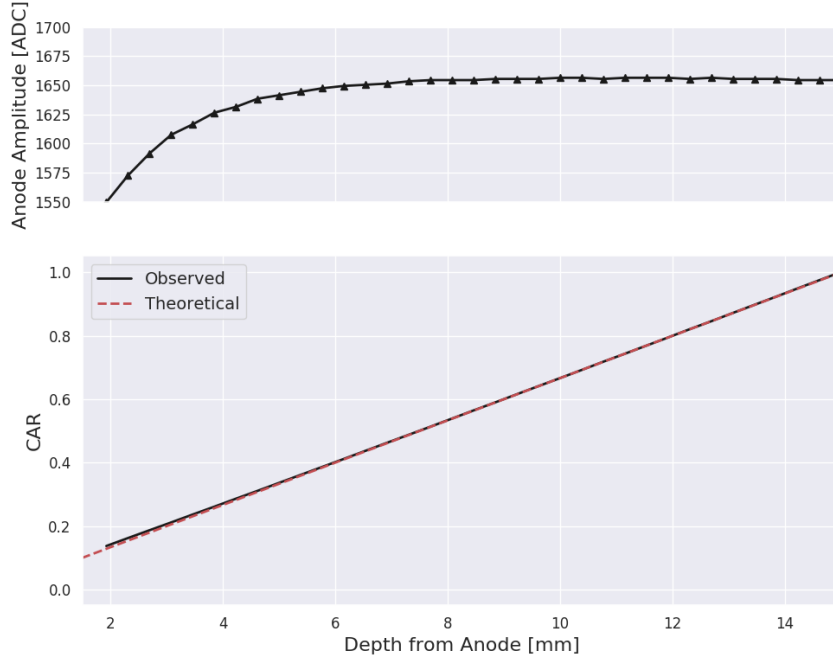


Figure 2.8:  $^{137}\text{Cs}$  photopeak amplitude for an anode pixel as function of depth from the anode (top) and the corresponding CAR as a function of depth.

Despite the constant, known incident gamma-ray energy, the amplitude for a generic anode pixel in Figure 2.8 varies as a function of depth. To compensate for changes in depth, energy is estimated by multiplying the observed anode amplitude,  $V_n$ , for pixel  $n$  by a depth-specific correction factor (Equation 2.29). This correction factor is determined empirically for each channel and discrete depth bin.

$$E = f(n, z) V_n \tag{2.29}$$

The empirical model for the correction factor is advantageous compared to ana-

lytical models that are vulnerable to systematic error (bad regression fit) and model complexity due to numerous free parameters (better fit, but susceptible to overfitting). The only free parameter for the adopted, discrete model is the number of virtual depth bins. The default value is based on a very conservative estimate of the depth reconstruction uncertainty. To estimate depth in continuous space, depth is generally determined by linear interpolation.

As demonstrated in Figure 2.9, depth correction provides demonstrable improvement in energy resolution compared to the raw amplitude spectrum. The energy resolution improves from 0.81% to 0.34% FWHM, and the peak-to-Compton continuum amplitude ratio increases threefold. However, depth corrections do not completely mitigate the low-energy tail apparent in the photopeak of both spectra, which is attributed to the loss of charge carriers to the gap between anode pixels [50]. Depth corrections alone do not adequately address this mechanism; the centroids of the empirical data that comprise the depth-specific corrections are relatively insensitive to the effect of the outliers in the low-energy tail.

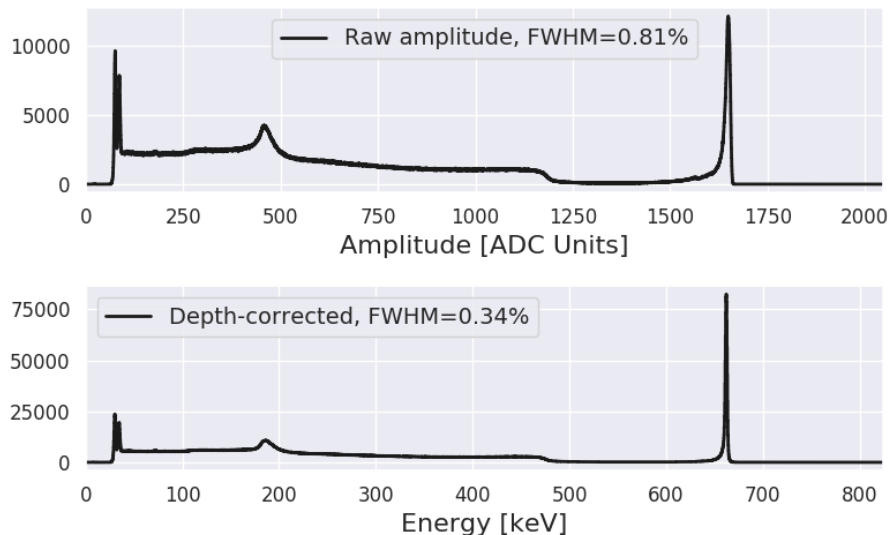


Figure 2.9: Energy spectrum obtained before (top) and after (bottom) applying depth corrections to data collected from a  $^{137}\text{Cs}$  exposure.

The CAR provides a robust method for estimating the depth of interaction, but its

application is limited to single-pixel interactions. When there are multiple, distinct interactions observed in the same event, the cathode amplitude is the superposition of the signals induced by multiple clusters of charge carriers. Such events rely on a proxy for the electron drift time, which can be inferred from the difference in triggering times between the cathode and triggering anode signals as demonstrated in Figure 2.10. In practice, waveforms are first filtered using a CR-RC<sup>n</sup> filter before determining the trigger time, but the same principle remains.

The anode-side interaction in the top partition reflects the relatively short time elapsed between anode and cathode triggers, which are approximated by the vertical, dotted lines. The digitized signals for a cathode-side interaction are juxtaposed in the bottom partition, and the time between signal triggers is demonstrably longer. In practice, the depth of interaction is a solution to the inverse problem  $z = f^{-1}$  (drift time), and it provides approximately equal precision in depth estimation as CAR for 662 keV single-pixel events according to Kaye [47].

#### 2.4.2 Lateral Position Reconstruction

The known location of the triggering pixel provides an estimate of the lateral position of interaction. The coarse precision is limited by the 1.72 mm pitch between adjacent anode pixels, but Zhu introduced a method to achieve more precise estimates of the lateral position using the induced signals on neighboring pixels [43]. Although the final weighting potential for an adjacent, non-collecting neighbor pixel should be 0, the induced transient signal has appreciable amplitude at its peak.

The principle behind subpixel position sensitivity depends on the relative neighbor signal amplitude for opposing neighbors. Consider the sample waveforms featured in Figure 2.11. The center, triggering pixel contains two waveforms: one in which the interaction occurs near the left pixel boundary and one in which the interaction occurs near the right pixel boundary. While the triggering pixel waveforms are nearly iden-

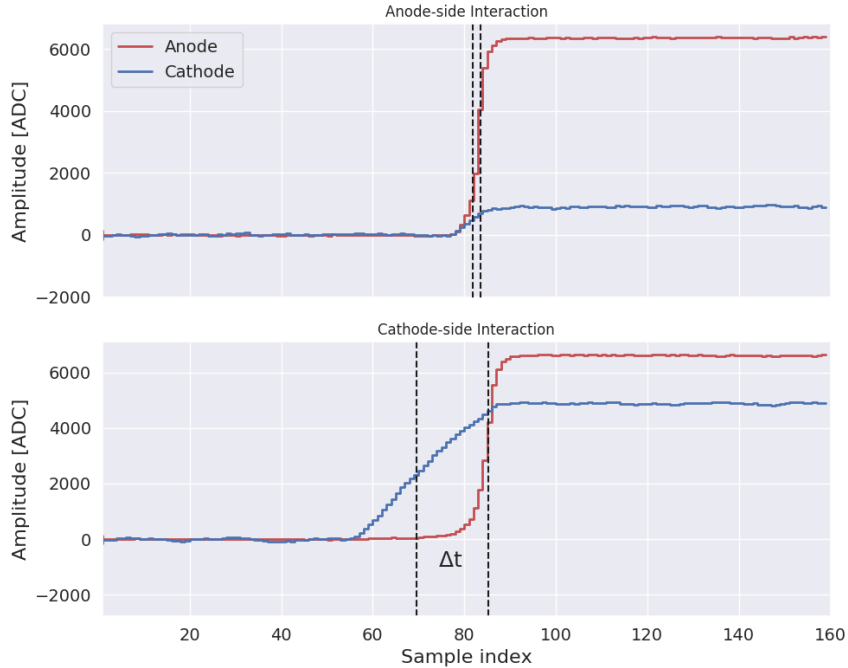


Figure 2.10: Generic waveforms for a single-pixel, 662 keV event and the associated drift times for an anode-side interaction (top) and a cathode-side interaction (bottom).

tical, the sampled signals from adjacent pixels distinguish the interactions far more effectively. The adjacent pixel signals record a high amplitude when the triggering pixel interaction nears the boundary shared between the two pixels.

This feature can be exploited to estimate the lateral position to greater precision than the coarse estimate provided by the triggering pixel location. Equations 2.30 and 2.31 provide the primary metrics used for estimating subpixel  $x$  and  $y$  values, respectively. The value  $S_i$  indicates the maximum signal amplitude for pixel  $i$ , and the function  $f$  relates the observed ratios  $R_x$  and  $R_y$  to the physical  $x$  and  $y$  locations, respectively.

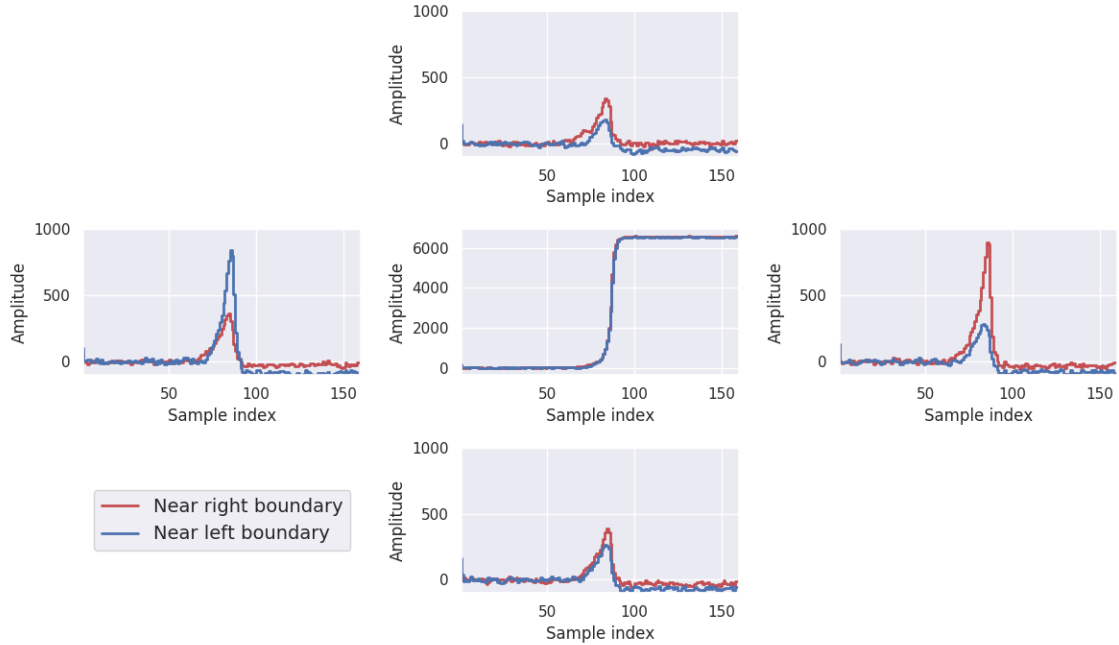


Figure 2.11: Array of pixels (triggering pixel in the center surrounded by cardinal neighbors) and the signals induced for interactions in which the position is near the left and right pixel boundaries.

$$x = f(R_x) = f\left(\frac{S_{\text{Right}} - S_{\text{Left}}}{S_{\text{Right}} + S_{\text{Left}}}\right) \quad (2.30)$$

$$y = f(R_y) = f\left(\frac{S_{\text{Top}} - S_{\text{Bottom}}}{S_{\text{Top}} + S_{\text{Bottom}}}\right) \quad (2.31)$$

With this approach, Zhu & Anderson measured a position uncertainty of 230  $\mu\text{m}$  at 662 keV with detectors similar to those used in this work [51]. Due to this method's dependence on the signal amplitude from neighboring pixels, the uncertainty has positive correlation to noise in the amplitude estimate. This most severely affects interactions with a low energy deposition where the fixed electronic noise of the system is a more significant portion of the total induced amplitude.

### 2.4.3 Reconstruction of Multiple-Pixel Events

As the name suggests, multiple-pixel events consist of events in which more than one pixel triggers. This may be the result of a single interaction whose charge carriers occupy space over multiple adjacent pixels, or it may refer to events in which multiple interactions belonging to the same parent gamma-ray deposit energy in two or more pixels. While these two causes of multiple-pixel events are very different, the reconstruction methods share many features in common.

Unlike single-pixel events, the signal induced on an electrode is not solely attributed to a single cluster of charge carriers, but rather the induced signal consists of the time-varying contributions from multiple clusters of charge carriers. Depending on the distance between anode pixels, the resulting weighting potential crosstalk (WPCT) may alter the affected waveform and invalidate the underlying assumptions of the event reconstruction methods. As a prime example, CAR no longer applies to depth reconstruction because the cathode signal has an unknown contribution from all interactions.

The underlying cause for WPCT can be visualized through examination of the weighting potential of pixels adjacent to the collecting pixel. Consider a charge carrier that drifts from the cathode surface and is collected by the central anode pixel. Figure 2.12 displays the corresponding weighting potential for various anode pixels. Before collection on the center pixel, the charge induces a transient signal on all pixels in close proximity.

Consequently, the effects of WPCT are most pronounced for side-neighbor events as demonstrated in Figure 2.13. The top partition displays the anode and cathode signal waveforms for an event in which two triggering anode pixels are well-separated in the lateral dimension. Given this significant distance, WPCT is negligible, and there is no apparent distortion of the collecting anode waveforms. Now consider the side-neighbor, two-pixel event in the lower pane. The influence of WPCT from the

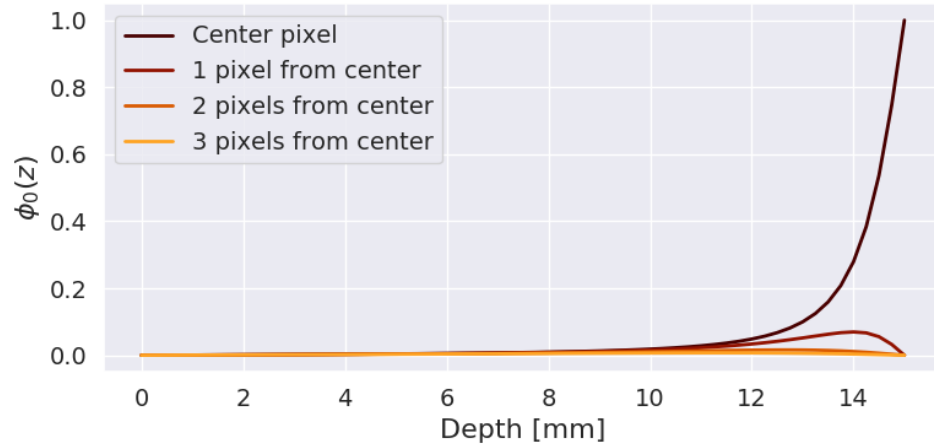


Figure 2.12: Weighting potential profile for an event in which a charge carrier is collected by the center pixel.

pixel with the large signal amplitude distorts the transient signal rise of the second anode waveform demonstrably.

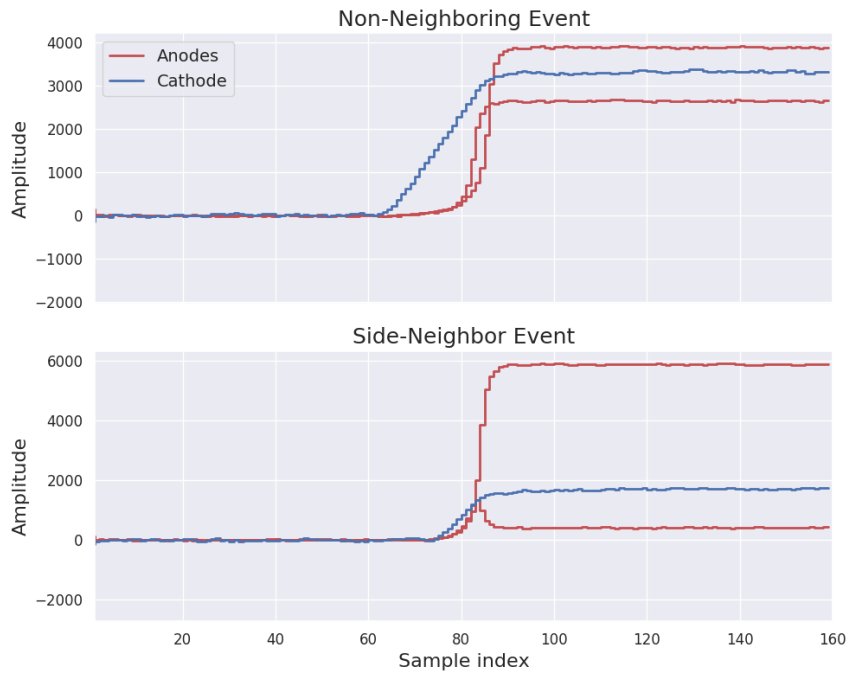


Figure 2.13: Anode and cathode signal waveforms for a two-pixel event with non-neighboring triggered pixels (top) and neighboring triggered pixels (bottom).

The presence of WPCT introduces systematic error into depth and energy recon-

struction methods that are otherwise reliable for single-pixel events. Anode waveforms altered by WPCT have a propensity to trigger earlier, and the reconstructed energy deposition tends to register lower than the actual energy deposition. Figure 2.14 demonstrates the systematic error in the reconstructed energy deposition for two-pixel events. As the separation between interactions decreases, the photopeak centroid decreases monotonically.

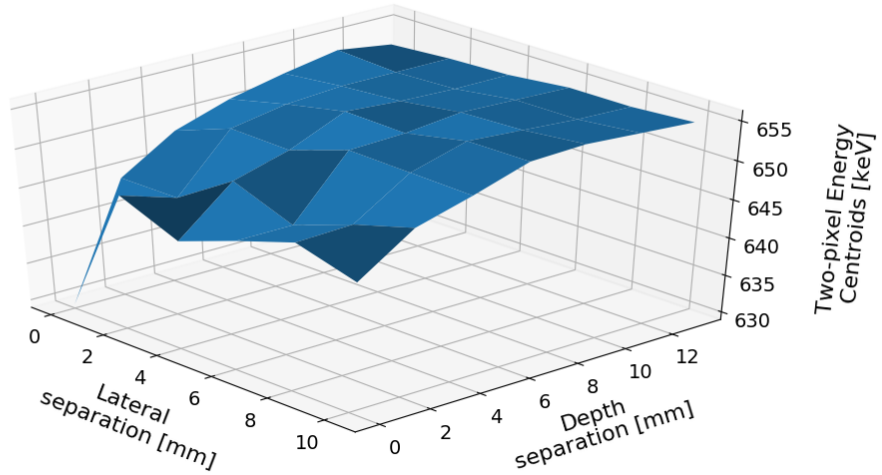


Figure 2.14: Photopeak centroid of two-pixel events at various degrees of separation between triggering pixels for a  $^{137}\text{Cs}$  exposure.

The WPCT correction introduced by Zhang [46] mitigates the systematic error in the reconstructed energy. Much like the depth-correction model, the WPCT energy correction models the change in energy using a discrete model (Equation 2.32). The correction  $f\left(\Delta z, \sqrt{\Delta x^2 + \Delta y^2}\right)$  is determined empirically from data in the calibration measurement, and it is multiplied by the induced signal amplitude on the two triggering pixels,  $V_1$  and  $V_2$ . Such measures improve multiple-pixel energy resolution by orders of 0.1%.

$$E = f\left(\Delta z, \sqrt{\Delta x^2 + \Delta y^2}\right) (V_1 + V_2) \quad (2.32)$$

While the correction described in Equation 2.32 targets the systematic error attributed to spatial separation, WPCT also varies with the difference in signal amplitudes. The difference in amplitude is conventionally measured by the energy ratio, defined as the normalized difference in energy (Equation 2.33). This metric ranges between 0 (nearly equal signal amplitudes) and 1 (nearly all of the total signal amplitude attributed to one pixel).

$$R_E = \frac{|E_1 - E_2|}{E_1 + E_2} \quad (2.33)$$

To understand this effect, consider the trend between combined energy and energy ratio for side-neighbor, two-pixel events in Figure 2.15. The events in question are those with similar depth separation and lateral separation to isolate the effects of energy ratio. Based on the Spearman correlation - a non-parametric measure of correlation - there is considerable positive correlation between two-pixel event energy and energy ratio.

Although the degree of WPCT varies significantly in three dimensions - depth separation, lateral separation and energy ratio - the WPCT correction is conventionally modeled as a function of only the depth and lateral separations due to the curse of dimensionality. The density of empirical, two-pixel event data used for finding WPCT corrections are highly concentrated in regions of low depth and lateral separation, whereas the data appear quite sparse for events separated by several depths and pixels. Therefore, the data in these large separation regions cannot be further divided without producing corrections with considerable statistical uncertainty.

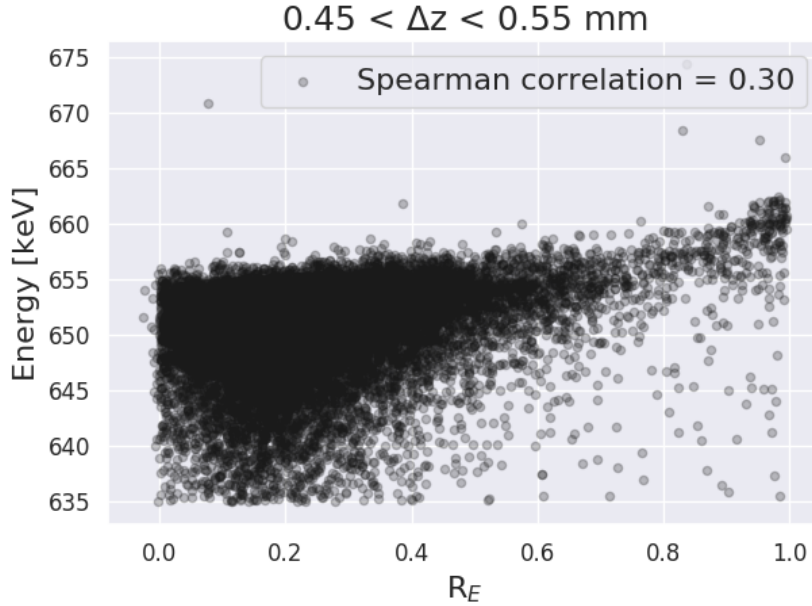


Figure 2.15: Two-pixel, side-neighbor event energy as a function of the energy ratio.

#### 2.4.4 Reconstruction by System Response Function

The methods presented up to this section are a product of legacy methods developed during a time in which analog front-end electronics were predominantly used. For each detection event, an analog ASIC provided only two values of interest per pixel: the amplitude of the induced signal and a proxy for the electron drift time [52]. The reconstruction methods developed in this time reflect the most efficient use of the meager data acquired from front-end electronics.

With the advent of digital front-end electronics, far more information can be extracted from each event. Rather than relying blindly on the shaper output of the analog front-end, one can preserve the entire digitized signal and use adaptive approaches to greater effect. Upon the introduction of the digital front-end electronics and the associated UM\_VAD readout system, early approaches focused heavily on the application of digital filtering.

Among the filters adapted to digitized waveforms of pixelated CdZnTe detectors, optimal energy resolution was obtained using trapezoidal filtering, which borrows

from the work of Jordanov & Knoll [53]. As demonstrated in Figure 2.16, the high frequency noise in raw waveforms is attenuated after the trapezoidal filter is applied to the raw waveforms. The amplitude of the respective signal is measured by the maximum amplitude of the filtered signal.

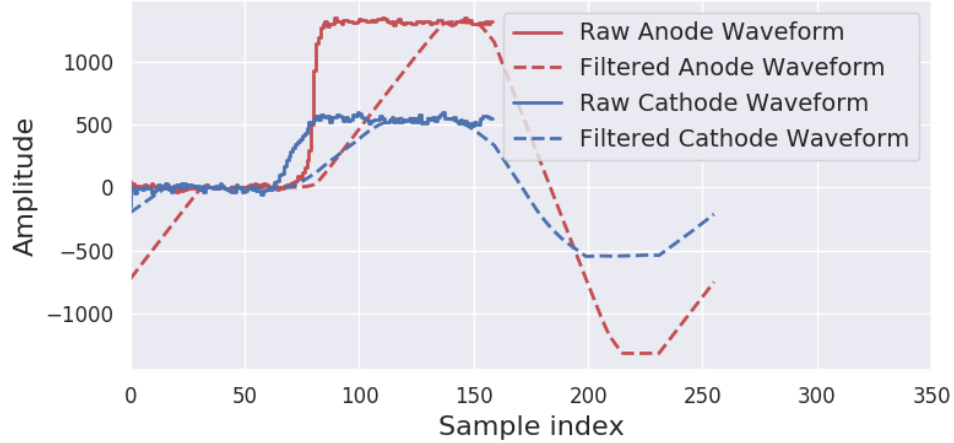


Figure 2.16: Raw and filtered waveforms for a generic single-pixel event.

The signal amplitudes and trigger times obtained by digitally filtered waveforms replaced the estimates previously acquired by analog front-end electronics. Despite the additional information provided by digitized waveforms, the procedures discussed in Sections 2.4.1, 2.4.2, and 2.4.3 were still practiced to perform event reconstruction.

Zhu proposed a method to make more judicious use of the full digitized waveforms by implementing a template-matching scheme designed to estimate the depth and energy deposition of gamma-ray interactions [43]. From the photopeak events extracted from  $^{137}\text{Cs}$  calibration measurements, system response functions (SRF) are formed for each channel and virtual depth bin as demonstrated in Figure 2.17. The SRF captures essential information - including the slope and signal amplitudes of the electrode waveforms - for determining depth of interaction and energy deposition.

The latent quantities - depth and energy deposition - of all subsequent single-pixel and multiple-pixel events are thereby estimated by determining which SRF the

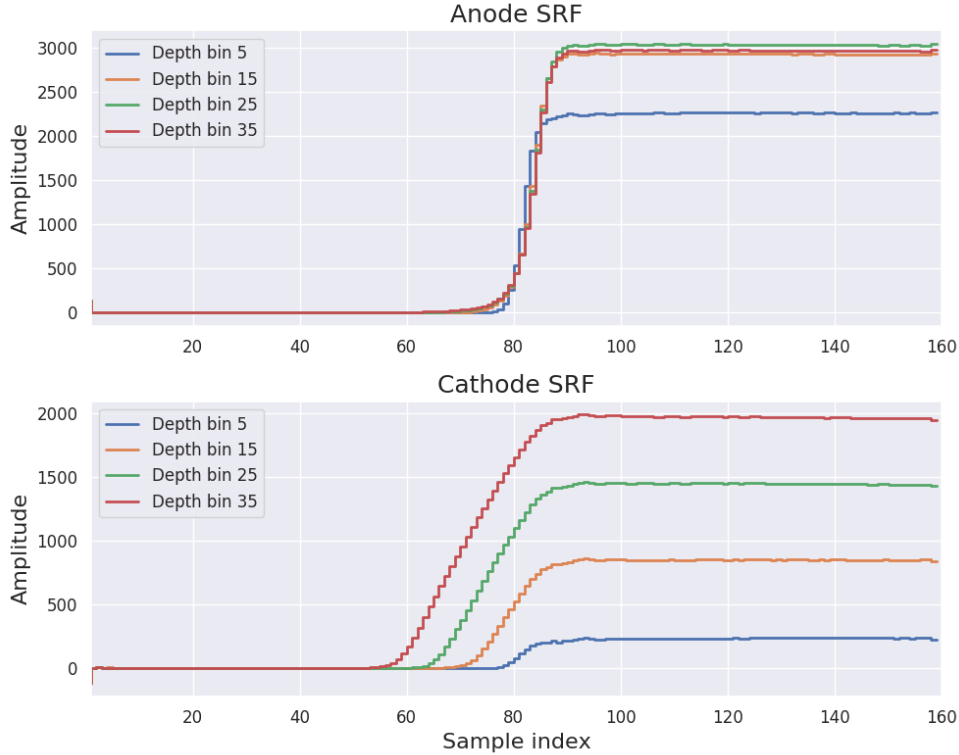


Figure 2.17: SRF for a generic anode channel (top) and the corresponding cathode SRF (bottom).

waveforms most resemble. This inverse problem is modeled symbolically by Equation 2.34 in which the variables  $\mathbf{x}$ ,  $\mathbf{y}$  and  $f$  represent the latent variables, the observations (waveforms) and the function that maps the two quantities, respectively. Given that the function is generally nonlinear, the Levenberg-Marquardt algorithm (LMA) provides an effective way to determine which latent quantities produced the observed waveforms [54, 55].

$$\mathbf{x} = f^{-1}(\mathbf{y}) \quad (2.34)$$

The LMA iteratively determines a solution that minimizes the objective function in Equation 2.35. The quantity  $\sum_i (y_i - f(\mathbf{x}, i))^2$  represents the sum of squares where  $y_i$  and  $f(\mathbf{x}, i)$  are the observed amplitude and the predicted amplitude at waveform index  $i$ .

$$\mathbf{x} = \arg \min_{\mathbf{x}} \sum_i (y_i - f(\mathbf{x}, i))^2 \quad (2.35)$$

For each iteration, the latent variables are incremented by a quantity  $\Delta\mathbf{x}$ . A Taylor expansion of the function evaluated at  $\mathbf{x} + \Delta\mathbf{x}$  approximates the update schema for each iteration (Equation 2.36). The function Jacobian,  $\mathbf{J}$ , measures the gradient at  $\mathbf{x}$  and provides direction to the optimal solution in the latent variable space. The optimal value of  $\Delta\mathbf{x}$  for the unregularized sum of squares is given by Equation 2.37.

$$f(\mathbf{x} + \Delta\mathbf{x}) \approx f(\mathbf{x}) + \mathbf{J}\Delta\mathbf{x} \quad (2.36)$$

$$\Delta\mathbf{x} = (\mathbf{J}^T\mathbf{J})^{-1}(\mathbf{y} - f(\mathbf{x})) \quad (2.37)$$

The numerical linear algebra procedure for finding this optimal value requires at least  $3n$  floating point operations for each iteration, where  $n$  represents the summed length of all waveforms. Based on empirical observations of this scheme, between ten and twenty iterations are required to find a local minimum for each event. For this reason, reconstruction by SRF is relatively computationally intensive, and this reconstruction may struggle to provide real-time processing in high count rate environments. This problem is compounded further when 3 and 4-pixel events are reconstructed, as  $n$  increases linearly with the number of waveforms included in the inverse problem.

The single-pixel event depth estimated by SRF yields similar results compared to the more conventional CAR, albeit with varying consistency as a function of energy deposition as demonstrated in Figure 2.18. The variance in the differential depth, which is defined as the CAR estimate less the SRF estimate, appears quite small when gamma-ray interactions deposit a large amount of energy, but the variance monotonically increases as the energy deposition decreases. The distributions of low

energy ranges skews towards positive values and indicates that the CAR estimates produce depths that are systematically higher than that of SRF.

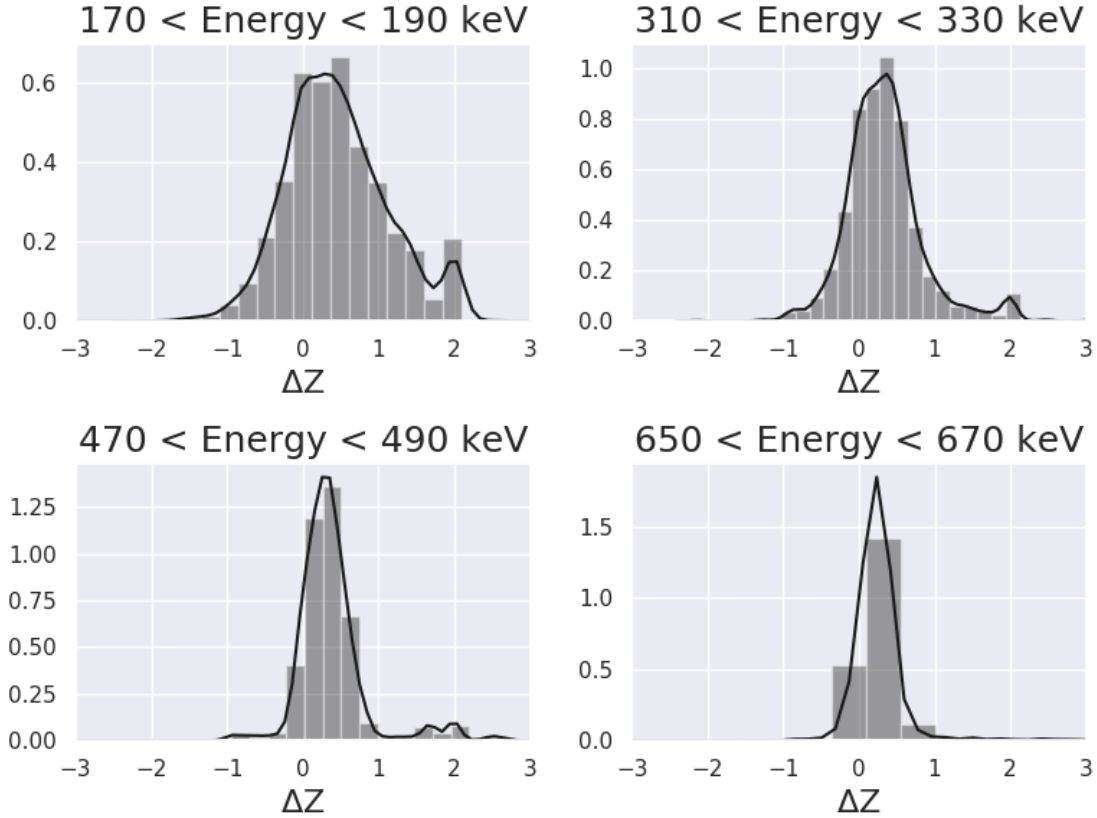


Figure 2.18: Difference in single-pixel event depth estimated by SRF and CAR for various energy ranges.

Despite the increase in computational complexity, SRF reconstruction pays dividends in energy resolution for multiple-pixel events. The SRF is derived from a single-pixel event devoid of the WPCT that afflicts multiple-pixel events, and it effectively allows that waveform to be reconstructed in the absence of the distorting effects of WPCT in the transient regime. It does not completely mitigate the effect of WPCT, however, as the amplitude is still subject to underestimation. For this reason, multiple-pixel events still require the WPCT correction described in Section 2.4.3. Nevertheless, SRF can achieve significant improvement for multiple-pixel

events [45].

### 2.4.5 Subpixel Energy Calibration

SRF reconstruction estimates event properties by matching observed signals to predetermined templates. These templates correspond to the system responses averaged over a small volume of the detection medium. While this methodology works well for voxels with little response variation, the template for a voxel with spatial response variation may be biased for a significant fraction of the interactions in that voxel.

As discussed in Section 2.4.2, subpixel position sensitivity is achievable. It may be leveraged to specifically address any systematic error due to nonuniform spatial response. The subpixel energy calibration methodology closely resembles the basic procedures presented in Section 2.4.1: each virtual detector volume is assigned a specific energy conversion factor based on the photopeak event signal amplitude for events within that detector region. The difference between subpixel energy calibration and the more traditional approaches are the size of these detector regions. Subpixel position-sensitivity enables one to partition the detection volume more finely, and it targets detector regions with small-scale response variation more effectively.

Figure 2.19 demonstrates the utility of subpixel energy calibration, in which the pixel-specific energy resolution observed at 662 keV is compared between the traditional and subpixel energy calibrations. The subpixel approach achieves the desired effect as the energy resolution improves for the majority of the interior anode pixels. However, it fails to address intrapixel variations in the exterior pixels where the worst energy resolution is generally observed.

Recall from Equations 2.30 and 2.31 that subpixel position sensitivity relies on the comparison of the transient signal amplitude induced on the opposing neighbor pixels. These relationships do not apply to exterior pixels, as they lack the requisite

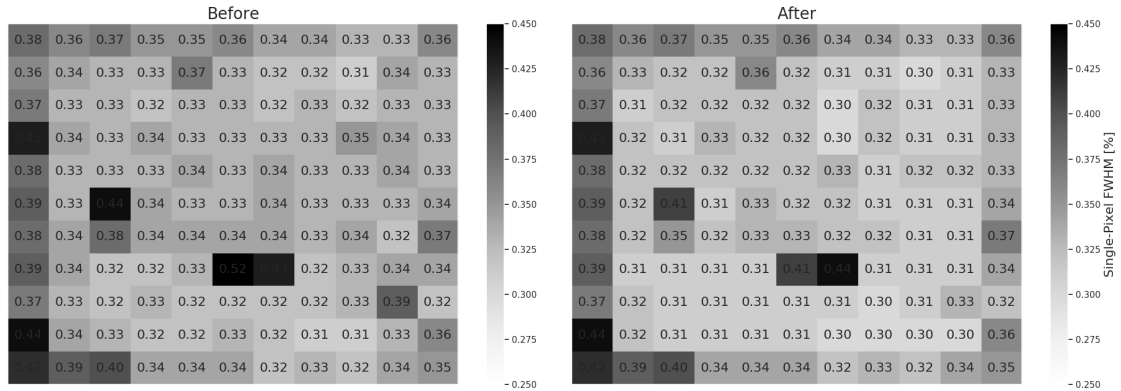


Figure 2.19: Single-pixel energy resolution at 662 keV, expressed in FWHM, as a function of the pixel location for traditional energy calibration (left) and subpixel energy calibration (right).

number of adjacent pixels. Therefore, subpixel energy calibration is not applicable to the exterior pixels, which comprise approximately 40% of the detection volume.

Subpixel energy calibrations require lengthy calibration measurements to acquire a sufficient number of events for each of the finely discretized detector voxels. This requirement can be burdensome, as typical applications of this technique may require up to 48 hours of data acquisition for a single detector module. For this reason, its use is primarily confined to research applications and material characterization.

## CHAPTER III

# Principal Component Analysis Methodology

Despite the wealth of information embedded in digitized waveforms, conventional reconstruction techniques do not fully leverage this information. Reconstructions based on trapezoidal filtering are primarily concerned with the amplitude of signals induced on triggering anodes and the cathode; energy deposition and depth of interaction are calculated entirely from these parameters. SRF improves this approach by using all of the information encoded in a triggering waveform to find a suitable waveform template. It reduces the dimensionality of the observations from an order of hundreds to less than ten (i.e., signal amplitude and depth of interaction).

While SRF more effectively leverages the information provided by digitized waveforms, it is inherently limited by human intuition. It categorizes events according to a set of attributes specified by a human operator - 3-D position, amplitude - without consideration of additional sources of response variance. Herein lies the *raison d'être* for applications of PCA for CdZnTe detector data.

Like the reconstruction methods that precede it, PCA reduces the dimension of the high-dimensional waveform data. However, it identifies and quantifies attributes that distinguish pixelated CdZnTe detector observations in a fundamentally different way. PCA exploits the statistical properties of the underlying data to find the attributes that account for the most variance between the observed waveforms, and it

provides a systematic procedure for quantifying these attributes for individual waveforms without relying on human intuition to guide its analysis.

The subsequent sections describe the formulation of PCA and demonstrate its usefulness in the context of analyzing digitized CdZnTe data. The ensuing discussion of latent variables produced by this analysis provides a critical foundation for concepts presented in Chapter IV. It does not provide a thorough description of any one particular algorithm used to perform PCA. Those interested in numerical linear algebra algorithms suited for this analysis are referred to the works of Trefethen & Bau [56] and Golub & Van Loan [57].

### **3.1 Principal Component Analysis Theory**

In essence, PCA summarizes data by a new set of characteristics. Like all useful summaries, the most vital ideas are distilled into a set of information that is more easily consumed and processed than the original content. In the context of this work, PCA summarizes the most vital features from a high-dimensional set of observed waveforms.

PCA achieves dimensionality reduction by finding orthogonal features in data that account for a large degree of variance between observations. The degree to which the dimensions of an observation may be reduced depends on the orthogonality of the dimensions. Orthogonal dimensions of data contain information that cannot be obtained from any other dimension, and are therefore essential to thoroughly describing that observation. By contrast, dimensions possessing strong correlations to another can be accurately estimated by knowing the value of another dimension.

Consider the sampled neighbor pixel waveform for a single-pixel event in Figure 3.1. Each of the 160 samples of a single waveform constitute a dimension of the data. Ignoring the influence of electronic noise in the samples, the amplitudes in the baseline and tail regions are roughly constant. With knowledge of the amplitude in

these regions, the values of the dimensions in the entire region may be inferred with a high degree of confidence. Therefore, the dimensionality in these regions is relatively low.

The transient region of the signal, however, has several attributes that have less correlation with the surrounding samples. Even with knowledge of one of the values in this region, there is limited capacity for predicting the amplitude of adjacent samples. Such values depend heavily on the the path of the collected charge carriers. The amplitudes in this region account for a significant amount of the variance observed between events, and the dimensions in this region are critical for approximating this observation in a reduced number of dimensions. Such signal attributes provide useful information for characterizing the event.

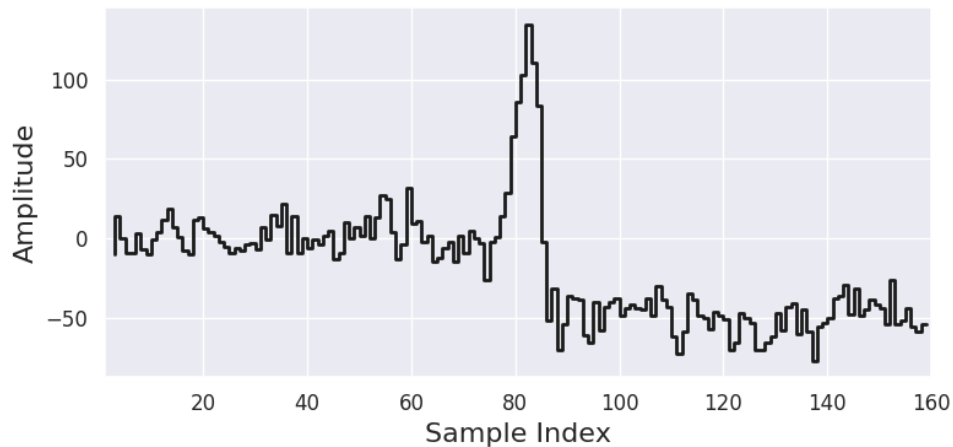


Figure 3.1: Generic neighbor pixel waveform for a single-pixel event.

PCA identifies a linear transformation of the data in which the dimensions are orthogonal to one another. By this approach, the original high-dimensional data can be faithfully represented by a relatively small number of dimensions. Of these dimensions in the linear transformation, those that account for a large proportion of the variance among observations are necessary to properly characterize the observation.

This foundational concept deserves a tangible example to translate abstract de-

descriptions to a more intuitive understanding of the subject matter. Consider a collection of football players, ranging from the preternatural talents of the sport - those in the realm of Cruyff or Messi - to those less noteworthy players. These players may be evaluated in several dimensions (e.g., agility, ball control, speed), but not all of them significantly distinguish the players from one another. For example, the ability to maneuver with and command the ball varies drastically among football players, and it distinguishes those on the fringes of lower tier clubs from legends of the sport. Some attributes, however, explain very little variance between players. All players have two functional legs, and it is trivial to evaluate players on this basis.

According to Hotelling's work on the matter, a linear transformation can be determined by maximizing the variance between observations [58]. Let  $\mathbf{v}$  represent a vector that maps the original data,  $\mathbf{y}$ , to a new projection space. The value in this space, the principal subspace, is the principal component of  $\mathbf{y}$ . Given a covariance matrix,  $\Sigma$ , the variance in this projected space is modeled by Equation 3.1.

$$\text{Projected Variance} = \mathbf{v}^T \Sigma \mathbf{v} = \frac{1}{N} \sum_i (\mathbf{v}^T \mathbf{y}_i - \mathbf{v}^T \bar{\mathbf{y}})^2 \quad (3.1)$$

Equation 3.1 must be optimized with a constraint lest the variance tends towards infinity. From first principles of calculus, this is performed by determining the eigenvector at which the derivative with respect to  $\mathbf{v}$  is constant. Without loss of generality, normalizing the inner product of  $\mathbf{v}^T \mathbf{v}$  to a value of 1 satisfies this constraint, and it may be enforced by means of a Lagrangian multiplier (Equation 3.2).

$$0 = \frac{\partial}{\partial \mathbf{v}} [\mathbf{v}^T \Sigma \mathbf{v} + \lambda (1 - \mathbf{v}^T \mathbf{v})] \quad (3.2)$$

$$0 = 2\Sigma \mathbf{v} - 2\lambda \mathbf{v} \quad (3.3)$$

The result in Equation 3.3 implies that the optimized vector  $\mathbf{v}$  must be an eigen-

vector of the covariance matrix, and the Lagrangian multiplier forms an eigenvalue. To further simplify, multiply Equation 3.3 by  $\mathbf{v}^T$ .

$$\mathbf{v}^T \Sigma \mathbf{v} = \mathbf{v}^T \lambda \mathbf{v} \quad (3.4)$$

$$\text{Projected Variance} = \lambda \quad (3.5)$$

The maximum variance obtained in the principal subspace corresponds to the maximum eigenvalue of the data covariance matrix. For the specific case of digitized data from CdZnTe, the length of the observations  $\mathbf{y}$  corresponds to the number of samples in the digitized waveforms. As such, the covariance matrix  $\Sigma$  has dimensions  $n \times n$ , and there are  $n$  eigenvalues of varying magnitude. The decomposition of the covariance matrix into these  $n$  eigenvalues and their corresponding eigenvectors is the familiar eigendecomposition.

Eigenvectors map the observations to a subspace; the variance in this subspace is measured by its corresponding eigenvalue. Therefore, the features that distinguish the observations most effectively (i.e., the features that contribute the most to the explained variance between observations) are measured by the eigenvalue magnitude. These eigenvectors are orthogonal. They provide unique information about a single observation that cannot be obtained from any of the remaining  $n - 1$  eigenvectors.

The mutual orthogonality of eigenvectors results from the symmetric nature of the covariance matrix [59]. If the corresponding eigenvalues of two eigenvectors are distinct,  $\lambda_i \neq \lambda_j$ , then the eigenvectors must be orthogonal. Consider the inner product of eigenvectors  $\mathbf{v}_i$  and  $\mathbf{v}_j$  in Equation 3.6. According to the definition of an eigenvalue, the quantity  $\lambda_i \mathbf{v}_i$  is equivalent to  $\Sigma^T \mathbf{v}_i$ . By a similar argument, the quantity  $\lambda_j \mathbf{v}_j$  is equivalent to  $\Sigma^T \mathbf{v}_j$ . The covariance matrix must be symmetric, which produces the equivalent statement in Equation 3.7.

$$\lambda_i \mathbf{v}_i \cdot \mathbf{v}_j = \Sigma^T \mathbf{v}_i \cdot \mathbf{v}_j \quad (3.6)$$

$$= \mathbf{v}_i \cdot (\Sigma \mathbf{v}_j) \quad (3.7)$$

$$= \mathbf{v}_i \cdot (\lambda_j \mathbf{v}_j) \quad (3.8)$$

$$= \lambda_j \mathbf{v}_i \cdot \mathbf{v}_j \quad (3.9)$$

According to the final equation (Equation 3.9),  $\lambda_i \mathbf{v}_i \cdot \mathbf{v}_j$  and  $\lambda_j \mathbf{v}_i \cdot \mathbf{v}_j$  are equivalent. Considering that the initial condition states that the eigenvalues are distinct, the only way in which equivalence is achieved is if the inner product of the corresponding eigenvectors evaluates to 0.

The process of decomposing the original waveform data into eigenvectors may be achieved by singular value decomposition (SVD). Consider a data matrix,  $A$ , with  $m$  observations; any  $m \times n$  matrix can be decomposed according to the relationship in Equation 3.10 in which matrices  $U$  and  $V$  are orthogonal matrices, and  $S$  is a diagonal matrix. The matrix  $U$  consists of the eigenvectors of the matrix formed by  $AA^T$ , while the eigenvectors of the  $A^T A$  constitute the columns of  $V$  as modeled by Equations 3.11 and 3.12, respectively [59]. Therefore, the diagonal entries of the  $m \times n$  matrix  $S$  comprise the singular values and, equivalently, the eigenvalues of  $A^T A$ . The diagonal matrix  $S$  obtains full rank when  $m \geq n$ .

$$A = USV^T \quad (3.10)$$

$$AA^T = (USV^T)(VSU^T) = USSU^T \quad (3.11)$$

$$A^T A = (VSU^T)(USV^T) = VSSV^T \quad (3.12)$$

Despite seemingly different approaches between the eigendecomposition of the data

covariance and the decomposition by SVD, the two approaches are equivalent. If  $Y$  represents the column-wise centered data matrix of  $A$  (as it was similarly presented in Equation 3.1), the covariance is modeled by Equations 3.13 and 3.14. The latter represents the eigendecomposition into the orthogonal eigenvectors in the columns of  $V$ , and the diagonal matrix  $\Lambda$  contains all eigenvalues  $\lambda_i$ .

$$\Sigma = \frac{1}{m-1} Y^T Y \quad (3.13)$$

$$= V \Lambda V^T \quad (3.14)$$

The matrix of eigenvectors  $V$  is equivalent to the right-singular values of Equation 3.10. To relate the two approaches, the singular values of the diagonal matrix  $S$  and the diagonal matrix of eigenvalues  $\Lambda$  may be equated by replacing the centered data matrix  $Y$  with its SVD (Equation 3.15).

$$\Sigma = \frac{1}{m-1} Y^T Y = \frac{1}{m-1} V S U^T U S V^T = \frac{1}{m-1} V S^2 V^T \quad (3.15)$$

The diagonal entries of  $S$  from SVD,  $s_i$ , are equivalent to  $\sqrt{(m-1)\lambda_i}$ . Note that the data matrix  $A$  must be centered in order for these two approaches to achieve the same result. While the magnitude of eigenvalues and singular values differ, the effect is negligible as the relationship between singular values and eigenvalues (i.e.,  $\lambda_i = \frac{1}{m-1}s_i^2$ ) is a monotonic relationship in  $s_i$ . Therefore, the ranking of eigenvalue magnitude does not change under conversion to singular values. The eigenvector that accounts for the most explained variance under the eigendecomposition of the covariance remains the same under SVD.

The eigendecomposition and SVD produce functionally identical results, but they differ in other practical considerations. SVD is the preferred method owing to the

numerically stable and efficient algorithms used in performing the decomposition. Contemporary algorithms for SVD use a divide-and-conquer approach that minimizes the costly data communication and provides backward stability [60]. The QR algorithm commonly used for eigendecompositions does not achieve the same standard for stability.

### 3.2 Interpretation of Principal Components

Common critiques of statistically-driven techniques include the opacity of the decision-making processes. In wide-ranging applications from quantitative equity trading to autonomous vehicle development, such systems can be called a “black box”, owing to the lack of transparency in the way in which algorithms arrive at a conclusion [61, 62].

The applications of PCA do not deserve the derogatory term “black box”. In a minor concession, the principal components produced by this analysis can be abstract; they are calculated by the inner product of an observation and an eigenvector. However, there are practical methods that derive physical meaning from otherwise opaque calculations.

The first of which requires a trial-and-error approach, and it entails visualizing the correlation between principal components and readily observed quantities. In the specific case of analyzing pixelated CdZnTe event data, there are well-known event properties that can account for significant variance in the observed waveforms. The most notable property that satisfies this criterion is the depth of interaction. Due to the pixelated geometry and the corresponding anode weighting potential, the induced amplitude for fixed energy deposition varies with the depth of interaction as was demonstrated in Figure 2.8. This property also produces visible changes in the waveforms: the slope of the signal rise and the amplitude of the neighbor pixel tail region change according to the depth of interaction.

This intuition can be confirmed in Figure 3.2, which visualizes the reconstructed depth of interaction to the first principal component for a generic anode pixel. This figure reveals that the relationship between the two quantities yields a prominent correlation. While the correlation is not always sufficient to prove causality, one can confidently assert that the first principal component provides complementary information to the depth of interaction.

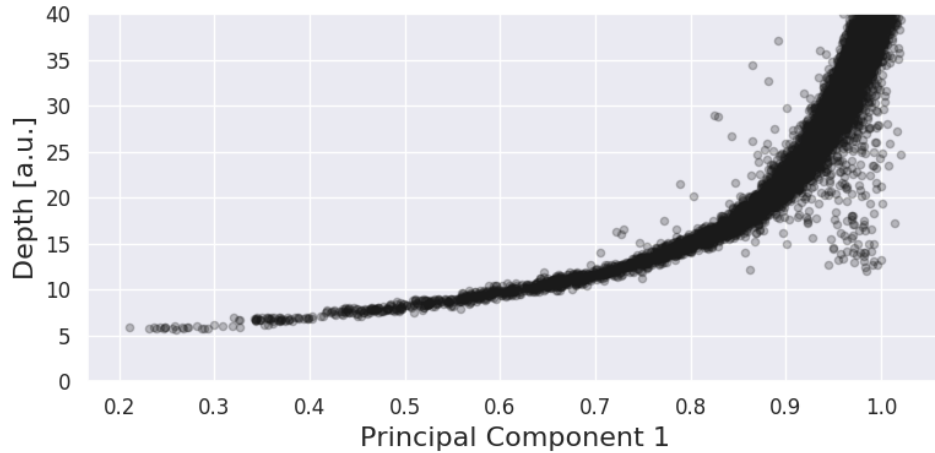


Figure 3.2: Reconstructed depth of interaction as a function of the first principal component obtained from the decomposition of single-pixel event data from a generic anode pixel.

The underlying mechanisms described by principal components may not always correlate significantly with readily observed parameters. For more thorough analysis, one can examine the eigenvector that produces the principal component. Recall that principal components result from the projection of a data vector onto a principal subspace. More explicitly, the principal component is the inner product of the eigenvector and that data vector, or equivalently, a weighted sum of the data vector.

The eigenvector reveals which samples in the data vector are most positively or negatively weighted. Indices with a low-magnitude weight may be considered insignificant to the the principal component. This analysis is demonstrated in Figure 3.3 in which the first principal eigenvector is juxtaposed with a sample observation.

The data vector contains the majority of the samples from the collecting pixel and the right, top, left, and bottom adjacent pixels for a single-pixel event.

From examination of the eigenvector in the top pane, it is apparent that the regions that contain the anode signal rise and the neighbor signal tails obtain positive, high-magnitude weighting. From principles of semiconductor detector physics, these signal segments are highly correlated with depth; anode-side interactions often include a more rapid rise time and neighbor tail amplitudes lower than the baseline. These observations are consistent with the correlation presented in Figure 3.2. Anode-side interactions obtain a low first principal component, while cathode-side interactions obtain a higher value for the first principal component.

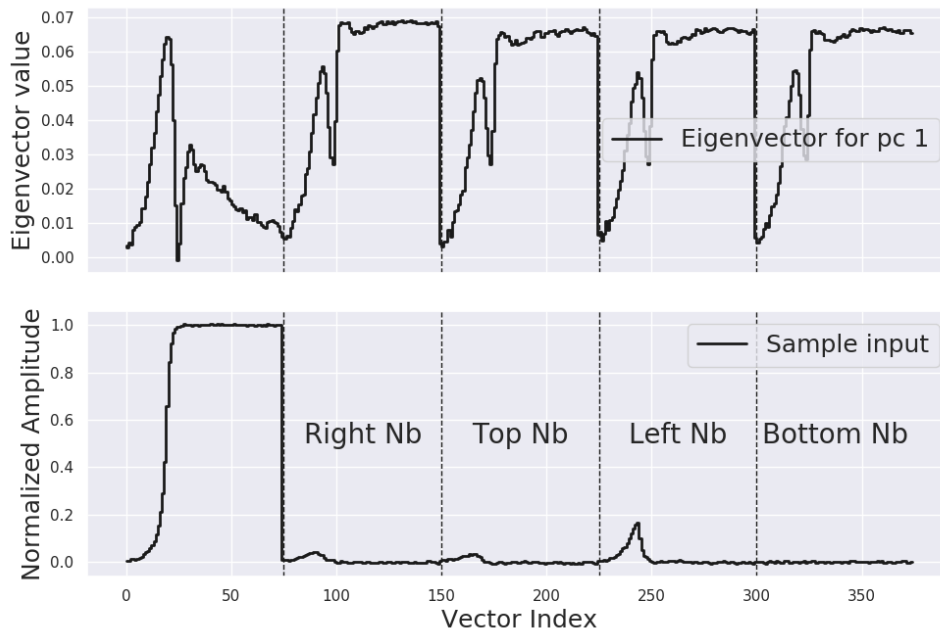


Figure 3.3: Eigenvector that maps data to the first principal eigenvector (top) and a sample data vector for juxtaposition (bottom).

For further confirmation, one can corroborate the findings from the eigenvectors by identifying data vectors that score excessively low and high with respect to the first principal component as demonstrated in Figure 3.4. The waveforms from these two categories should be distinguished by the waveform segments that correspond to

indices of high magnitude in the eigenvector. As expected by the eigenvector, the anode signal rise and neighbor tail regions are visibly different for the two categories of waveforms.

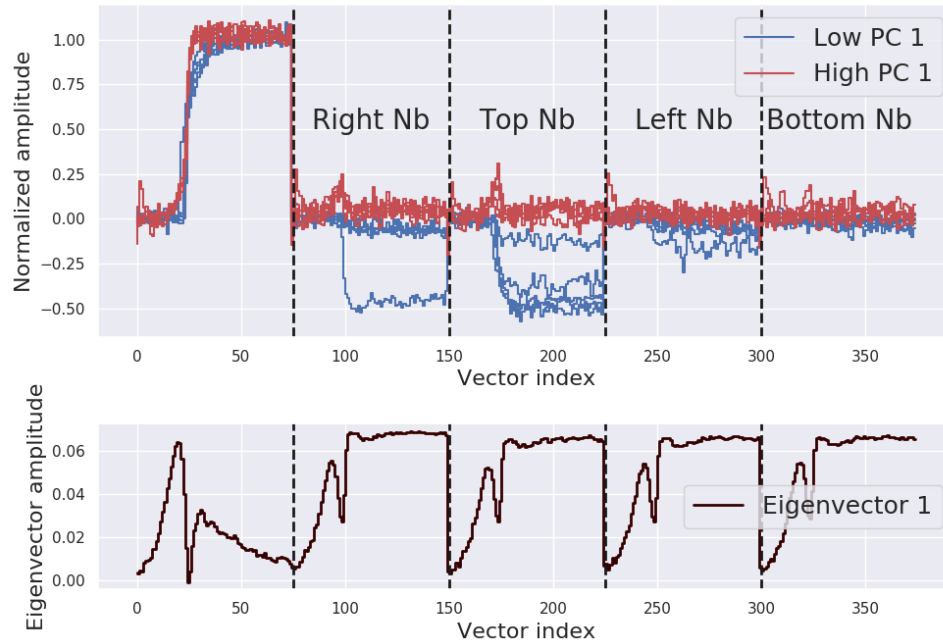


Figure 3.4: Waveform vectors with excessively low and high first principal component scores (top) and the eigenvector responsible for the projections (bottom).

## CHAPTER IV

# Energy Reconstruction by Principal Component Regression

The PCA process extracts signal properties that may be otherwise overlooked by conventional reconstruction methods. To fully leverage this information, one must pre-process waveform data to ensure that PCA extracts relevant information, and the principal component values must be translated to physical event properties. This chapter addresses these tasks specifically for energy reconstruction of single-pixel events. Performance metrics and practical aspects - such as analysis of model complexity, overfitting and sensitivity to electronic noise - follow in subsequent sections. Supervised variants of PCA are introduced in the final sections as means for improving performance.

While only single-pixel events are analyzed in this chapter, the presented methods build a foundation for analyzing more complicated event structures in Chapters V and VI, in which the adaptations required for applying these methods to multiple-pixel events and high-energy events, respectively, are discussed in more detail.

## 4.1 Data Preprocessing

While each pixelated anode occupies a similar area, the material underneath the effective pixel area may differ due to localized crystal defects or concentrations of trapping impurities [63, 64]. Exterior pixels exhibit additional deviations from the theoretical weighting potential profiles due to what Shor, Eisen & Mardor describe as ‘edge effects’ [65]. For these reasons, single-pixel events are separated and analyzed according to the pixel in which charge is collected, ensuring that pixel-specific information is captured by PCA.

The data vectors subject to PCA should capture all relevant information about the charge-carrier paths to extract the most pertinent event properties. At one extreme, this includes signals induced on all anode pixels and the cathode. However, this presents challenges in data acquisition and *a posteriori* processing. As mentioned in Section 2.3, system dead time depends heavily on the number of digitized waveforms. The digitization of all anode pixel signals comes at the costly expense of detection efficiency. Furthermore, very little charge is induced on pixels that reside far away from the collecting pixel. The cost of including the signal induced on these pixels is not justified by the return in additional information about a given event.

One must also consider the constraints of performing PCA on such a large data matrix and storing the requisite waveforms in memory. In consideration of execution time, waveforms are stored in random-access memory (RAM) for rapid access during the analysis. While this promotes fast execution, it imposes constraints on the memory to tens of GB for modern computers. For contemporary SVD algorithms, the number of operations also depends heavily on the dimensionality. Golub & Van Loan state that the complexity of such algorithms adhere to  $O(mn^2 + Bn^3)$ , where  $m$ ,  $n$  and  $B$  are the number of observations (rows), number of dimensions of an observation (columns) and a constant, respectively [57]. This provides additional incentive to limit the length of data vectors. Due to these considerations, at most four neighbor

pixel signals are included in the data vector. This ensures that information encoded in pixels close to the collecting pixel are included in the analysis while limiting the length of data vectors.

One must also decide whether to include the cathode signal. Intuitively, the cathode signal provides limited information about the charge carrier path, apart from the depth of interaction, due to its planar geometry. However, even this quantity may be inferred from other signal components. As demonstrated in Section 3.2, depth can be effectively captured from the collecting and neighbor pixel signals.

The inclusion of the cathode signal can be more definitively determined by examination of eigenvalues. Recall from Section 3.1 that the eigenvalues measure the variance explained by a given principal component, where explained variance serves as a proxy for the ability to distinguish observations. It is expected that the addition of the cathode signal should add more explained variance due to the increased dimensionality of the data vector. To more accurately compare the effect of the cathode signal, the eigenvalues for the first three principal components are normalized by the total number of dimensions in Table 4.1. Based on the first three principal components, using the cathode signal increases the explained variance for single-pixel events. While this is an admittedly heuristic comparison, it merits the inclusion of the cathode signal. Empirical evidence further suggests that it does improve single-pixel energy resolution by an order of 0.01% in absolute terms with little additional computational resources.

Table 4.1: Comparison of single-pixel event eigenvalues normalized to data vector length with and without the cathode signal included

Principal Component	With Cathode Signal	Without Cathode Signal
1	0.50	0.35
2	0.086	0.052
3	0.056	0.042

PCA is performed using events of varying induced signal amplitudes to avoid overfitting to events within a narrow energy range. The signal amplitude also contributes to the explained variance of events, but it is not considered crucial for the purposes of PCA. Amplitude is readily quantified without the aid of principal components, and its relationship to energy is trivial. Rather, it is more pertinent to analyze the scalable aspects of waveforms (e.g., rising signal slope and width). To control for the effects of signal amplitude, data vectors are normalized to the amplitude of the signal induced on the collecting pixel. Methods for translating the principal components to energy deposition for all events is deferred to the subject matter in Section 4.3.5.

Waveforms may also vary due to artifacts in the data acquisition process. For example, all signals may be shifted in time due to the configuration of the front-end electronics. The capacitive cells that store the signal amplitude for a given electrode constantly revolve and overwrite, and the rising portion of the acquired signal may start at any of the samples in the frame. It is only after data acquisition that the signal rise is centered in the frame. While algorithms are implemented to align the signal rise to the center of the frame, some misalignment still occurs as demonstrated in Figure 4.1. It is pertinent to align similar points of waveform inflection in the same data matrix column to more precisely compare scalable waveform features (e.g., point of initial signal rise, the shape of the waveform as it reaches its maximum amplitude). Therefore, waveforms are aligned to a common point of reference within a frame to achieve this precise comparison.

Note that this alignment requires truncation of the waveform to properly align the waveforms. This entails discarding some signal samples at the beginning and end of the waveform frame. The dimensionality of these regions is low, and the cumulative effect of discarding these samples on the analysis is negligible.

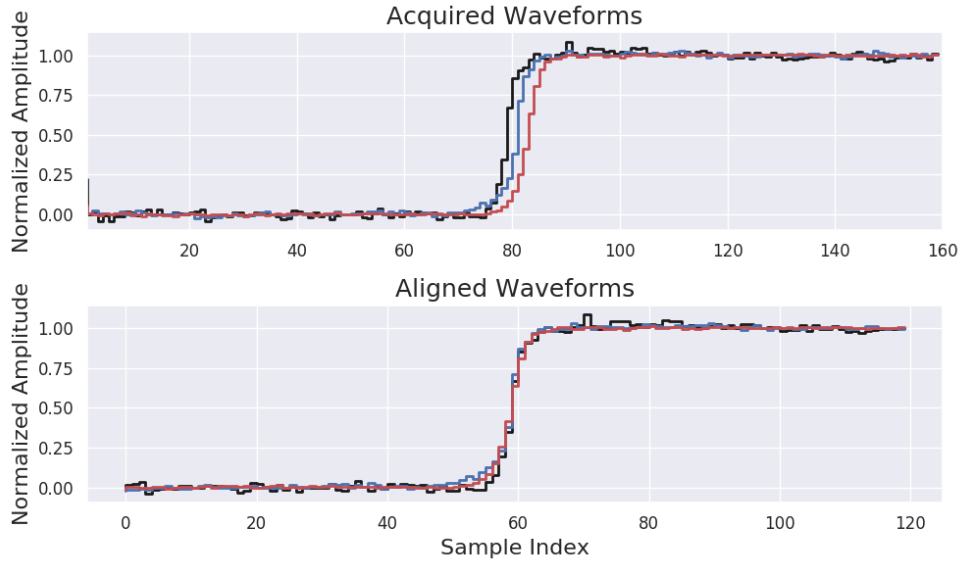


Figure 4.1: Normalized, collecting pixel waveforms as they are acquired (top) and the aligned waveforms used for PCA (bottom).

## 4.2 Principal Component Regression

Principal components obtained from the original waveform data reveal information about systematic error in the reconstructed energy deposition. To compensate for systematic trends in estimated energy deposition, they must be modeled as a function of principal component values. Alharbi proposed this correction methodology to compensate for the depth-dependent response in planar CdTe detectors [66]. While this approach was implemented for a planar CdTe detector to great effect, it utilized only the first principal component. The methods presented in this section derive from this approach, but they are heavily adapted to address the unique challenges of position-sensitive CdZnTe detectors. This section also introduces a methodology to utilize the information encoded in multiple principal components to more thoroughly compensate systematic error in reconstructed energy deposition.

For the pixelated CdZnTe detectors in question, the initial energy reconstruction corrects for the depth-dependent response as discussed in Section 2.4.1. Therefore, the relationship between reconstructed energy and the first principal component -

consistently correlated with the depth of interaction - may yield no obvious systematic trend. As demonstrated in Figure 4.2, data must be separated by depth to visualize and regress systematic trends more completely.

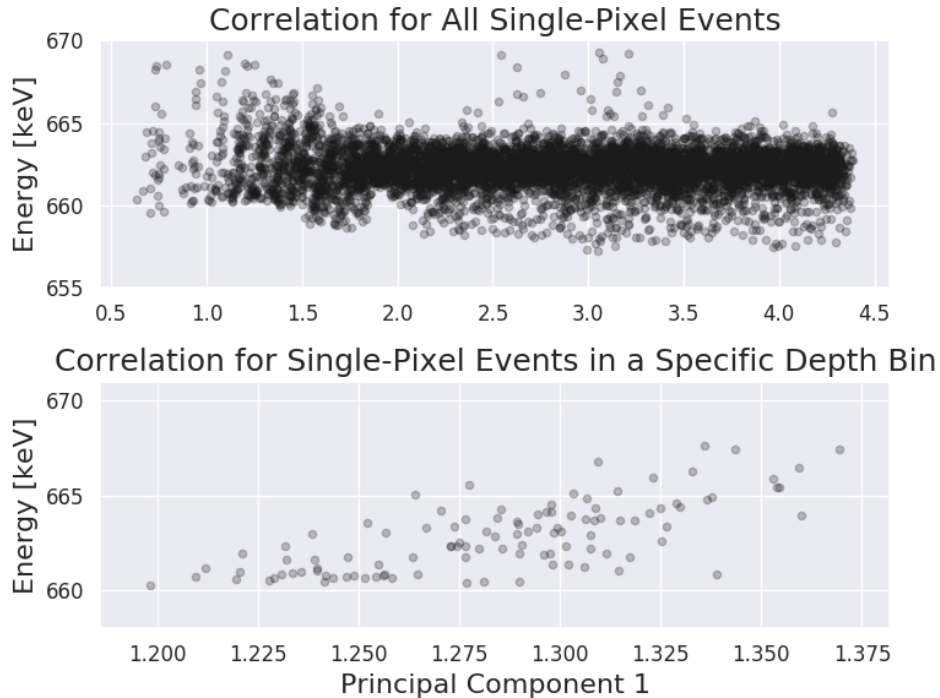


Figure 4.2: Correlation between reconstructed energy and the first principal component for all events (top) and for a specific depth bin near the anode surface (bottom).

In practice, systematic trends are regressed by a linear model. As this does not reflect any theoretical model of the systematic error, this could be considered a Procrustean bed<sup>1</sup>. However, a linear model is the pragmatic choice to limit model complexity for systematic trends.

Linear models predominantly use ordinary least squares (OLS) to estimate the slope and intercept. However, this method is notoriously susceptible to the influence of outliers. Such outliers may originate from front-end electronics interference or incomplete energy deposition from background radiation that coincidentally falls

<sup>1</sup>The term “Procrustean bed” refers to the unorthodox methods of Procrustes. According to Greek mythology, he adjusted the height of his guests at his inn to conform to the size of his bed by unnecessarily cruel methods.

within the energy window of interest. To prevent outliers from corrupting the linear model of prevailing systematic trends, the relationship between reconstructed energy and principal components are regressed by a Theil-Sen estimator [67, 68].

OLS operates under the assumption that the random noise for each observation is homoscedastic. Outliers violate this assumption, and they can significantly distort the linear regression as demonstrated in Figure 4.3. The Theil-Sen estimator does not rely on such assumptions. Rather it designates the median slope between all unique pairs of points as the trend slope. The median statistic provides a robust estimator of the linear model; nearly 30% of the data may consist of outliers without degrading the accuracy of the Theil-Sen estimator [69].

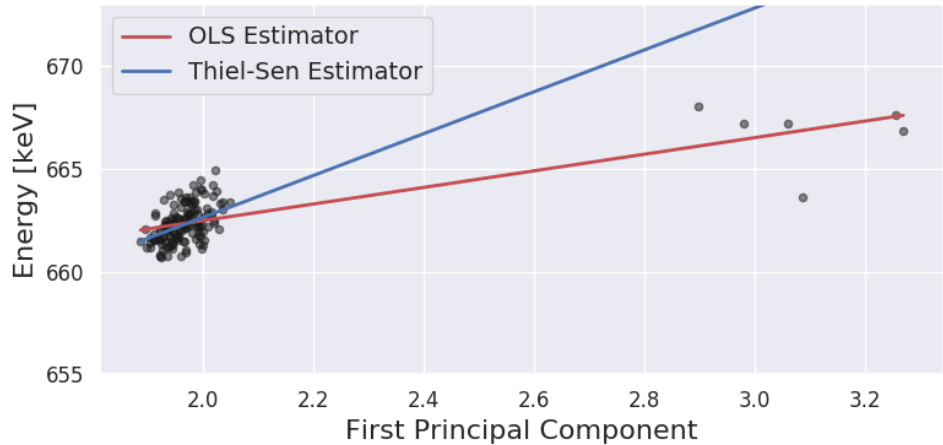


Figure 4.3: Linear regression of energy and principal component correlation with apparent data outliers.

To mitigate systematic error, data are projected along the regressed trend. As presented in the top-left pane of Figure 4.4, the initial correlation between energy and principal component contains a significant, systematic trend. The FWHM of the corresponding energy histogram in the top-right pane is significantly reduced after projecting that same data along the regression as shown in the bottom two panes.

The regression and correction process demonstrated in Figure 4.4 can be repeated for each principal component. Recall from Section 3.1 that eigenvectors with distinct

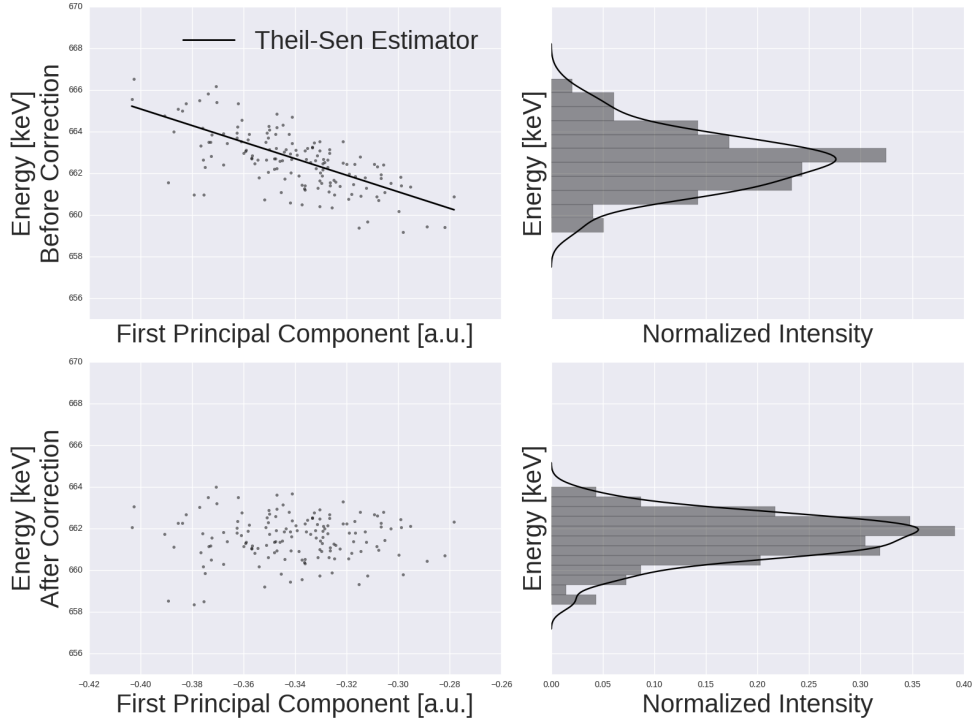


Figure 4.4: Correlation between the energy deposition estimate and principal component before (top-left with the corresponding histogram in the top-right) and after (bottom-left with the corresponding histogram in the bottom-right) projecting the data long the regressed trends.

eigenvalues must be orthogonal. Therefore, one may perform this correction procedure for each principal component serially without affecting the corrections based on any proceeding principal components.

Consider the correlations presented in Figure 4.5. The energy values featured in the first pane are the initial estimates obtained after depth-correction. The systematic trend with respect to the first principal component is regressed, and the initial energy estimates are updated by the process of projecting the data along the line of regression. At this point in the procedure, there is still demonstrable systematic error in the reconstructed energy. The results of this projection replace the initial energy estimates, and these values are subsequently correlated with the second principal component in the second pane of Figure 4.5. This process is repeated to obtain a second update of the energy reconstructed for each of the single-pixel events in

question. By the third iteration of this procedure, the systematic trend as a function of the third principal component appears nearly constant and signifies the effective mitigation of systematic error in the energy estimates.

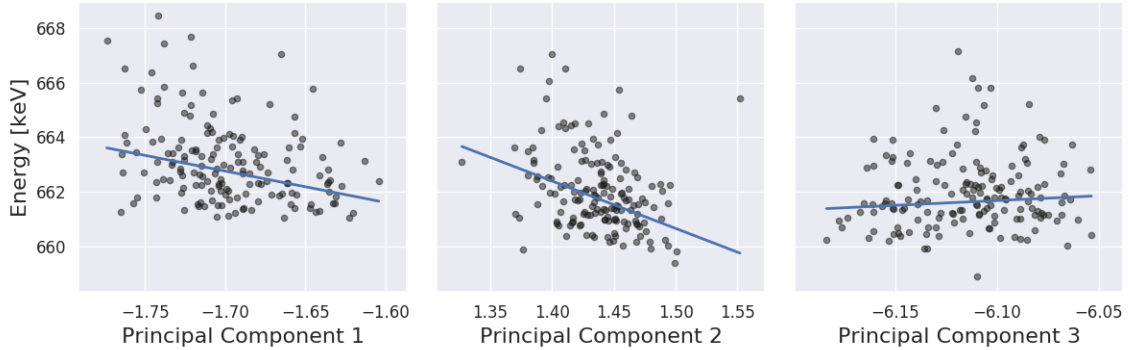


Figure 4.5: Updated energy estimates as a function of the first three principal components after regressing and projecting along each systematic trend.

### 4.3 Results for Single-Pixel Events

The PCA and regression methodology described in the preceding sections require a  $^{137}\text{Cs}$  calibration measurement. Events within an energy window around 662 keV are collected for each channel, and the ensuing principal component regression procedure generates energy calibration parameters that may be saved in a look-up table for subsequent measurements. Corrections are applied on an event-by-event basis and lends well to real-time processing applications.

The energy reconstruction process for a single event follows a procedure that closely resembles the example depicted in Figure 4.5. Principal components for an event are generated by projecting the corresponding waveform data onto the channel-specific eigenvectors stored in memory. The energy of each event is iteratively updated for each principal component using the linear model coefficients determined by principal component regressions.

The efficacy of the principal component methodology can be evaluated by comparing the single-pixel results against results of conventional methods for a  $^{137}\text{Cs}$  calibration measurement. For the purposes of this analysis, the first five principal components are used to update energy estimates. This is an arbitrarily low amount of principal components; selection of the number of principal components is discussed in greater detail in Section 4.3.1.

For thorough analysis, energy resolution metrics for the 662 keV photopeak are displayed for each pixel as a function of the pixel location in Figures 4.6 and 4.7. These figures compare the energy resolution obtained with conventional energy reconstruction methods against the updated performance after leveraging the information from principal component regressions. The energy resolution metrics, FWHM and full width at tenth maximum (FWTM) in Figures 4.6 and 4.7, respectively, are color-coded for enhanced visualization. Good performance obtains a light shade of gray, while darker shades indicate worse energy resolution.

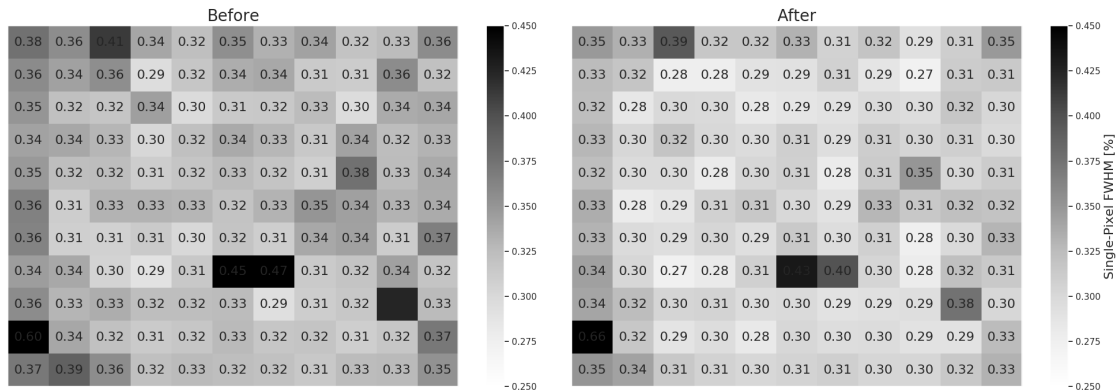


Figure 4.6: Single-pixel FWHM observed at 662 keV for each anode pixel using conventional energy reconstruction methods (left) and the FWHM after updating energy estimates according to principal component correlations (right).

For the vast majority of anode pixels, the FWHM improves between 1 - 10% relative to the baseline performance established with conventional reconstruction meth-

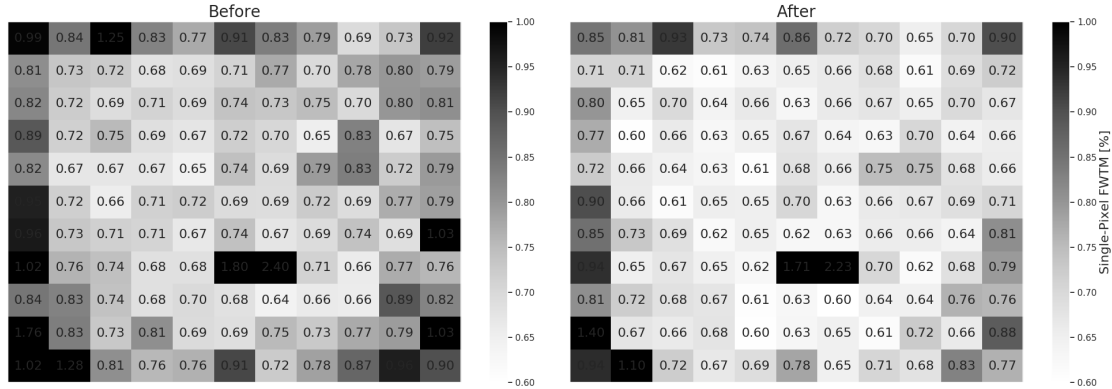


Figure 4.7: Single-pixel FWTM observed at 662 keV for each anode pixel using conventional energy reconstruction methods (left) and the FWTM after updating energy estimates according to principal component correlations (right).

ods. To understand the underlying cause of the improvement, the analysis must revert back to the abstract concepts presented in Section 3.2. Examination of eigenvectors provides valuable insight into the origin of the improvement. They indicate the specific mechanisms and event attributes of the underlying principal components. In the interest of brevity, the first five eigenvectors are displayed for only two pixels. This includes the central anode pixel and one of the corner pixels to capture the prevailing eigenvectors for a pixel with little and significant intrapixel response variation, respectively.

The corresponding eigenvectors are displayed in Figure 4.8. Note that the corner pixel has only a neighboring pixel to the right and above the collecting pixel. Therefore, the last two segments of the eigenvectors in the bottom pane have effectively no amplitude. The first and second eigenvectors for both pixels give significant weight to the cathode and neighbor signal tails. The second eigenvector gives relatively more weight to the cathode signal rise, and it therefore gives more consideration to the slope of the rising cathode signal. It is reasonable to infer that the two most significant principal components are heavily dependent on the depth of interaction.

Beyond the first two principal components, the eigenvectors for the pixels signify different event properties. The third and fourth eigenvector for the interior pixel give little weight to the collecting anode pixel and cathode signals. Rather, combinations of the neighbor pixel signals have significant magnitude and opposing polarity. For example, the third principal component has negative weight for the top neighbor tail and positive weight for the bottom neighbor tail. It signifies the subpixel proximity of the charge carrier paths to the top and bottom adjacent pixels. The same rationale applies to the fourth eigenvector, which measures the subpixel proximity to the right and left adjacent pixels.

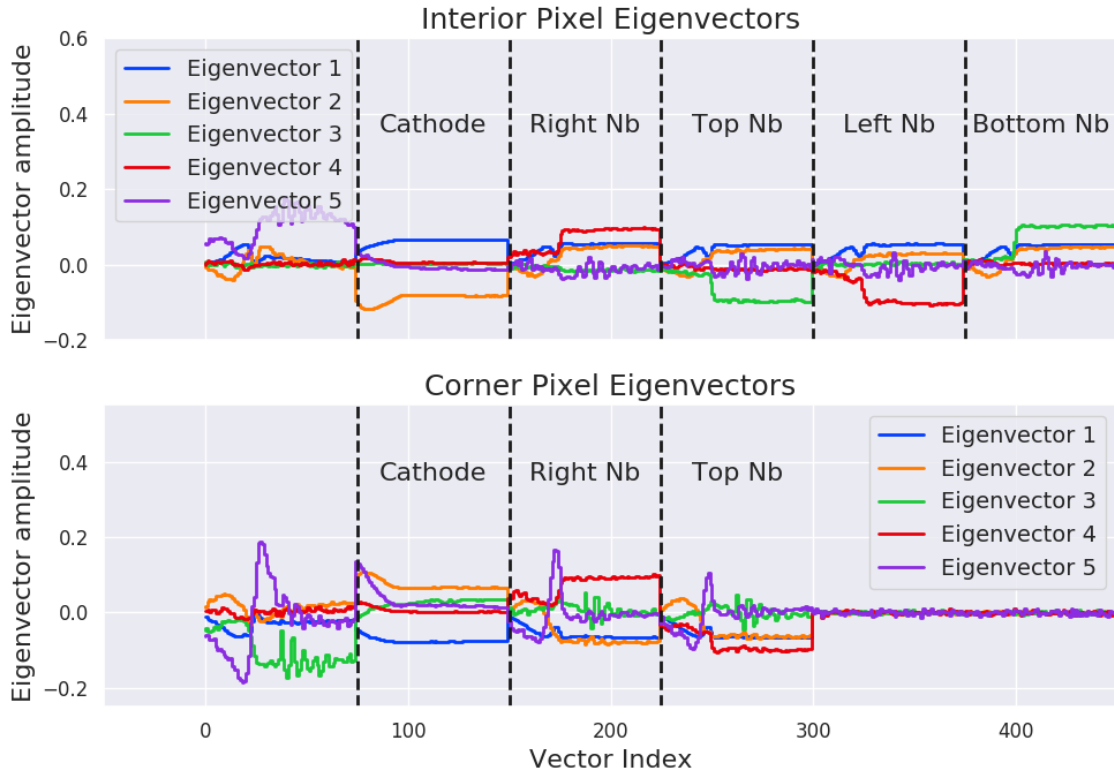


Figure 4.8: First five eigenvectors for an interior pixel (top) and a corner pixel (bottom).

The last remaining eigenvector for the interior pixel is most heavily weighted for the collecting pixel signal tail. It identifies abnormalities in the collecting pixel as

demonstrated in Figure 4.9. Waveform vectors with excessively high and low fifth principal components accentuate the primary signal feature in the collecting anode signal rise. Vectors with low principal components have an abnormal inflection that may be attributed to a single-pixel event in which there are two distinct interactions under one pixel. Yang implemented an event filter to identify these events for digitally filtered waveforms [44], but principal components and the subsequent regressions identify and compensate for the systematic error in energy at a far lower computational expense.

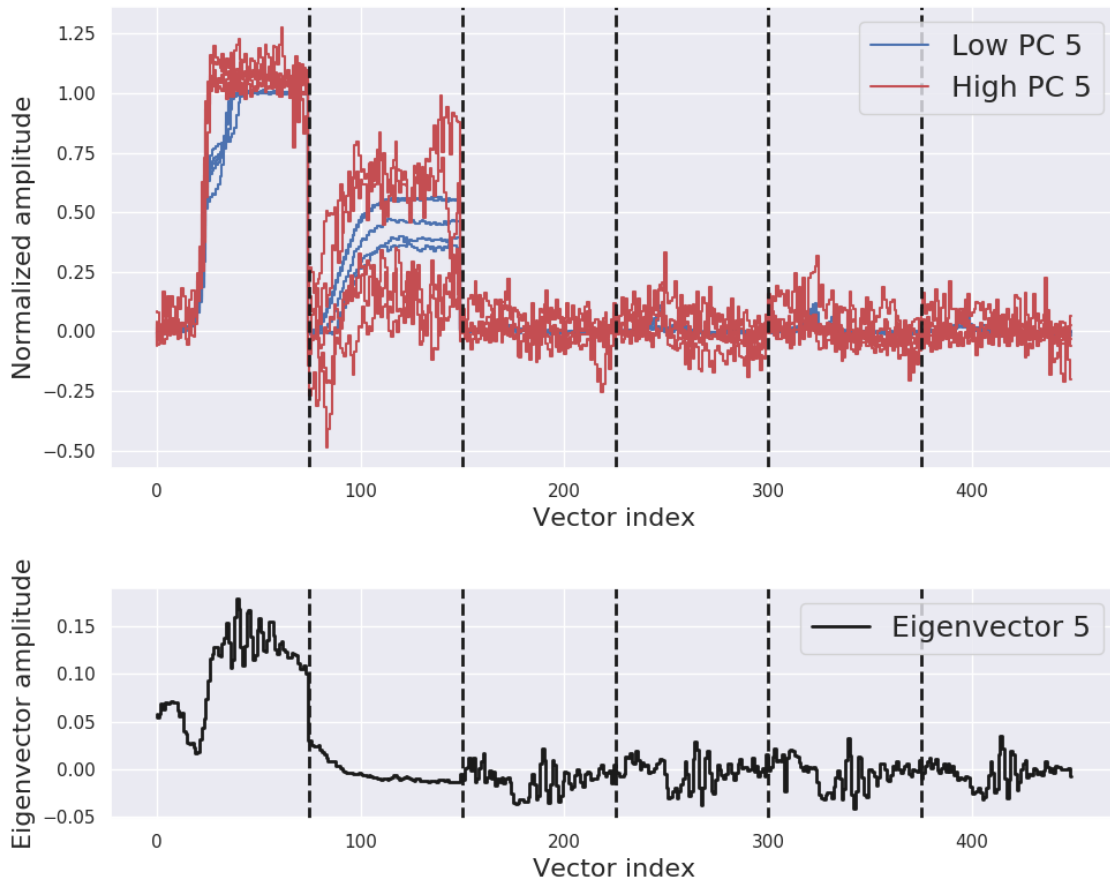


Figure 4.9: Waveform vectors with excessively high and low fifth principal components for an interior pixel (top) and the corresponding eigenvector (bottom).

The corner pixel eigenvectors extract similar event properties as those for the in-

terior pixel, albeit in a different order. The third eigenvector for the corner pixel identifies events with abnormal signal rise inflection in a similar fashion to the fifth eigenvector of the central pixel in Figure 4.9. The fourth and fifth eigenvectors indicate the proximity to the neighboring pixels and the relative amplitudes of the neighbor pixel signals to the collecting pixel signal, respectively. Based on observations of pixelated CdZnTe detectors, relatively poor energy resolution is expected from exterior pixels [50]. The PCA methodology addresses these flaws to some extent. However, the improvement in exterior pixel energy resolution significantly outperforms that of interior pixels in FWTM only, as displayed in Figure 4.10.

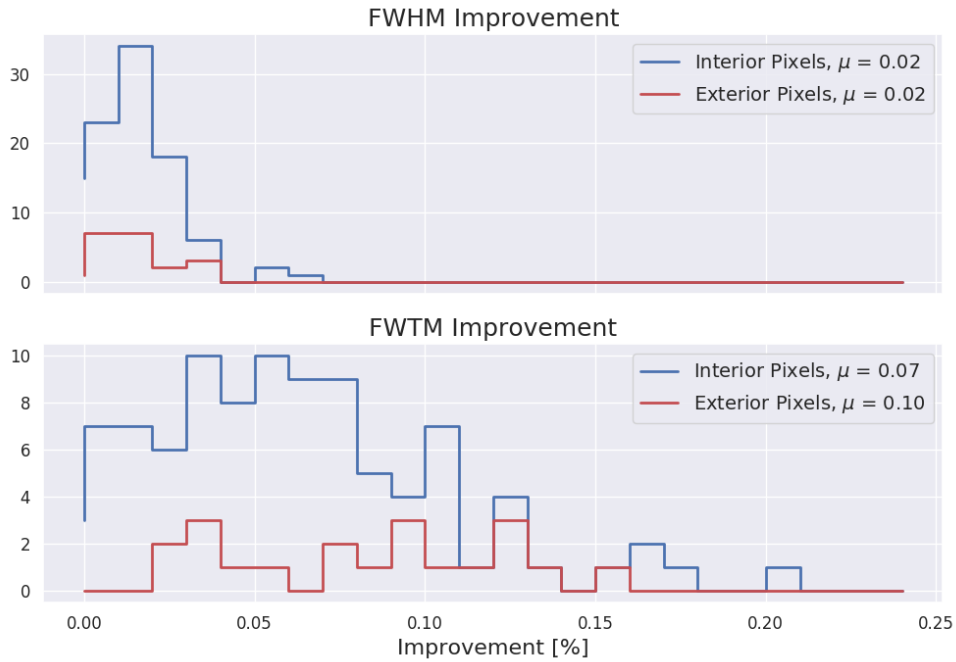


Figure 4.10: Energy resolution improvement at 662 keV for exterior and interior pixels with respect to FWHM (top) and FWTM (bottom).

Figure 4.11 displays the aggregate single-pixel energy spectrum, making note of the 10% relative improvement in FWHM and FWTM. The right pane plots the pixel-specific energy resolution obtained after principal component corrections as a function of the original energy resolution. The line  $y = x$  provides a reference, and it corresponds to no net change in energy resolution. The vast majority of pixels fall

below the reference line, regardless of the initial energy resolution.

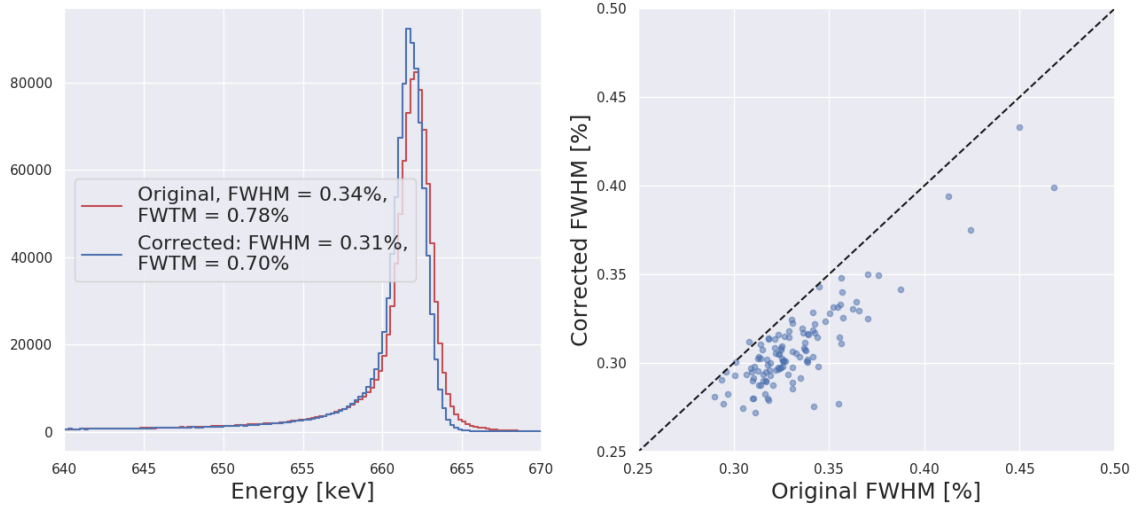


Figure 4.11: Aggregate single-pixel event energy spectrum obtained before and after principal component regressions (left) and the pixel-specific improvements for the original and corrected energy spectra (right).

According to the aggregate energy spectra in Figure 4.11, the low-energy tail persists. It provides evidence of the limitations to principal component regression. Even with the addition of more principal component corrections - and at the risk of severely increasing model complexity - the low-energy tail is not mitigated. This observation presents three, mutually exclusive conclusions: the source of the low-energy tail originates from a source of unexplained variance, PCA cannot produce reliable signatures of the source of the low-energy tail, or the systematic error from this flaw is encoded in subsequent principal components. The last explanation is unlikely; the cumulative variance explained by principal components beyond 200 account for less than 5% of the total explained variance. It is also unlikely that this results from a source of unexplained variance - sources of variance that occur randomly. As noted by Bolotnikov [63], this primarily occurs when charge is lost to the gap between pixels. Therefore, it should theoretically be encoded in the principal components that are strongly influenced by the lateral position of the charge carrier paths. This leaves the

second conclusion as the prevailing hypothesis.

### 4.3.1 Selection of the Number of Principal Components

The number of principal components used in PCA regression is a free parameter; its value is not determined by any physical or theoretical properties of the system, but rather it is chosen by the user. To make an informed decision on its value, it is critical to understand the influence of the number of principal components on system performance to strategically choose its value.

Recall from Section 3.1 that the eigenvectors produced by SVD arrange in such a way that the first principal component explains the most variance, the second principal component explains the next highest amount, and so forth. This principle is demonstrated by Figure 4.12, which features the cumulative variance explained (i.e., cumulative eigenvalues normalized to one) as a function of the principal component rank. This convex trend increases monotonically at a rapid rate for an exterior pixel and, to a lesser extent, an interior pixel. As the principal component rank increases in magnitude, the underlying mechanism distinguishes the waveform vectors less effectively. Beyond a certain principal component, the systematic trends in the reconstructed energy become increasingly insignificant compared to random noise.

The energy resolution trends in Figure 4.13 support this claim. The variance explained by a principal component and the net improvement in energy resolution after applying its correction correlate positively at low principal components. The greatest improvement in energy resolution occurs after the correction derived from the first principal component, but the energy resolution approaches an asymptotic value after correcting for subsequent principal components.

The results featured in Figure 4.13 were obtained using self-calibrated data, implying that the performance was evaluated for the same data set from which the energy calibration parameters were derived. Under these self-calibration circumstances,

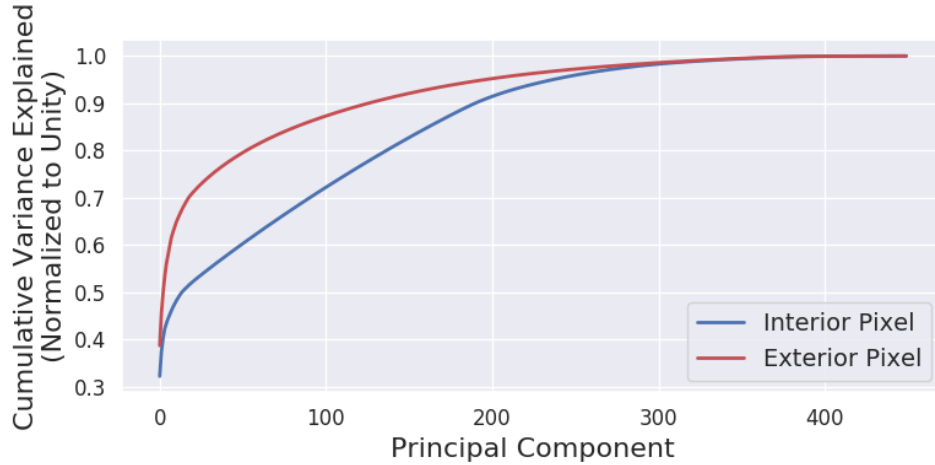


Figure 4.12: Cumulative explained variance of single-pixel events as a function of principal component for two anode pixels.

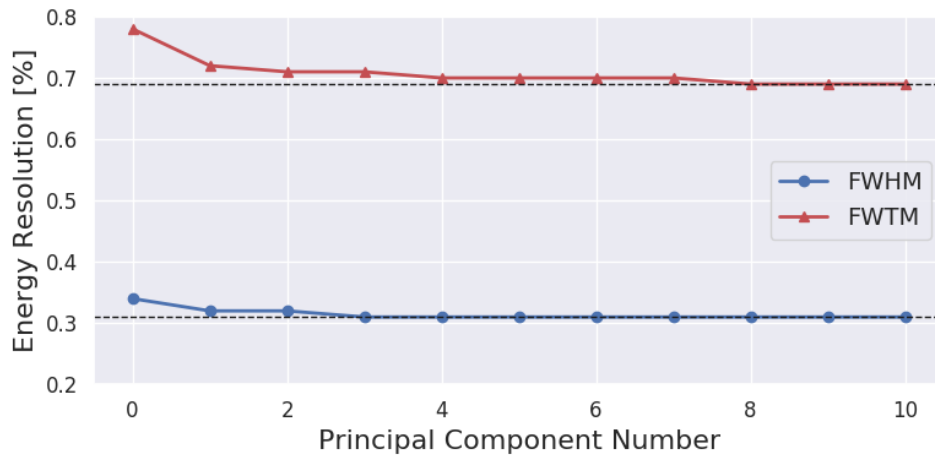


Figure 4.13: Single-pixel energy resolution metrics as a function of the number of principal component corrections. Asymptotic values are indicated by dotted lines.

energy resolution should improve monotonically within the constraints of statistical noise. However, this does not accurately reflect the expected performance of out-of-sample data.

Regressions with respect to principal components from calibration measurement data are subject to statistical and electronic noise, and deviations in the regression model coefficients depend on the random noise present in the calibration data.

Self-calibrated performance does not suffer from this random noise, regardless of the regression model complexity, as the regression coefficients are optimal given the exact noise patterns in the calibration measurement data. However, out-of-sample measurement performance degrades, as it is effectively impossible to replicate the exact noise patterns that were present in the calibration measurement data.

The severity of out-of-sample performance degradation depends on model complexity. As the model increases in complexity - or equivalently, as more principal component corrections are used - the model gains flexibility to adapt to the systematic trends in the calibration data. However, this may allow the model to overfit the calibration data. Bishop refers to this dilemma as the bias-variance trade-off [70]. If the model is kept simple by limiting the number of principal components, bias remains in the energy reconstruction procedure. However, if the model becomes overly complex, the principal component regressions develop increasing sensitivity to random noise in the calibration data. The variance of the estimated energy resolution increases in subsequent, out-of-sample measurements.

To gain intuition about this trade-off for single-pixel energy reconstruction, energy resolution at 662 keV for a generic detector was tabulated with varying degrees of model complexity in Table 4.2 to gain intuition about this trade-off. To approximate out-of-sample performance,  $k$ -fold cross-validation was implemented. This method divides calibration data into  $k$  partitions. For each of the  $k$  iterations, one of the partitions of the data is designated the test data, and the remaining  $k - 1$  partitions constitute the training data. Calibration parameters are regressed from the training data and subsequently used to process the test partition [71]. It allows one to approximate out-of-sample performance without exposing the system to extrinsic factors that may alter system performance between the calibration and out-of-sample measurements. Therefore,  $k$ -fold cross-validation isolates the degradation attributed to the stimulus in question - regression parameter error.

Despite increasing model complexity, the self-calibrated performance in Table 4.2 improves monotonically, and it benefits from over-fitting. However, the performance from the cross-validated test data indicates that the out-of-sample performance is optimal between 1 and 20 principal component corrections. Consistent with the bias-variance trade-off, energy resolution degrades as additional principal component corrections are applied beyond this model complexity. In light of the effects of model complexity - and in the interest for in-field applications - the number of principal component corrections are conservatively limited to five.

Table 4.2: Single-pixel energy resolution at 662 keV for self-calibrated data and cross-validation results

Principal Component	Self-Calibration		Cross-Validation	
	FWHM [%]	FWTM [%]	FWHM [%]	FWTM [%]
0	0.40	0.97	0.40	0.97
10	0.36	0.82	0.37	0.82
20	0.36	0.80	0.38	0.82
50	0.34	0.72	0.39	0.83
100	0.31	0.72	0.40	0.86
200	0.27	0.63	0.42	0.90

### 4.3.2 Sensitivity to Statistical and Electronic Noise

Although PCA and the subsequent regression enable significant improvement in energy resolution, the observed energy resolution does not meet the theoretical performance limit. A portion of this discrepancy may be attributed to pixelated detector design specifications (e.g., pixel pitch and gap width) [31], but some of the remaining discrepancy may be attributed to intrinsic factors of principal component regression. As discussed in Section 4.3.1, statistical noise adversely affects the accuracy of regression models as a function of principal component. Furthermore, electronic noise

in the initial energy estimates may degrade the accuracy of those same regression models.

To understand the sensitivity to statistical and electronic noise, these values are perturbed, and the resulting energy resolution metrics are monitored. Statistical noise is modulated by using various amounts of events per principal component regression, whereas Gaussian noise is added to the response variable in principal component regressions. For the latter, Gaussian noise is only imposed for the regression; it is not imposed on the final processed energy spectrum to avoid distorting the monitored energy resolution. All reported results in Tables 4.3 and 4.4 are obtained with five principal component corrections.

Both energy resolution metrics suffer significantly when the number of events used for each voxel's regressions are limited to a low number. They progressively improve as the event limit is raised and the statistical noise is reduced. When there is effectively no limit - corresponding to a limit of 500 events per voxel - the energy resolution recovers its unperturbed performance.

Table 4.3: Summary of single-pixel energy resolution as a function of the events used for principal component regression

Maximum Events Regressed	FWHM [%]	FWTM [%]
10	0.42	0.97
25	0.35	0.82
50	0.33	0.75
75	0.32	0.73
100	0.32	0.73
500	0.31	0.70

According to the energy resolution summarized in Table 4.4, electronic noise does not appear to limit the regression performance. Even with 2 keV electronic noise imposed on the response variable, the regressions produce similar performance to the

baseline performance established with conventional methods.

Table 4.4: Summary of single-pixel energy resolution as a function of the electronic noise added to the response variable

Additive Noise [keV]	FWHM [%]	FWTM [%]
0.25	0.32	0.71
0.50	0.32	0.71
0.75	0.32	0.72
1.00	0.33	0.72
1.25	0.33	0.73
1.50	0.33	0.74
1.75	0.34	0.75
2.00	0.34	0.76

The tabulated results suggest that statistical noise limits the efficacy of principal component regressions. This is far more preferable to the alternative. Electronic noise improvements require intricate front-end electronics design and careful consideration of detector electrode dimensions. As demonstrated in Table 4.3, statistical noise can be mitigated by allowing adequate calibration measurement time to collect a sufficient number of events.

### 4.3.3 Comparison to Sub-Pixel Energy Calibrations

Based on the single-pixel eigenvectors in Figure 4.8, PCA possesses potential to correct for intrapixel response variation. The first two eigenvectors account for depth-dependent systematic error, and the third and fourth eigenvectors embed information about the subpixel, lateral position. By forming corrections based on the regression of the resulting principal components, the PCA reconstruction methodology begins to encroach on the territory previously dominated by subpixel energy calibrations (Section 2.4.5).

The PCA methodology implicitly corrects for intrapixel variation through principal component regression. The same applies to the exterior pixels, in which some eigenvectors account for the lateral position as demonstrated in Figure 4.8. This reveals one of the primary advantages over subpixel energy calibrations; PCA addresses subpixel response variation for all pixels, not just those in which the lateral position can be precisely estimated. Subpixel energy calibrations cannot replicate the performance for exterior pixels, as the subpixel position in exterior pixels cannot be explicitly calculated.

The performance of these two alternatives is compared in Figure 4.14, in which the single-pixel FWHM values are plotted in correspondence to the location in the pixelated anode. While data were acquired in trigger+8 mode to obtain optimal position reconstruction for subpixel energy calibrations, only the signals from the four cardinal neighbor pixels were included in the PCA waveform vectors for the purposes of consistency. As before, the number of principal component corrections was limited to five to keep the PCA correction model relatively simple.

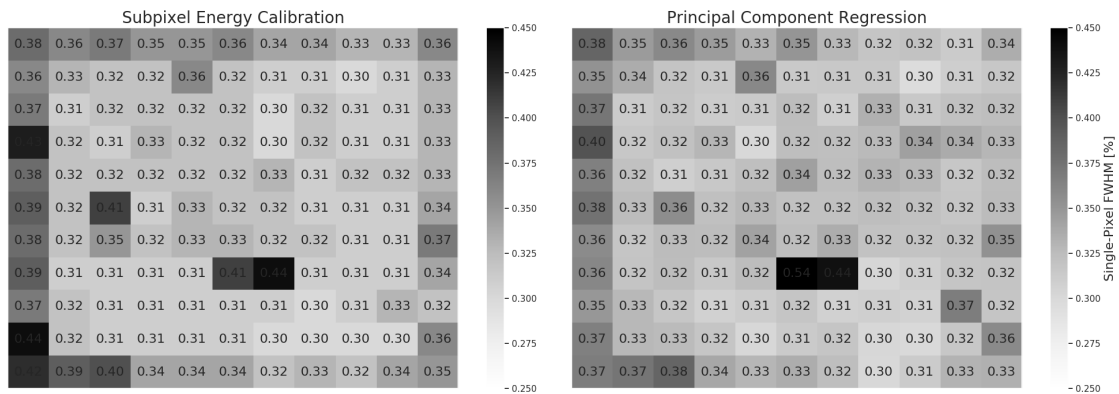


Figure 4.14: Single-pixel FWHM as a function of pixel location obtained by subpixel energy calibration (left) and PCA (right).

The performance of exterior pixels systematically improves under the PCA methodology, but PCA cannot consistently outperform the subpixel energy calibration metrics for interior pixels - at least not without risking overfitting by the addition of

more principal component corrections beyond the fifth principal component. It suggests that principal component corrections cannot entirely compensate for intrapixel variation to the same extent of the precise subpixel energy calibrations.

The PCA methodology provides another critical advantage over subpixel energy calibration. Recall that an excessive amount of events - which corresponds to upwards of 48 hours - must be acquired to generate energy corrections for each small detector volume with a high degree of statistical significance. The PCA methodology decreases the calibration time requirement by orders of magnitude compared to traditional subpixel corrections compared to traditional subpixel corrections.

Unlike subpixel energy calibrations - which requires eight neighbors to obtain optimal lateral position resolution - PCA only requires the four cardinal neighbors in its default configuration. PCA can perform identically using data acquired in trigger +8 mode and trigger +4 mode - the mode in which at most four cardinal neighbors are digitized per collecting pixel. As noted in Section 2.3, the system dead time depends heavily on the number of digitized waveforms. Therefore, operating in trigger +8 mode substantially decreases detection efficiency. This consideration also contributes significantly to the discrepancy in calibration times between the two competing methods.

#### **4.3.4 Event Processing Time**

Real-time processing applications - those that reflect the operating conditions for field applications - require fast event processing to account for all incoming events and maintain optimal detection efficiency. These demands limit the use of more computationally intensive reconstruction methods such as SRF. Therefore, reconstruction methods based on trapezoidal filtering are currently the primary choice for field operation.

Trapezoidal filters require a Fourier transform, complex number multiplication and

an inverse Fourier transform to the time domain for each acquired waveform. The transforms use the Fastest Fourier Transform in the West (FFTW) software library, in which the transform algorithms run in  $O(n \log n)$  time [72, 73]. The processing time for each event also requires fixed overhead to prepare for the trapezoidal filter and apply energy corrections.

PCA reconstruction methods rely on  $O(n)$  processes; the projection onto principal subspaces requires the inner product subroutine and the requisite processing overhead. Therefore, the processing time for an event depends heavily on the number of principal components used in the reconstruction. The software suite developed for these purposes make judicious use of the Intel Math Kernel Library (MKL) to accelerate processing speed for commonly used linear algebra subroutines [74].

Although the theoretical complexity of PCA methods compares well against the  $O(n \log n)$  behavior for trapezoidal filters, it is difficult to predict which method processes more quickly. In the case of trapezoidal filtering, the variable  $n$  refers to the length of the padded waveform in the Fourier domain - 256 indices - whereas  $n$  corresponds to the length of the waveform vector for the PCA methodology. The waveform vector length for a typical application of PCA is generally 450 indices.

The processing time is compared more definitively by the observed, single-pixel processing-time distributions in Figure 4.15, in which the processing time for each event of a calibration measurement data set was measured by a high-resolution timer from the C++ chrono library [75]. PCA reconstruction with the default five principal components provides a clear advantage over the alternatives, but PCA with an excessive amount of principal components becomes comparable to the processing time obtained by trapezoidal filtering.

The processing time distribution obtained for trapezoidal filtering varies far less than that of PCA. The filtering process is performed on only one waveform for the purposes of this analysis, and the number of operations is constant for all events.

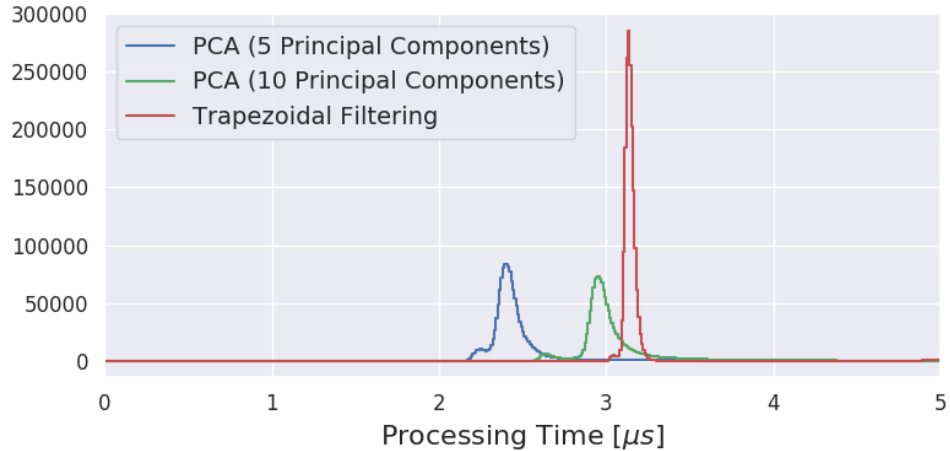


Figure 4.15: Single-pixel event processing-time distributions for various reconstruction methods.

However, the number of operations for PCA depends on the number of adjacent pixels to the collecting pixel. For single-pixel events, this can correspond to two (corner pixels), three (edge pixels, excluding corners) or four neighbors (interior pixels). Each neighbor pixel in the event must be normalized to the collecting pixel signal amplitude as described in Section 4.1, and this  $O(n)$  process for a variable amount of neighbors accounts for the greater variance observed in the PCA processing time distributions.

#### 4.3.5 Adaptations for Different Incident Gamma-Ray Energy

The results presented to this point examine the performance of the PCA methodology at the point of calibration, 662 keV. To accommodate energy reconstruction at other energies, the regression procedures must be agnostic of the true energy deposition. Consider the equation used to update the estimated energy deposition discussed in Section 4.2. When an event is processed, it must be projected along the regression line and scaled to the proper energy as modeled in Equation 4.1. The variables  $m$ ,  $b$  and  $x$  refer to the linear model slope, intercept and the principal component value, respectively. The quantity  $(E_{\text{Initial}} - mx)$  has units of keV, and it projects the energy value to a common point of reference - the y-axis where the principal component

value is zero. To ensure that this value is scaled properly to keV, it is multiplied by the conversion factor  $\frac{662}{b}$ .

$$E_{\text{Updated}} = (E_{\text{Initial}} - mx) \frac{662}{b} \quad (4.1)$$

The slope and energy conversion factor in Equation 4.1 are regressed for 662 keV photopeak events, therefore they are not applicable to other energies of interest. To accommodate all energies, these model parameters must be normalized to the true energy deposition. The revised regression model in Equation 4.2 addresses this concern, regardless of the calibration point ( $E_{\text{True}}$ ). While the equation for updating the energy estimate in Equation 4.1 only applies to 662 keV, its replacement in Equation 4.3 applies for all energies. This revised update equation implicitly assumes that the integral nonlinearity of the front-end electronics is negligible, which is generally true up to approximately 1 MeV for the ASIC design used for this work [44]. Events in which the energy deposition is greater than 1 MeV are addressed specifically in Chapter VI.

$$\frac{E_{\text{True}}}{E_{\text{Initial}}} = mx + b \quad (4.2)$$

$$E_{\text{Updated}} = E_{\text{Initial}} (mx + b) \quad (4.3)$$

The efficacy of the energy-agnostic technique may be visualized through a comparison of the single-pixel energy spectra of a plutonium source<sup>2</sup> reconstructed via PCA and SRF. Figure 4.16 highlights two energy windows of interest between 300 - 450 keV and 550 - 750 keV. In both of these regions, the advantage of PCA reconstruction of SRF is visually apparent. The peaks of the former contain higher maximum amplitudes, and the regions on either side of the peaks - colloquially referred to as “valleys”

---

<sup>2</sup>The source in question refers to a well-characterized,  $\alpha$ -phase plutonium source [76]

- are lower than that of the SRF spectrum. Both of these spectral features enhance the ability to resolve the characteristic photopeaks of various plutonium photopeaks.

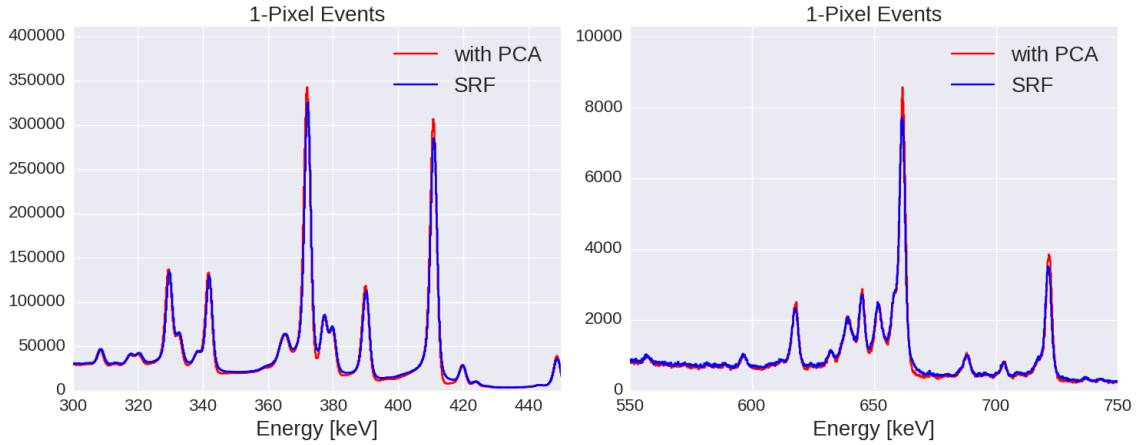


Figure 4.16: Processed BeRP ball spectrum obtained with PCA and SRF for the energy ranges of 300 - 450 keV (left) and 550 - 750 keV (right).

While PCA reconstruction applies towards all energies, its effectiveness varies as a function of energy. The fixed electronic noise of the subsystem comprised of the detector and front-end electronics account for a higher proportion of the total noise at lower energies. At progressively higher gamma-ray energy, the contribution from systematic error accounts for increasingly higher proportions of the total noise.

Principal component decomposition identifies sources of explained variance between the observed waveforms. Principal component regression can correct for such sources to an extent, but it offers no solution to the adverse effects of electronic noise - a source of unexplained variance. For this reason, the improvement of PCA relative to alternative methods of energy reconstruction increases as a function of the incident gamma-ray energy.

Consider the energy resolution trends as a function of gamma-ray energy for PCA and SRF in Figure 4.17. These results were obtained with a detector operating with a 3 MeV dynamic range, implying that the electronic noise is slightly higher than that of the previous results presented in this chapter that were obtained with a dynamic

range of 700 keV. At 238 keV, the comparative advantage for PCA is negligible. As the incident energy increases, the advantage progressively increases owing to the expected contributions of systematic error to the total error.

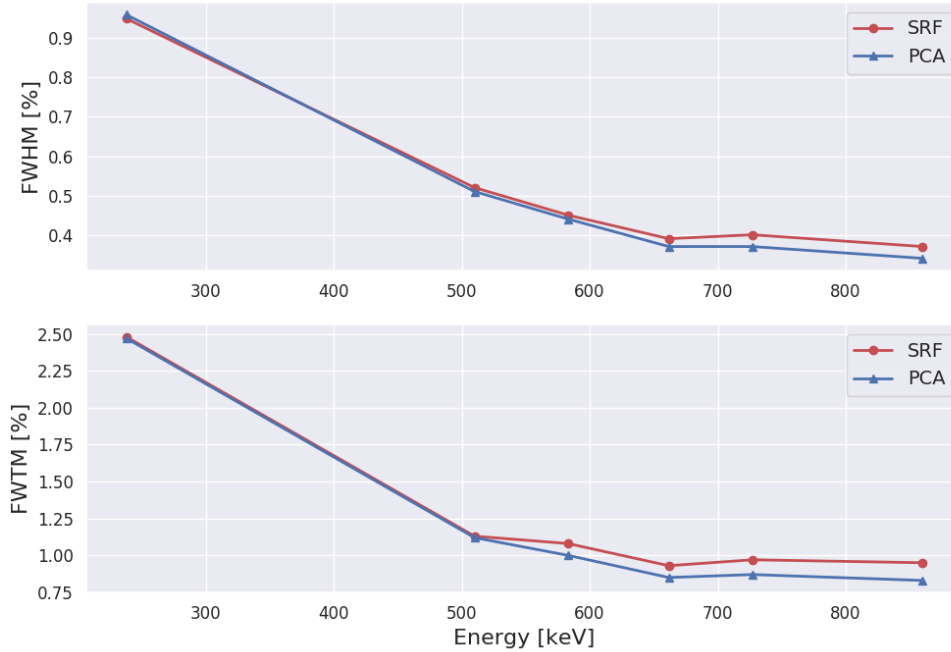


Figure 4.17: Energy resolution as a function of incident gamma-ray energy for PCA and SRF as measured by FWHM (top) and FWTM (bottom).

#### 4.4 Supervised Principal Component Analysis

The information provided by PCA is useful to the extent that it helps form predictive models for event parameters of interest. According to the formulation in Section 3.1, PCA decomposes data so that the data in a principal subspace has maximal variance. This does not necessarily imply that it provides the optimal predictive capability for a response variable like energy deposition.

Alternative methods address this by considering the response variable when performing decomposition; such methods are referred to as supervised principal component analysis (SPCA) as they include *a priori* knowledge of at least one response

variable to guide the analysis. In certain academic disciplines, the supervised methods may be designated by constrained PCA due to the consideration of a response variable in the formulation. By contrast, the decomposition presented in Section 3.1 is referred to as unconstrained PCA to distinguish it from the supervised alternatives. While many methods for performing supervised dimension reduction exist (e.g., Fisher’s discriminant analysis, partial least squares), two were chosen for further investigation primarily due to their reported prediction performance and the ability to interpret latent variables.

Bair et al. proposed decomposition of a data matrix comprised of only dimensions that depend heavily on the response variable [77]. The dependence between each dimension  $j$  and the response variable is measured according to the standardized regression coefficient in Equation 4.4, in which  $\mathbf{x}$  represents the  $j^{th}$  column of the data matrix, and  $\mathbf{y}$  is a vector containing the response variable. Only the dimensions in which the magnitude of the coefficient  $\beta_j$  exceeds a threshold are included in the data matrix.

$$\beta_j = \frac{\mathbf{x}_j^T \mathbf{y}}{\|\mathbf{x}_j\|} \quad (4.4)$$

The dimension selection process ensures that the response variable and the principal components have significant correlation and a meaningful regression model. The authors of this work demonstrate the utility of supervised decomposition by measuring the  $p$  value of a hypothesis test on the resulting regression between the response variable and the first principal component. With respect to the  $p$  value, the regression model formed from supervised principal components outperforms alternative methods by orders of magnitude.

The hypothesis test assigns a probability that the regressed model coefficients could be produced by chance. A low  $p$  value indicates that the null hypothesis, which assumes that there is no systematic trend in the data, is improbable. Low  $p$  values

provide evidence to reject such a null hypothesis, and it suggests that the regression coefficients are statistically significant given the probability distribution of possible coefficients. The validity of hypothesis testing is somewhat controversial; as Gill notes, the null hypothesis is not unique [78]. Estimates of the  $p$  value may vary due to the existence of different null hypotheses, leading some to criticize the validity of this significance test.

The method was replicated for the purposes of comparing waveform data. The threshold for the dependence metric,  $\beta_j$ , was heuristically selected by identifying the median value of  $|\beta_j| \forall j$ , thereby ensuring that only dimensions above the 50<sup>th</sup> percentile in dependence to the response variable are included in the decomposition. This implies that the number of columns in the reduced data matrix are half of that in the unconstrained PCA methods described in this chapter.

The eigenvectors produced by this heuristic approach are juxtaposed to those generated by unconstrained PCA for a generic anode pixel in Figure 4.18. The constrained PCA eigenvectors are padded with zeros as a matter of convenience; it allows one to align the eigenvector indices to those in the original waveform vectors, and it provides a modular way to project data onto principal subspaces regardless of the decomposition method.

The constrained eigenvectors lead to notable observations. The cathode signal does not appear, implying that it does not correlate strongly with the energy deposition deviation. Rather, these eigenvectors give significant weight to the transient anode signals - collecting and adjacent pixels alike - and there is emphasis on the anode signal tails. The comparison also suggests that the competing methods do not necessarily identify the same mechanisms through decomposition. For example, the third eigenvector for the unconstrained variety appears to distinguish waveform vectors by the proximity to the top or bottom neighboring pixels. It negatively weights the vector segment corresponding to the top neighbor pixel signal tail and positively

weights the segment for the bottom neighbor pixel signal tail. However, constrained PCA targets a different event property. Virtually no weight is given to neighbor pixels, but significant weight is placed on a portion of the collecting pixel signal tail.

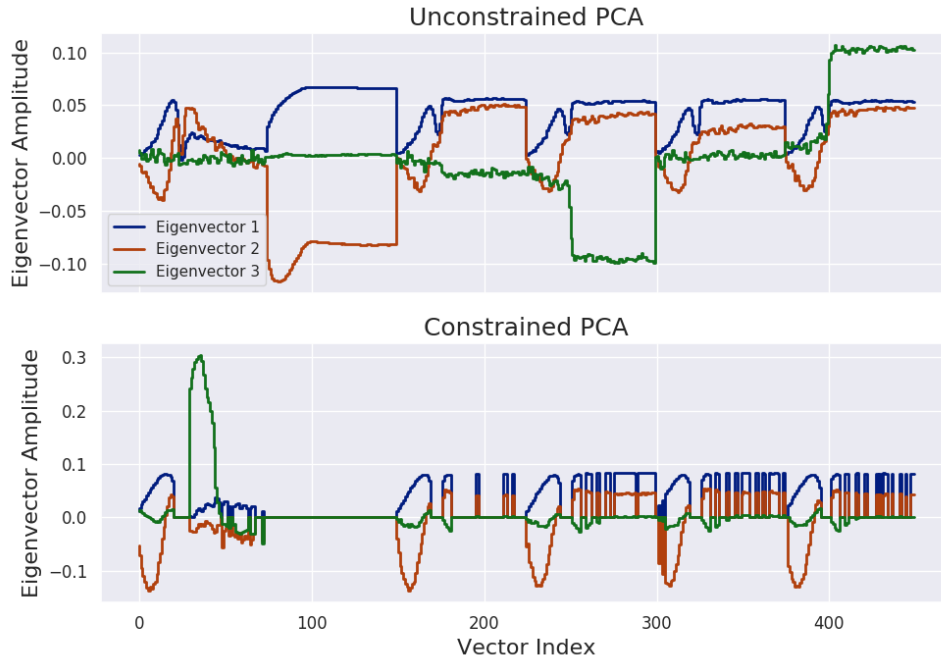


Figure 4.18: First three eigenvectors for events collected by a single, interior pixel using unconstrained PCA (top) and the using the constrained method described in Bair et al. (bottom).

Although Bair’s method for constrained PCA produced superior  $p$  values for the regressions featured in the seminal publication, the results for single-pixel waveform data are inconclusive as demonstrated in Figure 4.19. The  $p$  values of each regression with respect to the first three principal components are calculated using constrained and unconstrained PCA for one anode pixel. The  $p$  values are plotted against the depth bin in which the events for these regressions occur. The values produced by constrained PCA do not consistently produce better regressions. The processed energy spectra obtained with the competing methods reveal similar, uninspiring results for constrained PCA performance in Figure 4.20. The observed energy resolution is indistinguishable between the two methods.

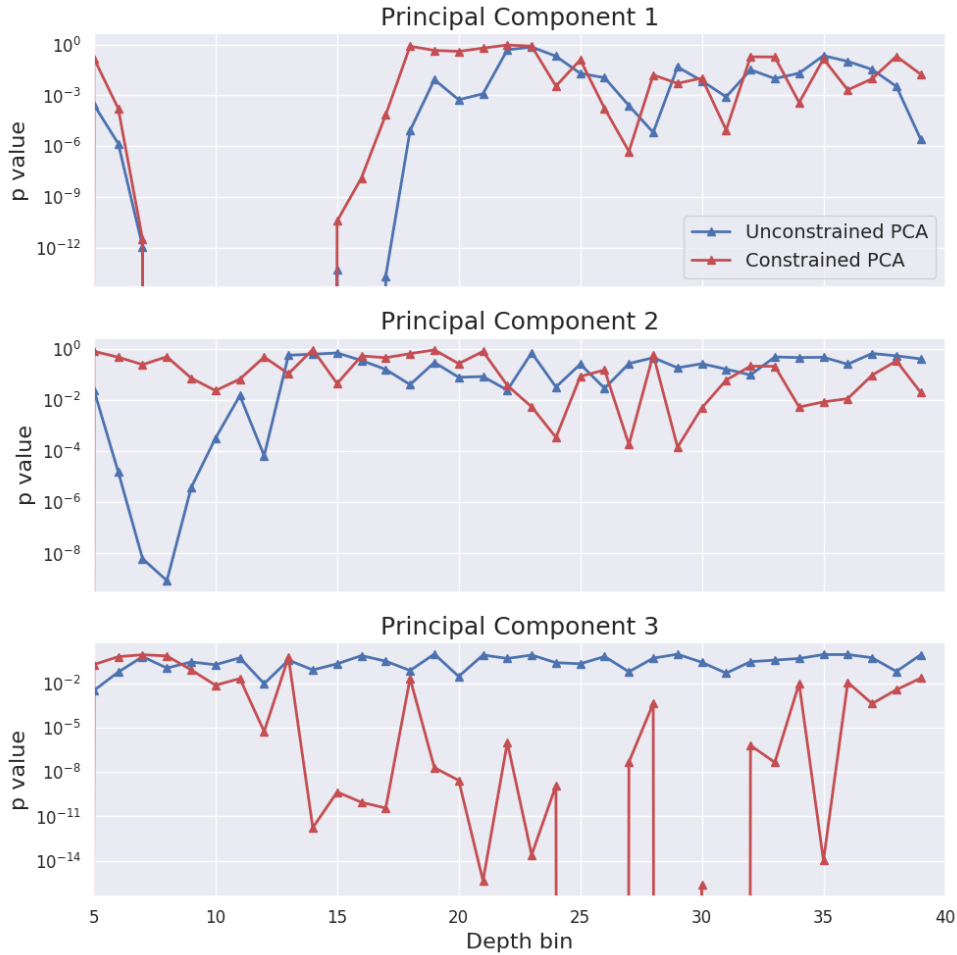


Figure 4.19: Comparison of the  $p$  values obtained from regressions based on the unconstrained and constrained principal components as a function of the depth bin containing the corresponding events.

For matters of model selection, the principle of Occam’s razor provides valuable insight. It is a rule of thumb that is more explicitly quantified by metrics such as Akaike Information Criterion [79], or the Bayesian analog, the Schwarz criterion [80]. In qualitative terms, it dictates that one should select a simpler model if there is not sufficient evidence to support a more complex model.

In this context, the constrained variety requires a free parameter for the threshold that determines which dimensions are included in the analysis. As Bair et al. reported, performance is sensitive to this parameter. The free parameter contributes to model complexity, and it leaves the reconstruction method based on this model

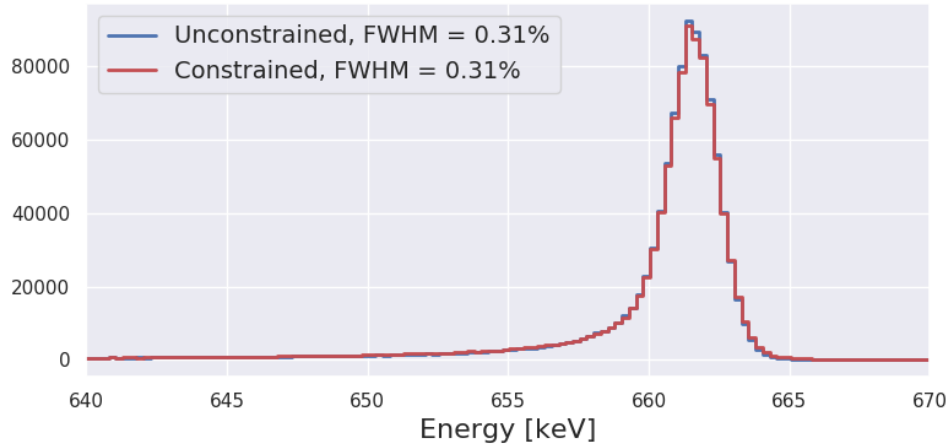


Figure 4.20: Aggregate, single-pixel energy spectrum obtained using unconstrained and constrained PCA.

susceptible to data-snooping - the process by which a model is repeatedly modified to produce optimal results. Based on the findings in this section, there is not sufficient reason to favor Bair’s methodology over unconstrained PCA.

Barshan et al. presented a variant of SPCA that does not entail free parameters [81]. The objective remains the same in that of Bair et al., but it identifies dimensions with significant dependence on the response variable by different means, namely the Hilbert Schmidt independence criterion (HSIC). The HSIC measures the dependence of two random variables - i.e., a response variable and the value in a dimension - from the norm of the cross-covariance operator in their respective reproducing kernel Hilbert space (RKHS) [82].

In the case that two such random variables are independent, the norm of the cross-covariance tends to a value of zero. Therefore, one must maximize the HSIC between the response variable and a given dimension of data. For the purposes of this work, the dependence between the response variable and the data projected onto a subspace is maximized to produce the most meaningful principal component regressions.

The ingenuity of Bair’s method lies in the maximization scheme and its connection

to unconstrained PCA. Let the variables  $\mathbf{X}$  and  $\mathbf{Y}$  represent the waveform matrix and the outer product of the response variable, respectively. The column space of matrix  $\mathbf{V}$  contains the eigenvectors that map data  $\mathbf{X}$  to the principal subspace such that the principal components are given by  $\mathbf{X}^T\mathbf{V}$ . Equation 4.5 models the empirical estimate of the HSIC, which measures the dependence between principal components and the response variable.

$$\hat{\mathbf{H}} = \text{Tr}(\mathbf{V}^T\mathbf{X}\mathbf{Y}^T\mathbf{Y}\mathbf{X}^T\mathbf{V}) \quad (4.5)$$

To maximize this measure of dependence, the eigenvectors must be modified accordingly. The solution for  $\mathbf{V}$  that maximizes the HSIC corresponds to the eigenvectors of the matrix  $\mathbf{X}\mathbf{Y}^T\mathbf{Y}\mathbf{X}^T$ . These eigenvectors serve the same purpose as those in the unconstrained variant of PCA.

For the sake of argument, suppose that there is no *a priori* knowledge of the response variable. Under these circumstances, the standardized response variable kernel  $\mathbf{Y}^T\mathbf{Y}$  reduces to the identity matrix. Using the same rationale, the eigenvectors that produce the optimal solution to Equation 4.5 correspond to the eigenvectors of the matrix formed by  $\mathbf{X}\mathbf{X}^T$ , an alternate expression for the covariance of the waveform data. As shown in Section 3.1, the eigendecomposition is one approach to performing PCA. Based on this observation, unconstrained PCA, or equivalently SPCA with no *a priori* information, generalizes the supervised decomposition proposed by Barshan et al.

Unfortunately, the constrained PCA eigenvectors obtained by this method do not reveal more information than the unconstrained variety, as shown in Figure 4.21. All information is collapsed, as it were, into the eigenvector for the first principal component, and it therefore discards the information that could otherwise correlate with subpixel lateral position or abnormal collecting pixel signals. Instead, the eigenvectors for the second and third principal components - and all subsequent eigenvectors

for that matter - are random noise.

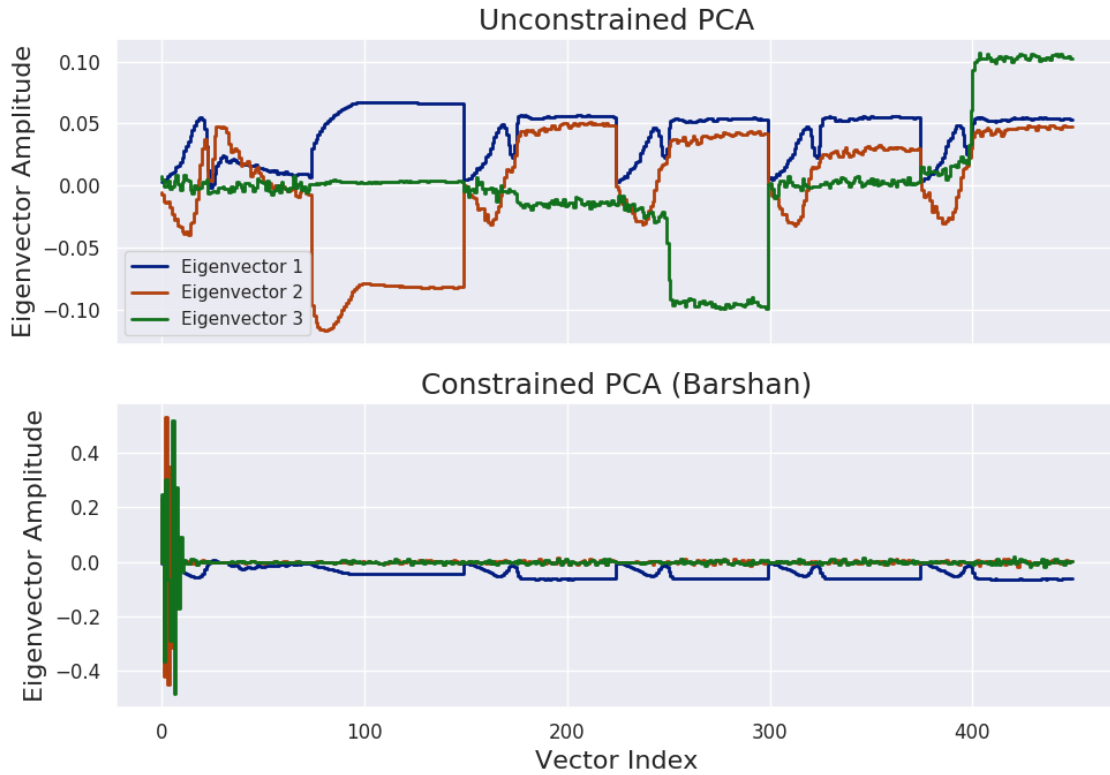


Figure 4.21: Eigenvectors for the first three principal components obtained by unconstrained PCA (top) and Barshan's method (bottom).

The spectrum obtained via Barshan's method provides no significant improvement over the results obtained by unconstrained PCA (Figure 4.22). It also lacks the ability to interpret the underlying mechanisms of the principal components. Unconstrained PCA remains the default implementation for principal component regression, due to this deficiency of Barshan's method.

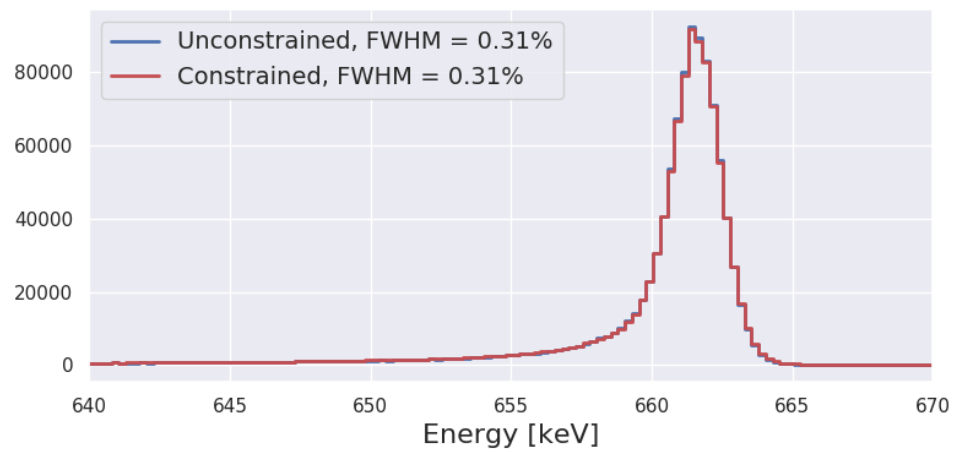


Figure 4.22: Single-pixel energy spectra for unconstrained PCA and principal component regression via Barshan's method.

## CHAPTER V

# Adaptations for Principal Component Regression for Multiple-Pixel Events

The contents of this chapter address the application of the PCA reconstruction methodology towards the unique challenges of estimating energy deposited in multiple-pixel events. The reconstruction process must account for the effects of WPCT, which is conventionally corrected after estimating the energy deposited by individual interactions. The SRF reconstruction methodology operates under the assumption that interaction properties can be estimated by matching an observed waveform to idealized templates derived from single-pixel observations. While this template-matching scheme can partially mitigate the influence of WPCT, this method still requires corrections to the cumulative, estimated energy deposition as discussed in Section 2.4.3.

This approach does not necessarily translate to the PCA methodology; the eigenvectors produced by the decomposition of single-pixel observations may not accurately reflect the specific characteristics of interactions that constitute multiple-pixel events. Most notably, the principal components determined from single-pixel event decomposition fail to account for the distortion caused by WPCT. Therefore, the methods presented in Chapter IV must be adapted to uniquely characterize multiple-pixel events. Subsequent sections thoroughly describe these adaptations for two-pixel

events and provide analysis of the resulting energy resolution. These methods are generalized for higher-order events at the conclusion of this chapter.

## 5.1 Adaptations for Multiple-Pixel Events

To effectively capture the relevant properties of a two-pixel event, the observations must include signals induced on both collecting pixels. The signals that correspond to the second collecting pixel are appended to the observations from the first pixel (Figure 5.1). This format ensures that all pertinent signals are captured by a signal observation.

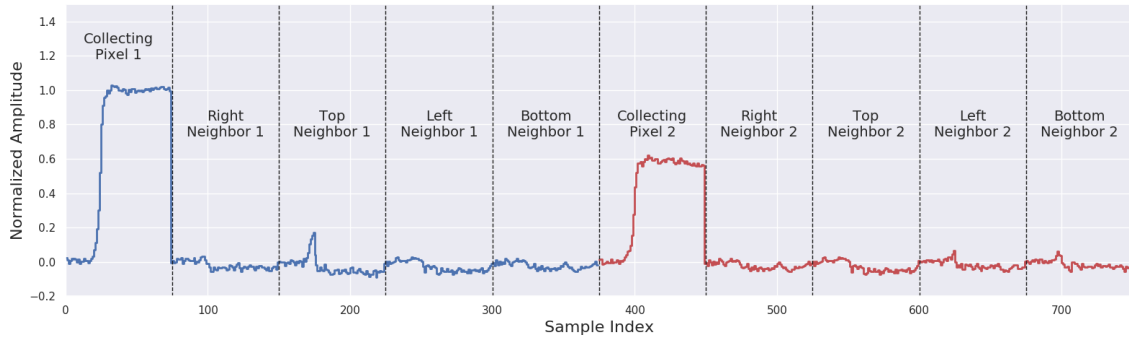


Figure 5.1: Sample, two-pixel observation annotated with the corresponding pixel descriptions.

Note that the collecting pixel with the greater signal amplitude is arranged first in the observation featured in Figure 5.1. As a matter of convention, this collecting pixel signal - referred to as the primary pixel - precedes the collecting pixel with lower amplitude - the secondary pixel. The observations of a given primary pixel constitute the rows of a pixel-specific data matrix. The decompositions of these separate matrices ensure that the eigenvectors provide some information about pixel-specific tendencies to account for idiosyncratic, systematic errors in the reconstructed energy deposition.

For more thorough analyses, events could be arranged in matrices devoted to

unique combinations of primary and secondary pixels. Although, this requires  $121 \times 120$  separate matrices and strains the limits of feasible calibration measurement statistics and computational resources required for the analysis. Limiting the number of waveform matrices to one per primary pixel relaxes these constraints and promotes more pragmatic use of the analysis.

The format of the waveform observations can accentuate key aspects of a two-pixel observation that provide critical information about a given event. It requires system-specific knowledge of the underlying physical processes to effectively emphasize these properties. In machine learning disciplines, this may be more formally referred to as ‘feature engineering’ [83]. By this process, one can suggest that the principal component regression embeds information about known sources of systematic error.

The preprocessing steps required for multiple-pixel event analysis share many tasks in common with those required for single-pixel events. As with single-pixel events, an event-specific time offset is applied to properly align columns with similar features in a data matrix. For the purposes of two-pixel events, all subsequent signals - collecting pixel and adjacent pixel signals alike - are aligned with respect to the time offset of the primary collecting pixel signal. This is preferred over the alternative, in which a time offset is determined for both collecting pixel signals in an observation. Figure 5.2 contrasts the observations formed by these approaches for a two-pixel event. The primary pixel signal remains unchanged between the two approaches, but the signal of the secondary pixel may shift significantly in time. The magnitude of this shift depends on the difference in trigger times between the collecting pixel signals.

The preference for a single, consistent offset reflects an intentional choice to preserve information regarding the difference in depth between the collecting anode pixel signals. Recall that the offset corresponds to the time at which the primary pixel signal exceeds half of its maximum amplitude, which serves as a reliable proxy for the electron drift time and depth of interaction. The index at which the secondary pixel

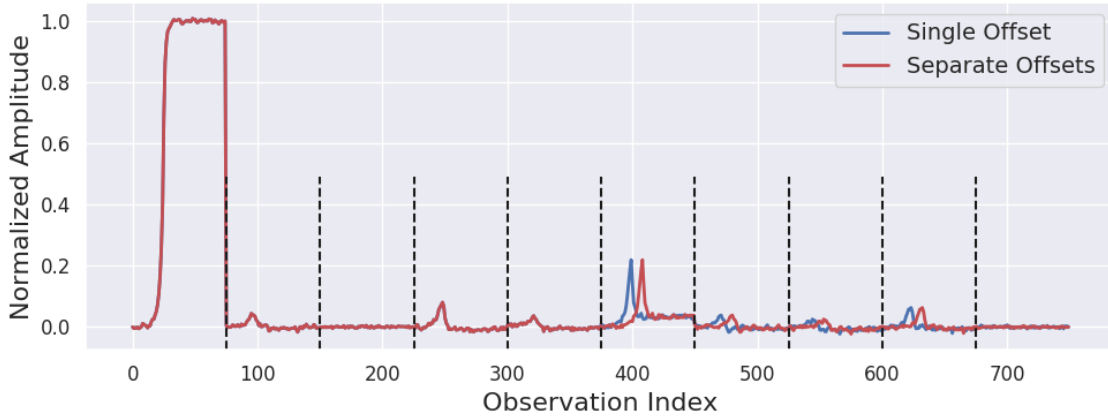


Figure 5.2: Sample, two-pixel observation configured with a single time offset determined by the primary pixel signal (blue) and separate time offsets determined for each collecting pixel signal separately (red).

signal rising edge starts varies according to the difference in depth. In the event that this form of explained variance is quantified by a principal component, the regression with respect to this component can compensate for any systematic error imposed by the resulting WPCT.

The correlations depicted in Figure 5.3 justify this choice. The second principal component correlates significantly with the reconstructed depth difference, and the two panes in Figure 5.3 plot the depth difference as a function of this principal component. The top pane features second principal components computed when a single, consistent time offset is applied to all waveform signals in an observation, whereas the bottom pane applies a time offset specific to each collecting pixel signal. The former preserves the relative trigger time difference between the collecting pixel signals, and higher correlation is expected between the observed depth difference and principal components. The strength of these correlations, as quantified by the Spearman rank correlation, confirm that a single offset produces the intended effect more definitively.

As demonstrated in Chapter II, the energy ratio also influences the magnitude

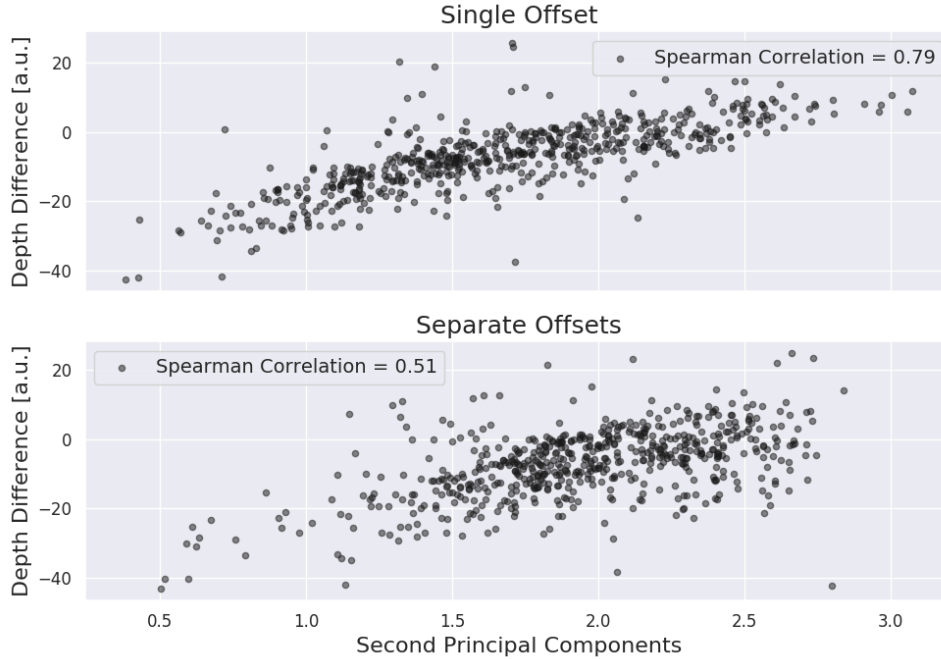


Figure 5.3: Difference in reconstructed depth for interactions in non-neighboring, two-pixel events as a function of the second principal component when using a single offset computed from the primary pixel signal (top) and using two, pixel-specific offsets (bottom).

of WPCT. Given its influence on WPCT, it would be advantageous to account for changes in energy ratio within the principal component regression framework. To accentuate the effect of energy ratio, two-pixel data vectors are normalized to the primary pixel signal amplitude. Under this approach, the amplitude of the secondary pixel signal tail ranges between zero and one. The correlation between energy ratio and the second principal component for a select anode pixel (Figure 5.4) provides evidence that the normalization scheme effectively captures this aspect of two-pixel events. This relationship obtains a functionally perfect Spearman correlation, implying that the effects of energy ratio are embedded within the decomposed data. If the signals for the primary and secondary pixels were normalized to their respective collecting pixel signal amplitudes, this relationship would provide insufficient correlation with any prominent principal component. Therefore, all signals are normalized by the primary pixel signal amplitude to maintain this correlation.

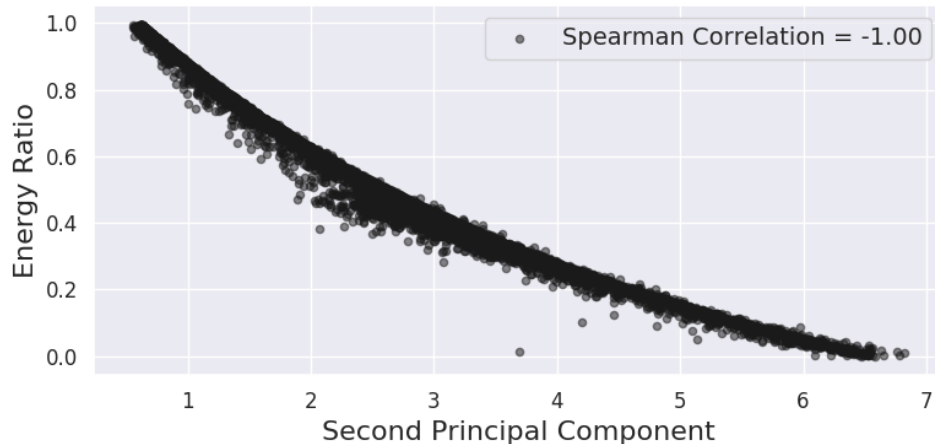


Figure 5.4: Energy ratio as a function of the second principal component for side-neighbor events for a given primary pixel.

The preprocessing steps necessary for multiple-pixel events differ from those used for single-pixel events at a critical juncture. The observations of multiple-pixel events omit the cathode signal, and the rationale behind this choice requires some foresight on the effect for higher-order events. This decision is elaborated in Section 5.5.

## 5.2 Categorization of Two-Pixel Events

Principal regression for two-pixel events requires a more nuanced approach than that of single-pixel events. To perform principal regression on reconstructed energy, events must be strategically divided to fully leverage the predictive capabilities of the regression. Consider the plot of combined, reconstructed energy for two-pixel events as a function of the first principal component in Figure 5.5. Based on the plotted data, no discernible trend is apparent in the first principal component.

These data represent a wide variety of events with significantly different properties. The data partially consist of neighboring events - events in which adjacent pixels trigger - which are frequently caused by the charge carriers originating from a single interaction [84, 85]. The remaining balance of events are attributed to non-

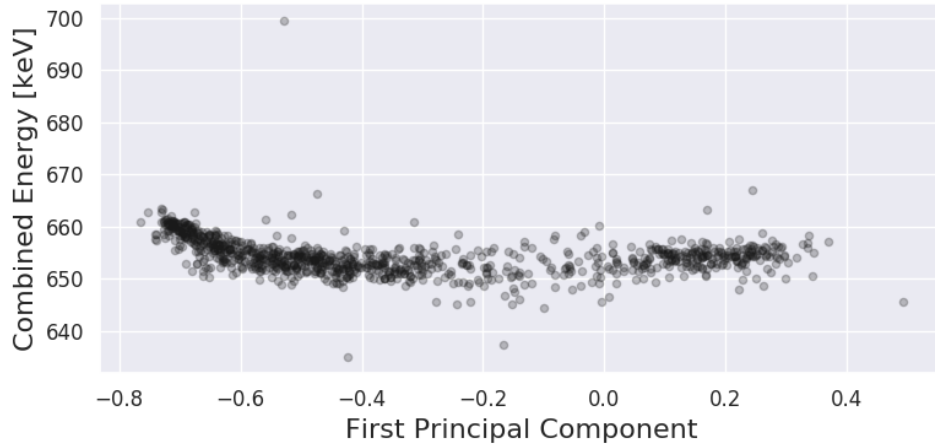


Figure 5.5: Combined, reconstructed energy of two-pixel events as a function of the first principal component for a given primary pixel.

neighboring events - events in which distinct gamma-ray interactions deposit energy in nonadjacent pixels. Such events may have different dependencies on the first principal component, as demonstrated in Figure 5.6. Although trends slowly come into focus after separating the neighboring and non-neighboring events, they cannot be fully exploited to correct the systematic error in the combined, reconstructed energy.

Additional, strategic event categorization promotes more effective regression with respect to principal components. A number of readily quantified event attributes divide the events into categories in which the systematic trends become more apparent. At this point of the reconstruction methodology, this resembles the conventional WPCT corrections from Section 2.4.3 where events are categorized by different factors (e.g., lateral separation, depth separation). However, principal component regression enables the two-pixel event energy to be modeled and corrected beyond common attributes while avoiding the deficiencies of these conventional calibration methods.

Of the event attributes that can distinguish two-pixel events, data is nearly uniformly distributed in only a few of these properties. Given the finite amount of calibration data, uniformity is a necessary condition to form regression models with a high degree of statistical significance for all events. Consider the distributions of

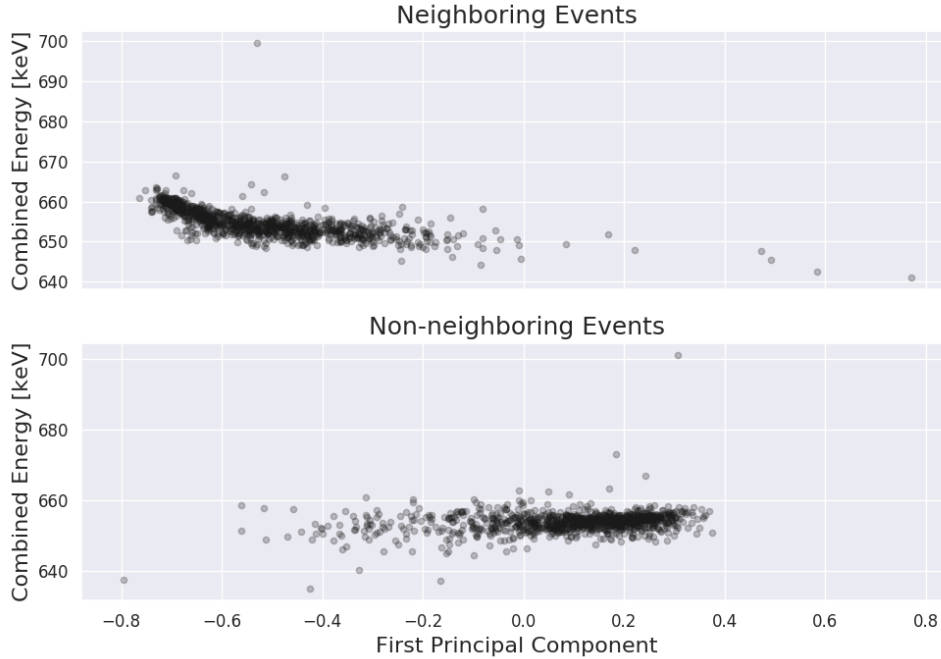


Figure 5.6: Combined energy for events of a given primary pixel as a function of the first principal component for neighboring events (top) and non-neighboring events (bottom).

event properties in Figure 5.7. Some categories are sparsely populated with events in certain regimes. For example, relatively few non-neighboring events have an energy ratio greater than 0.5, whereas the density below this threshold is far greater. Regression coefficients derived from sparsely-populated regions of data render the regression model susceptible to statistical uncertainty. One might assume that poor regressions for rare events does not significantly impact energy resolution. However, this line of reasoning may lead to overfitting calibration data; rarely observed events at 662 keV may become increasingly more common for gamma rays of different incident energies.

The required data density for statistically significant regressions leave two options for neighboring and non-neighboring events. Energy ratio and primary depth are viable options for neighboring events, whereas non-neighboring events contain relatively uniform distributions in primary depth of interaction and lateral separation. To limit model complexity, only one category is chosen for each. In either case, it is preferable

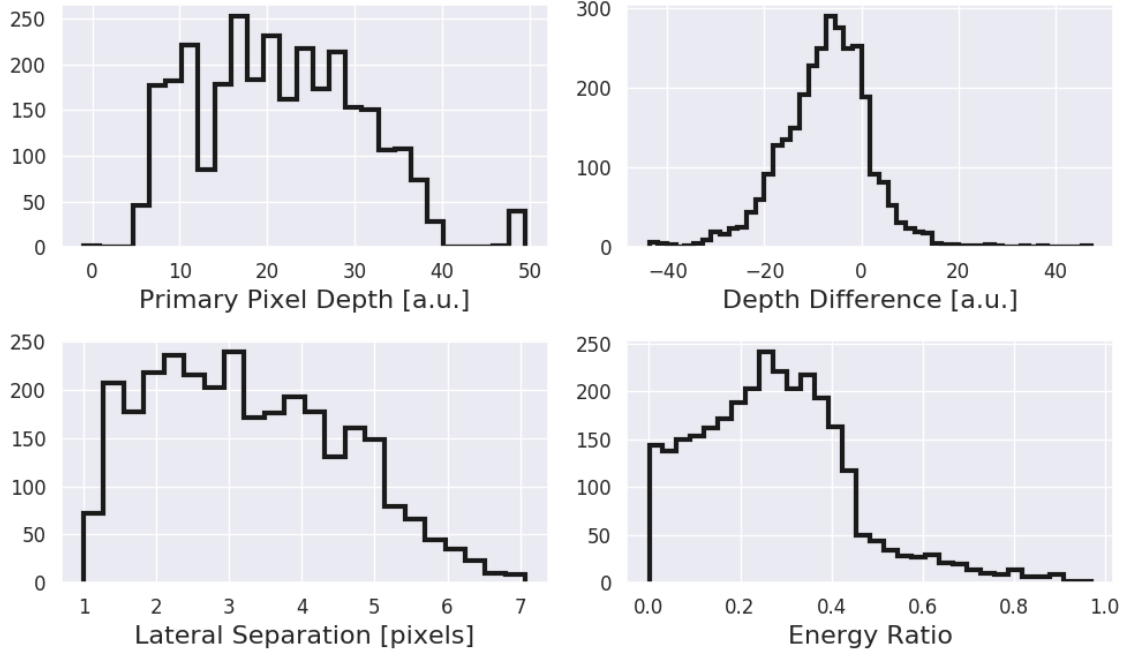


Figure 5.7: Distributions of the primary pixel depth of interaction (top-left), depth difference (top-right), lateral separation (bottom-left) and energy ratio (bottom-right) for non-neighboring, two-pixel events recorded for a single primary pixel.

that the categorization provides stronger dependence between energy and principal components. The Spearman rank serves as a valuable metric for this dependence.

The Spearman rank correlation values in Figure 5.8 correspond to the correlation between reconstructed energy and principal components for a set of non-neighboring events divided by the specified categories. The first and second principal component correlations for non-neighboring events categorized by lateral separation appear more consistent, and occasionally have higher magnitude, than those divided by primary pixel depth. It also confirms intuition about the nature of WPCT and its effect on multiple-pixel events. Charge carriers induce relatively small amounts of charge on pixels separated by a large lateral distance, and these events are less susceptible to the systematic error attributed to WPCT. Figure 5.9 depicts principal component regressions for non-neighboring events from three regimes of lateral separation.

While no appreciable trends emerged in the principal component regression of all non-neighboring events in Figure 5.6, the category-specific principal component regressions reveal more information about the systematic error in reconstructed energy.

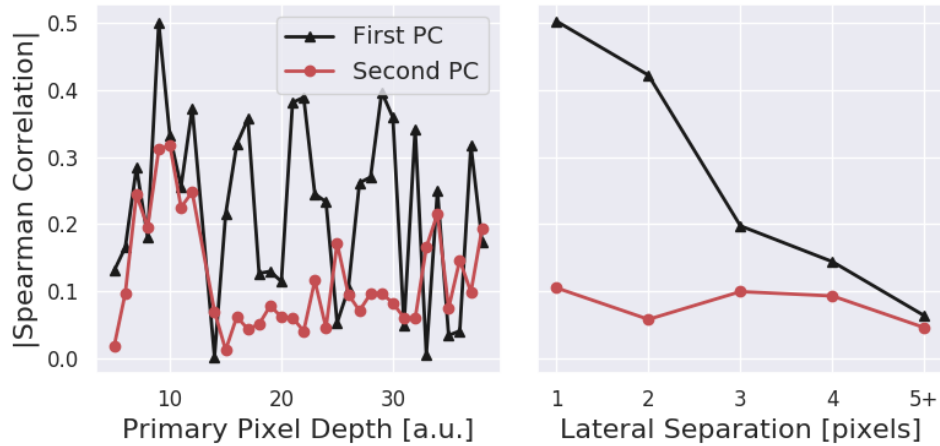


Figure 5.8: Spearman rank correlations for principal component regressions of non-neighboring events divided by the primary pixel depth (left) and lateral separation (right).

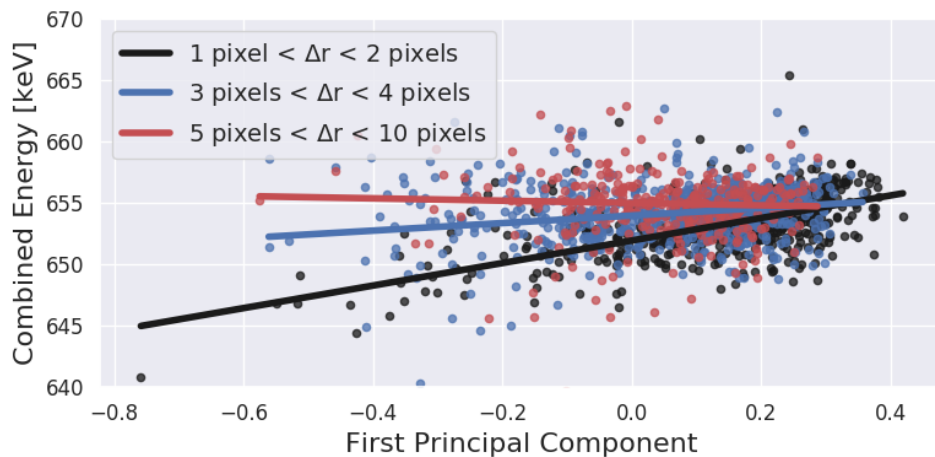


Figure 5.9: Principal component regressions for three regimes of lateral separation of non-neighboring, two-pixel events for a primary pixel.

The same analysis applies for neighboring events in Figure 5.10, in which absolute Spearman rank correlation measures the quality of the principal regressions between reconstructed energy and the first two principal components for the noted event cate-

gories. When categorized by depth of interaction in the primary pixel (left pane), regressions yield relatively high Spearman correlation for the first principal component. However, there is relatively weak dependence with the second principal component. Although the Spearman correlation with respect to the first principal component has less magnitude when categorized by energy ratio (right pane), it maintains an advantage in the correlation strength with respect to the second principal component. This, along with empirical results, justify the use of energy ratio to adequately categorize neighboring, two-pixel events. The quality of these regressions for the combined energy of neighboring events as a function of the first principal component is visualized more explicitly in Figure 5.11. As indicated by the trends for three regimes of energy ratio, the regressions of combined energy yield recognizable trends when separated by energy ratio.

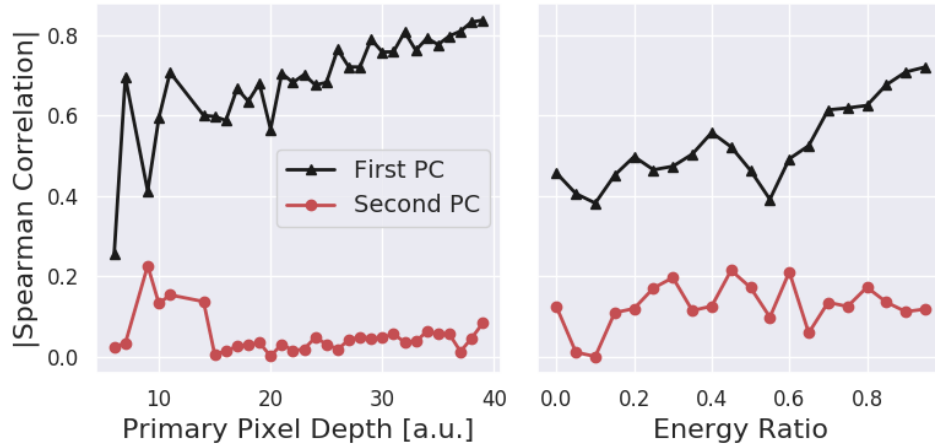


Figure 5.10: Spearman rank correlations for principal component regressions of neighboring events divided by the primary pixel depth (left) and energy ratio (right).

While two-pixel categorization enables principal component regression to more readily identify systematic trends in energy deposition, it leaves the principal component regression model more susceptible to free parameters and data-snooping. The binning parameters for event categories of non-neighboring and neighboring two-pixel

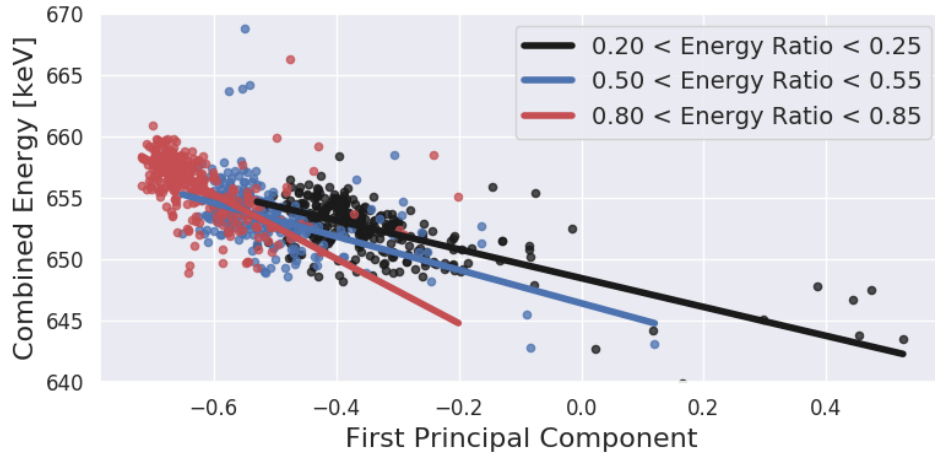


Figure 5.11: Principal component regressions for three regimes of energy ratio of neighboring two-pixel events for a primary pixel.

events - lateral separation and energy ratio, respectively - are free parameters. In the event that these categories are binned finely, the regression model may overfit the energy deposition trends according to the small amount of data within each bin. Alternatively, a coarse binning structure may degrade the regression accuracy. With this consideration in mind, the binning parameters are chosen so that the number of events in each category generate robust results. However, no rigorous optimization of the binning parameters were performed.

### 5.3 Results for Two-Pixel Events

Once events are categorized according to event type and category, principal component regression follows similar procedures as those outlined for single-pixel events. For each principal component, a linear model approximates the dependence of the combined energy as function of principal components, and combined energy is iteratively updated upon each principal component correction. As depicted in Figure 5.12, the spectral FWHM of all two-pixel events monotonically decreases as a function of the number of principal components applied.

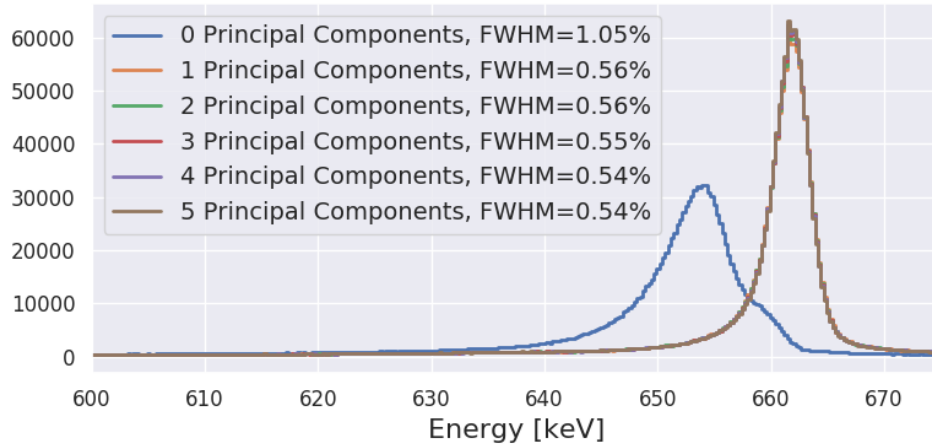


Figure 5.12: Processed, two-pixel energy spectra as a function of the number of applied principal component corrections.

The spectrum obtained without principal component corrections corresponds to the estimated energy after applying the standard depth corrections to the estimated energy deposition for each interaction. There is demonstrable systematic error in this initial spectrum; the observed centroid is significantly lower than the 662 keV energy of the incident photons, primarily due to the adverse effects of WPCT. The most significant improvement in energy resolution occurs after the application of the first principal component correction, in which the energy resolution improves by a factor greater than two. Beyond the first principal component, the energy resolution improves in small increments.

The PCA methodology compares favorably against conventional techniques for two-pixel events, as indicated by the energy spectra of a  $^{137}\text{Cs}$  exposure measurement in Figure 5.13. Relative to trapezoidal filtering and SRF, the observed FWHM at 662 keV for the PCA methodology improves by 7 and 14%, respectively in relative terms. The PCA methodology owes much of its success to the performance of side-neighboring events, which constitutes approximately 75 and 60% of all two-pixel events and two-pixel photopeak events, respectively.

The energy resolution of side-neighboring, two-pixel events is visualized as a func-

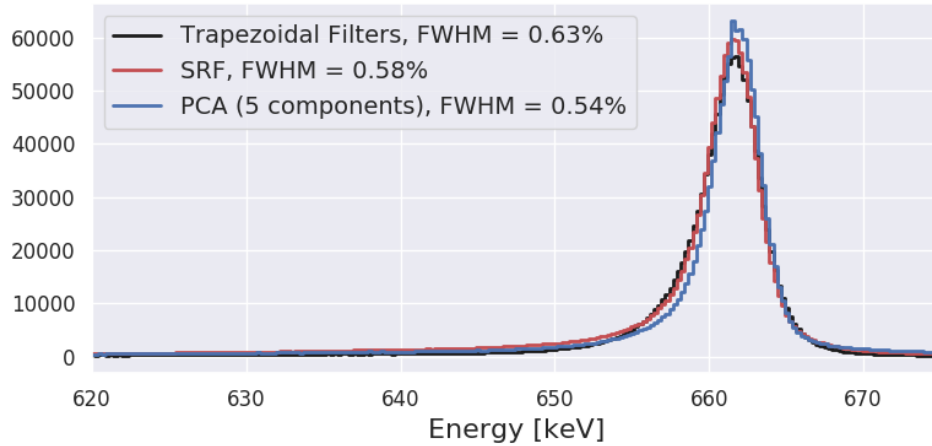


Figure 5.13: Two-pixel energy spectra of a  $^{137}\text{Cs}$  exposure processed by trapezoidal filtering, SRF and PCA reconstructions techniques.

tion of the primary pixel location in Figure 5.14, which compares the FWHM between SRF in the left pane to that of principal component regression in the right pane. The data in Figure 5.15 provides a direct comparison of the side-neighboring, two-pixel energy resolution for each primary pixel. It includes the line  $y = x$  as a benchmark; data that fall below the benchmark indicate net improvement between PCA reconstruction and SRF. Regardless of the baseline performance achieved by SRF, the energy resolution improves for the majority of anode pixels.

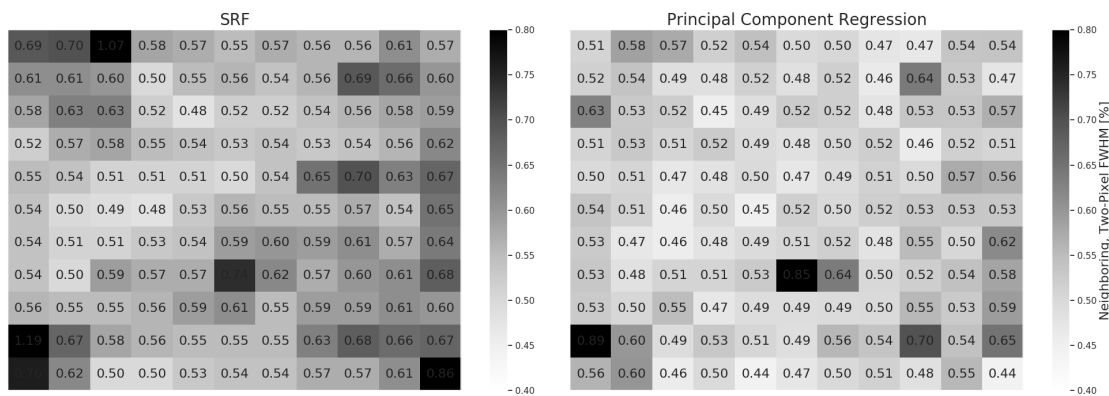


Figure 5.14: Neighboring, two-pixel event energy resolution for each primary pixel as a function of its physical location for SRF (left) and PCA (right).

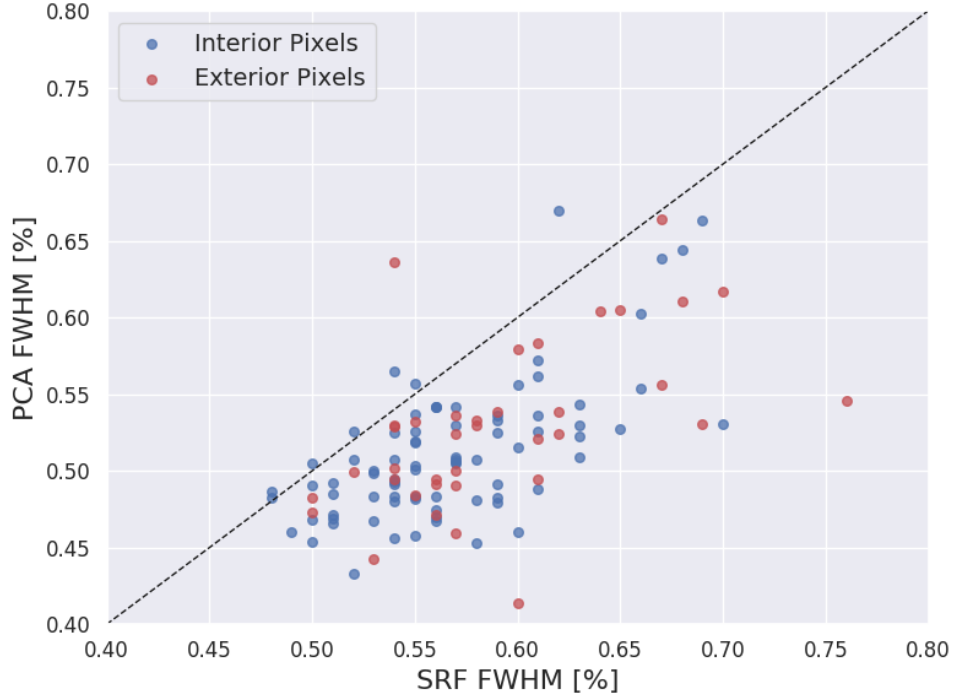


Figure 5.15: Neighboring, two-pixel event energy resolution for each primary pixel for PCA as a function of the resolution obtained by SRF.

The PCA methodology decomposes two-pixel observations separately for each primary pixel in an attempt to preserve information regarding pixel-specific tendencies and local material properties. Conventional methods do not preserve these effects, but rather derive two-pixel energy corrections from aggregate two-pixel event data from all pixels. Such an approach ignores differences in the position-specific response.

It is a nontrivial matter to determine how much of the improvement may be attributed to principal component regression or the pixel-specific decomposition, as there may be some indeterminable amount of codependency between these two factors. However, the contribution of pixel-specific PCA may be inferred by evaluating the performance under a framework in which all two-pixel events are analyzed in a single data matrix. This hypothetical application of PCA ignores position-sensitive response information and treats all events as though they are collected by a generic anode pixel.

Under this hypothetical framework, the energy resolution observed for all two-pixel events degrades to 0.59%, nearly matching that of the SRF methodology. The loss of pixel-specific eigenvectors negatively affects exterior pixels more severely, as the neighboring event FWHM recorded in exterior pixels degrades by 0.06% on average, doubling the average interior pixel degradation of 0.03%. While principal component regression alone helps the PCA methodology nearly match the performance achieved by SRF, the pixel-specific decomposition of waveform data gives PCA the comparative advantage. Pixel-specific corrections are not feasible for SRF or trapezoidal filtering largely due to the curse of dimensionality. In its current configuration, the WPCT correction divides two-pixel events by lateral and depth separation. Dividing these events further would degrade the statistical significance of the WPCT correction.

## 5.4 Processing Time

The rapid processing speed for the PCA methodology for single-pixel events benefits from the  $O(n)$  processes that govern event reconstruction processes. The circumstances change under the framework required for two-pixel event reconstruction. The processes pertaining to PCA evaluation and projection still rely on inner products among other  $O(n)$  processes, albeit with a larger value of  $n$ . The waveform vector nearly doubles upon the addition of the signals corresponding to the secondary pixel.

Although the length of  $n$  nearly doubles, the time allocated to the depth reconstruction accounts for the most significant increase in processing time under the multiple-pixel framework. The underlying assumptions of the CAR methodology no longer apply, and multiple-pixel event reconstruction relies on the trigger time to estimate depth of interaction. To extract robust estimates of the trigger time, waveforms must be filtered - a process that is optimally performed with a CR-RC<sup>*n*</sup> filter. The filtering process runs in  $O(n \log n)$  using the FFTW implementation, and it dictates the overall run time complexity for reconstruction under the PCA framework.

The trigger-time filter and the increase in waveform vector length change the relative processing time performance with respect to the standard trapezoidal filtering reconstruction. As with single-pixel events, trapezoidal filtering runs in  $O(n \log n)$  time for each observed waveform, and it implements the same depth reconstruction procedure as that of the PCA methodology. The comparison of processing time distributions for two-pixel events are shown in Figure 5.16. Due to the additional computational load for the PCA methodology, trapezoidal filtering obtains an advantage. However, the observed processing speed is still far faster than the maximum throughput of approximately 3000 events per second.

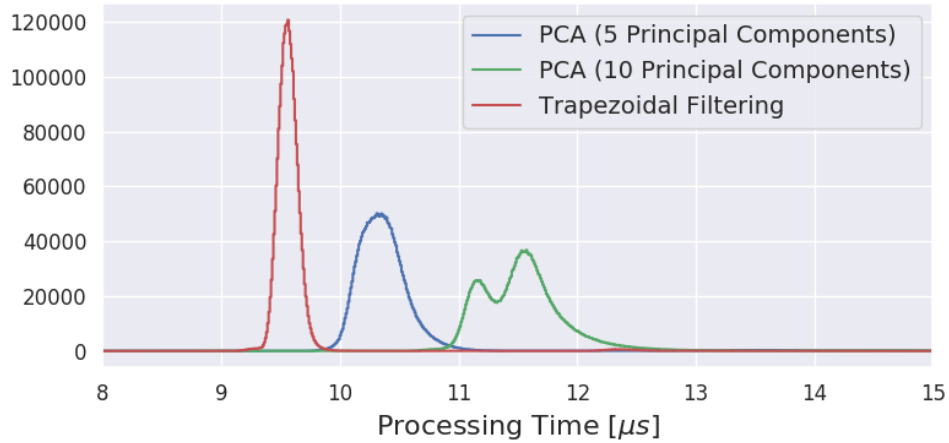


Figure 5.16: Processing time distribution for two-pixel events under various reconstruction methods.

## 5.5 Generalization for All Multiple-Pixel Events

The PCA framework must accommodate the reconstruction of higher-order events - events in which three or more pixels trigger - to provide a complete and effective alternative to conventional reconstruction methods. Such events are frequently associated with Compton scattering interactions, although they may result from charge sharing events or mixtures of the two. These events comprise a small, yet non-negligible, proportion of all detected events. In concrete terms, approximately 20% of events

in a typical,  $^{137}\text{Cs}$  exposure trigger three or more pixels. This fraction increases as a function of incident gamma-ray energy, due in part to changes in the gamma-ray interaction cross sections in CdZnTe and the electron cloud dimensions.

The logistics of decomposing higher orders of events in the same manner as single and two-pixel events render it impractical. The predominant concern is the amount of higher-order event data and the categorization thereof. Much of the success of principal component regression of two-pixel event data is predicated on event categorization. Event categorization strategies for two-pixel events correspond to fundamental parameters (i.e., lateral separation, energy ratio), but quantifying equivalent metrics for higher-order events becomes increasingly difficult as the number of triggered pixels increases. For example, the distribution of the energy deposited between two pixels is concisely quantified by the energy ratio, but more complex schemes are required to quantify the distribution of energy deposition for higher-order events with a single value. Even with the aid of an effective event categorization scheme, the relatively small amounts of higher-order events present challenges for the generation of statistically-significant corrections by means of principal component regression.

The more pragmatic approach to higher-order event reconstruction relies on the corrections derived from two-pixel events, owing to the abundance of two-pixel photopeak data and the salient information embedded in their eigenvectors. To properly apply principal component corrections derived from two-pixel events towards higher-order events, one must divide the constituent interactions into pairs. For an  $n$ -pixel event, there are  $\frac{n(n-1)}{2}$  unique combinations of interactions. Consider the case of a generic three-pixel event. In such an event, there are three unique pairs of interactions: the first and second, first and third, and the second and third pixels all form two-pixel events in isolation.

Under this framework, each pair is processed as though it is a two-pixel event. As modeled in Equation 5.1, the summation of the net change in energy for the pseudo-

events formed by pixels  $i$  and  $j$  produces the cumulative energy change for an  $n$ -pixel event. This concept serves as an analogue to the WPCT developed by Zhang [46], albeit with principal component corrections.

$$\Delta E_{\text{Total}} = \sum_{i,j>i}^n \Delta E_{i,j} \quad (5.1)$$

To rationalize Equation 5.1, it is convenient to recall the Shockley-Ramo theorem introduced in Chapter II. It dictates that the net charge induced on an electrode,  $\Delta Q$ , by several units of charge, individually represented by  $q_i$ , corresponds to Equation 5.2. The charge induced by  $q_i$  on an electrode is independent of any other  $q_j$  ( $j \neq i$ ). Therefore, the net induced charge is the superposition of the signal induced by all charges  $q_i$ . This ignores the effects of charge repulsion, which may alter the path of  $q_i$  to an insignificant extent. If only the charge carriers collected by pixels  $i$  and  $j$  are considered, one can therefore approximate the signals induced by the hypothetical two-pixel event formed by this pair. On a macroscopic scale, the energy collectively deposited by this pseudo-event may be estimated from the initial, depth-corrected energy for pixels  $i$  and  $j$ . This estimate may be updated with the aid of principal component corrections, and the change relative to initial energy is  $\Delta E_{i,j}$ .

$$\Delta Q = - \sum_i^N q_i [\phi_0(\mathbf{x}_{t_f}) - (\mathbf{x}_{t_0})] \quad (5.2)$$

Certain assumptions must be made to apply this approach for higher-order events, as the effects of WPCT cannot be completely decoupled from the sampled waveforms. Consider a combination of two interactions from a three-pixel event. The WPCT imposed by the third interaction is embedded in the waveforms of the pseudo-event, even though it is not considered in the pair. Due to this contribution, the projection of the pseudo-event onto the principal subspace is biased to some extent. Without a method

for isolating the induced signals from the interactions in question, this bias cannot be mitigated. Promising methods such as independent component analysis (ICA) allow one to separate mixtures of signals [86]. However, ICA relies on restrictive assumptions of independent signals that do not necessarily apply to the signals induced by multiple-pixel events in pixelated CdZnTe detectors.

Note that the cathode signal is omitted from the observations of multiple-pixel events. Compared to an anode pixel, the signal induced on the planar cathode surface is far more sensitive to the movement of all charge carriers. The amplitude of this signal corresponds to the summation of the contributions from all moving charge carriers, while the anodes are only sensitive to those that move in close proximity to the pixel in question. Therefore, the observed cathode signal in a higher-order event does not accurately reflect the cathode signal pertaining to the pseudo-event formed by a pair of interactions. The observed cathode signal consistently overestimates the latter and adds a source of systematic error to the calculation of principal component values for higher-order events.

To prevent exhaustive evaluation of the higher-order energy resolution, the comparison is limited to the performance for three and four-pixel events in Figure 5.17. It provides a direct comparison of trapezoidal filtering, SRF and PCA methodology applied to identical  $^{137}\text{Cs}$  exposure data. The PCA methodology compares favorably with respect to three-pixel event performance, but SRF achieves the best performance for four-pixel events by a significant margin.

The relative performance between trapezoidal filtering and PCA do not change for three and four-pixel energy reconstruction. However, the performance achieved by SRF surpasses the two alternatives only for four-pixel events. The reason for this shift in performance lies in the depth reconstruction mechanics for this suite of reconstruction methods.

The depth reconstruction and subsequent depth-correction process for trapezoidal

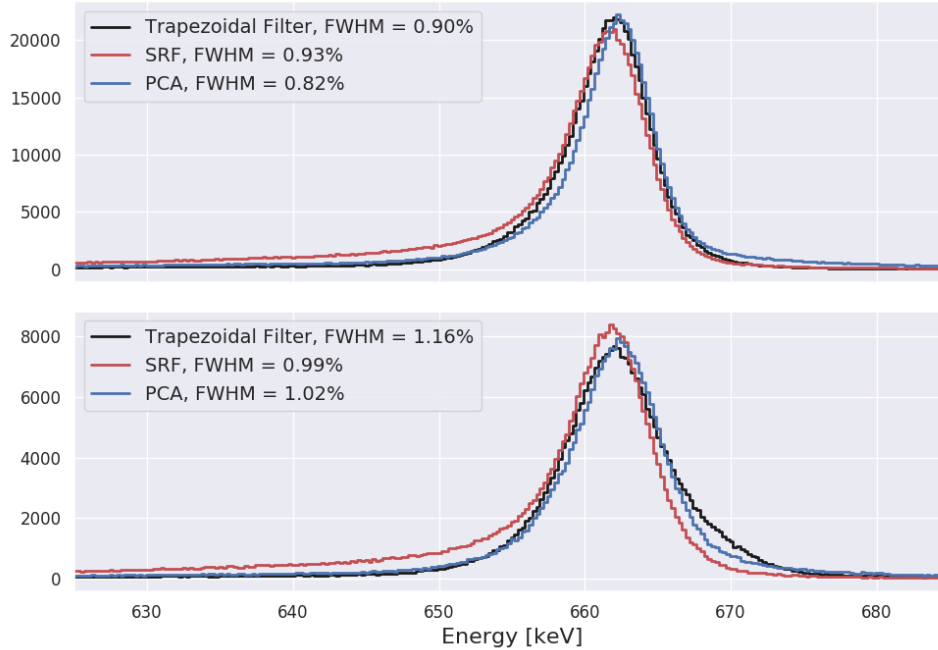


Figure 5.17: Comparison of three-pixel (top) and four-pixel (bottom) energy spectra for a  $^{137}\text{Cs}$  exposure processed via trapezoidal filtering, SRF and the PCA methodology.

filtering and the PCA methodology are fundamentally identical, as they both estimate depth of interaction based on trigger time. The SRF framework follows a different procedure in which it determines the best depth estimate by matching the observed waveforms to the system response templates that they most closely resemble. The two approaches yield insignificant differences in estimated depth for single-pixel events as demonstrated in Chapter II. However, this consistency is not true of multiple-pixel events.

The estimated trigger time, and therefore depth of interaction for trapezoidal filtering and PCA, for multiple-pixel events is much more sensitive to the effects of WPCT. The transient signals imposed on collecting pixels cause a systematically low estimate of the trigger time and depth of interaction. This is increasingly true for interactions with little induced charge, as the transient signal from WPCT may have larger magnitude.

Consider the waveforms of a generic two-pixel event in Figure 5.18, which features raw waveforms and the corresponding filtered waveforms used in the trigger time estimation process. The primary pixel signal imposes a considerable transient signal on the secondary pixel. This is readily apparent to the human eye, as the secondary pixel signal initially rises, declines as the WPCT induced charge in a neighboring pixel decreases, and rises once again as it collects charge. However, the filtered waveform fails to make this distinction and severely underestimates the trigger time of the secondary pixel signal. If the secondary pixel amplitude signal were greater, the transient signal would be less likely to exceed the trigger threshold.

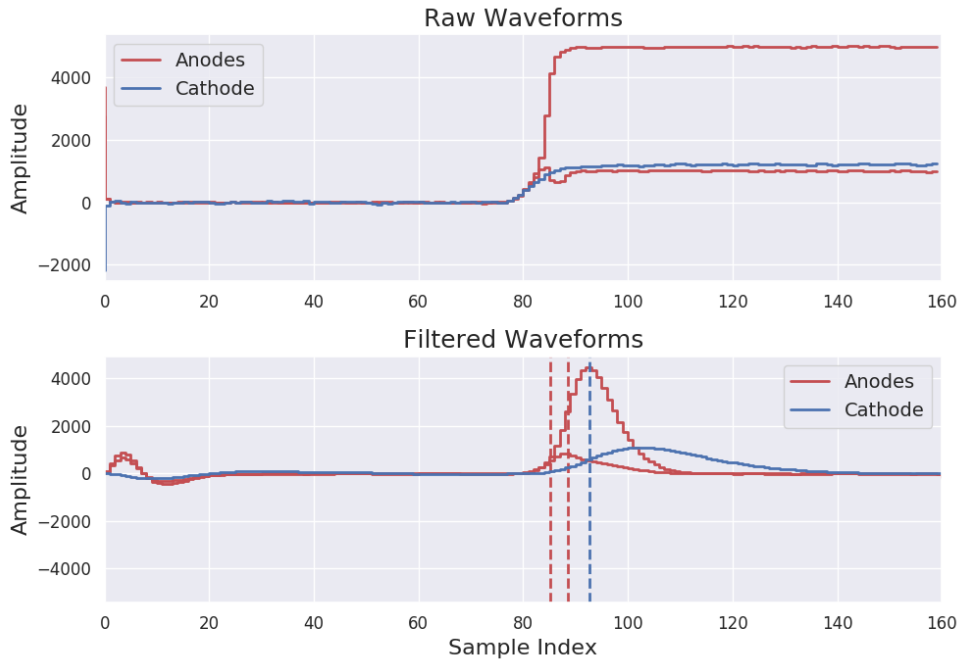


Figure 5.18: Raw waveforms acquired for a generic two-pixel event (top) and the corresponding, filtered waveforms used in calculating the trigger times (bottom). The trigger times are indicated by the dashed, vertical lines.

The resulting systematic error in depth may not be significant for cathode-side interactions, as the induced signal amplitude is approximately constant as a function of depth in this regime. However, systematic error can be more consequential for interactions near the anode where the response changes significantly as a function of

depth. As it pertains to energy reconstruction, the depth correction shared by PCA and trapezoidal filtering aggressively compensates for the assumed loss of amplitude for anode-side events and overestimates the energy deposition for the affected, collecting pixel. The energy deposition estimated by SRF is less sensitive to these sources of systematic error.

This consideration becomes relevant when analyzing higher-order events, as the total energy deposition is shared among more pixels. As indicated by the distribution of energy deposited in individual pixels for  $^{137}\text{Cs}$  photopeak events in Figure 5.19, the most probable energy deposition per pixel in three and four-pixel events are those with a low amount of energy. This distribution of energy deposition increases the potential for systematic error for higher-order events reconstructed by PCA and trapezoidal filtering.

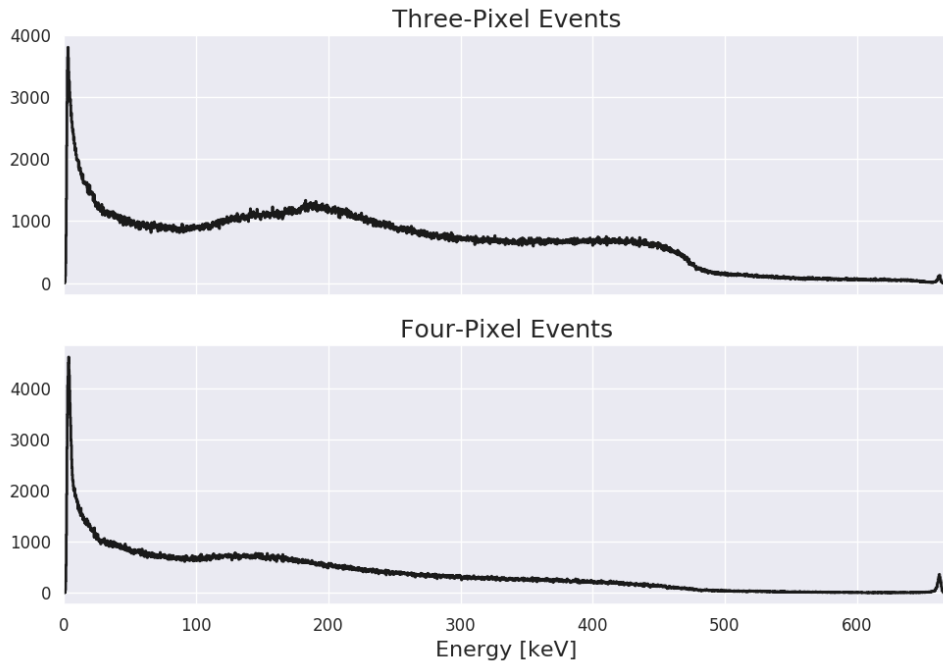


Figure 5.19: Distribution of energy deposited in individual pixels for  $^{137}\text{Cs}$  photopeak events resulting in three-pixel events (top) and four-pixel events (bottom).

Based on these arguments, the performance of PCA and trapezoidal filtering de-

depends much more heavily on the presence of low-energy interactions than SRF as shown in Figure 5.20. To modulate the influence of events containing interactions with small energy deposition, the energy resolution is calculated at several threshold values. The threshold value places a lower limit on the energy deposited in an individual pixel; events containing interactions that do not meet this threshold are excluded from the energy resolution calculation. By removing events with low-energy interactions, the sources of systematic error in trapezoidal filtering and PCA reconstruction should progressively diminish as threshold increases. This is apparent in Figure 5.20 where the four-pixel energy resolutions obtained with trapezoidal filtering and PCA reconstruction improve by 0.10 and 0.06%, respectively, as the threshold increases from 0 to 30 keV. The energy resolution achieved by SRF changes insignificantly in this range of thresholds and indicates that the reconstruction method is resilient to the presence of low-energy interactions. It is this resilience that allows SRF to surpass the resolution of alternatives for events in which low-energy depositions are prevalent.

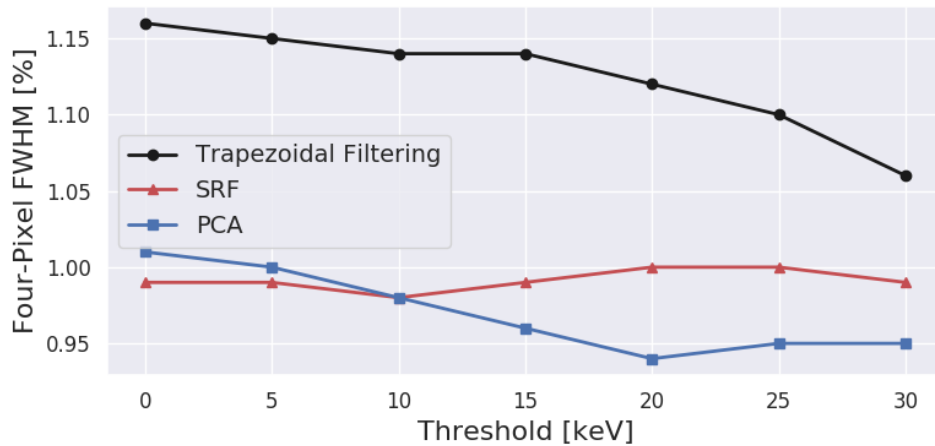


Figure 5.20: Observed, four-pixel energy resolution at 662 keV as a function of a low-energy threshold for trapezoidal filtering, SRF, and PCA reconstruction methods. Events that contain individual interactions with energy deposition below the threshold are removed and excluded from the energy resolution calculation.

## CHAPTER VI

# Adaptations for Principal Component Regression for High-Energy Events

Event reconstruction of high-energy depositions differs from the interactions analyzed in Chapters IV and V enough to justify a chapter devoted to its unique challenges. This subject matter is relevant to niche applications in which numerous, high-energy gamma-ray emissions must be resolved and quantified, such as neutron-capture prompt gamma-ray activation analysis (PGAA) [87–89]. Additional applications, such as imaging prompt gamma rays induced by the delivery of clinical proton beams [90, 91], bear some dependence on accurate energy reconstruction of high-energy, gamma-ray interactions.

For the purposes of this work, high-energy depositions are those in which more than 1 MeV is deposited. Beyond this energy, conventional reconstruction methods and principal component regression propagate sources of systematic error. The systematic error in question manifests itself in the form of misaligned photopeak centroids as shown in Table 6.1. Tabulated data for various  $^{228}\text{Th}$  and  $^{22}\text{Na}$  gamma-ray emissions<sup>1</sup> indicate that all viable reconstruction methods systematically underestimate photopeak centroids below the calibration energy of 661.7 keV and overestimate incident gamma-ray energy above the calibration point. The differential nonlinearity

---

<sup>1</sup>Gamma-ray emission energies were extracted from the Idaho National Laboratory (INL) gamma-ray spectrum catalog

is more explicitly featured in Figure 6.1. Bias appears at low-energy depositions to a small extent, but it is far more pronounced for incident gamma-rays possessing energy above the calibration point.

Table 6.1: Observed, single-pixel photopeak centroids as a function of incident gamma-ray energy as reconstructed by PCA, SRF and trapezoidal filtering

Emission Energy [keV]	PCA Centroid [keV]	SRF Centroid [keV]	Filtering Centroid [keV]
238.632	273.2	237.95	237.96
300.087	298.6	299.27	299.27
510.770	509.9	510.46	510.24
583.191	582.7	583.25	583.01
727.330	728.1	728.53	728.24
785.370	787.1	787.27	787.16
860.564	863.0	863.24	862.75
1274.53	1283.3	1283.40	1282.28
1592.521	1608.0	1607.50	1606.28
2614.533	2654.6	2654.00	2651.77

Mechanisms specific to high-energy gamma-ray interactions also degrade energy resolution above the calibration point. Of the factors that dictate energy resolution, the most prominent contributions arise from statistical error, electronic noise, variance in the charge-carrier transport, and systematic error. Electronic noise is a property determined by the sensor and front-end electronics subsystem design, and it remains constant over the entire energy domain. Statistical variation arises from fluctuations in the amount of charge carriers generated by the interaction between radiation and matter. The Fano factor succinctly describes the statistical properties of this fluctuation, and it measures the ratio between the observed signal amplitude variance to that predicted by Poisson statistics [92]. The Fano factor depends entirely

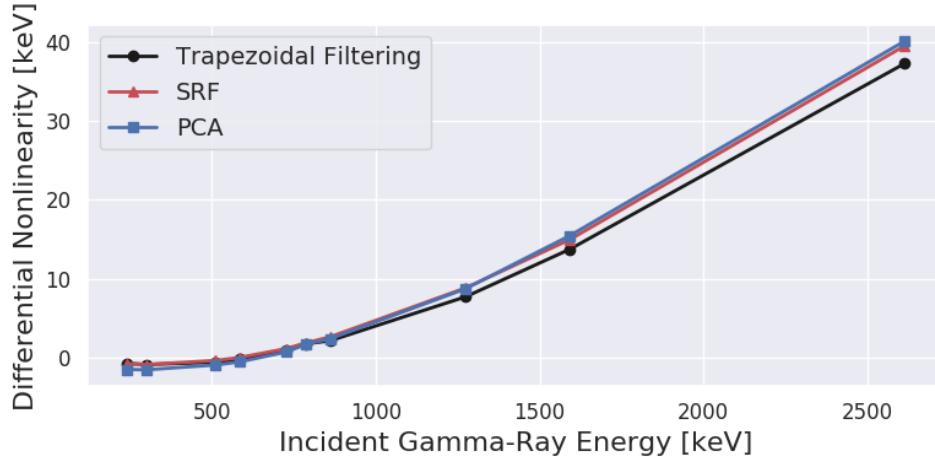


Figure 6.1: Differential nonlinearity for reconstructed, single-pixel photopeak centroids as a function of incident gamma-ray energy for various reconstruction methods.

on the detection medium, and its contribution to the observed FWHM is modeled by Equation 6.1, in which  $W$ ,  $F$ ,  $\epsilon$  and  $E$  represent the FWHM, Fano factor, the efficiency at which charge carriers are generated and the incident radiation energy, respectively. Note that the factor  $2.35^2$  relates the variance to FWHM under the assumption of a Poisson distribution.

$$W^2 = 2.35^2 F \epsilon E \quad (6.1)$$

Based on Equation 6.1, the statistical contribution of FWHM depends on the square root of the incident gamma-ray energy, and its relative contribution to the FWHM as a percentage of the energy deposition - which is the preferred form for reporting this metric - decreases as a function of incident energy. Variations in charge-carrier transport is not characterized as precisely as the contributions from electronic noise and statistical variation. It ultimately depends on electrode geometry and the detector material. Owens suggests that the FWHM attributed to variations in charge-carrier transport depends linearly on incident energy for a coaxial HPGe detector [93], but the implications for pixelated CdZnTe detectors have not been evaluated with

the same level of detail and rigor. The contribution of systematic error in the event reconstruction process also lacks thorough characterization as a function of incident gamma-ray energy.

Despite the uncertain contributions of charge-carrier transport variation and systematic error as a function of incident energy, the prevailing sentiment suggests that energy resolution in pixelated CdZnTe detectors should monotonically decrease as incident energy increases. The observed FWHM of single-pixel events under the PCA framework deviates from the expected behavior as demonstrated in Figure 6.2. Energy resolution at low incident energy degrades due to the fixed contribution from electronic noise, and it progressively improves until approximately 1500 keV.

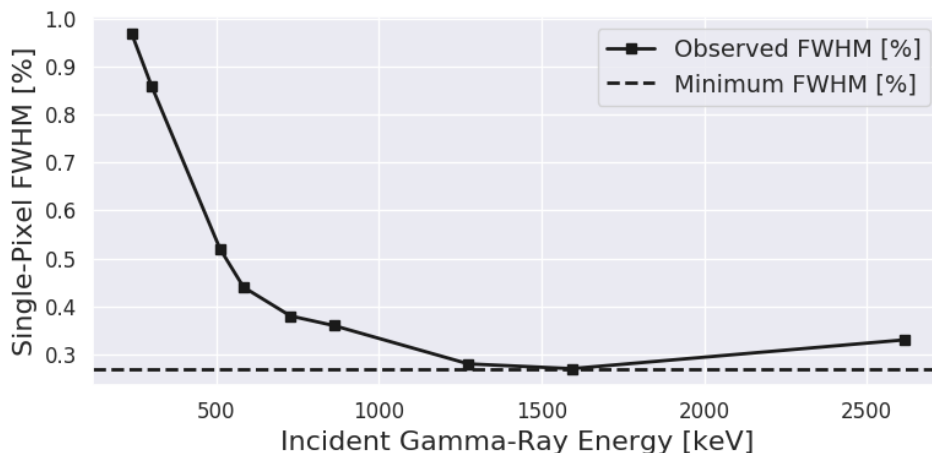


Figure 6.2: Single-pixel energy resolution as a function of incident gamma-ray energy obtained with PCA reconstruction.

Given current designs of detector geometry, electrode configuration and front-end electronics, the task of improving energy resolution for high-energy depositions focuses on compensating for the variance in charge-carrier transport more effectively. Statistical variance, electronic noise and charge-carrier transport variations are inherent properties to the detection system used in this work, and the focus of this chapter rests on mitigating sources of systematic error that prevail at higher gamma-ray energies. For conventional methods, this is performed by characterizing the differential

nonlinearity for each anode pixel. Such methods yield energy resolution that more accurately reflects the expected performance at high incident energy, but they neglect the position-specific responses for high-energy depositions. The intent of this work seeks to leverage the analysis provided by PCA to mitigate the underlying causes of poor performance in high-energy depositions.

Event properties that distinguish high-energy events from the events studied in previous chapters are elaborated in subsequent sections. The adaptations developed to address these challenges and the corresponding performance for these adaptations are presented for single-pixel and multiple-pixel events. The performance of the PCA methodology is compared directly to the leading alternative for energy resolution, SRF. The evaluation of the performance for these methods leads to discussion of the factors that limit performance of principal component regression.

## 6.1 Challenges Unique to High-Energy Events

As indicated by Zhang, Kaye & He, some portion of the systematic error arises from the front-end electronics [94]. In more concrete terms for the data acquisition systems used in this work, the manufacturers of the VAD\_UM2 ASIC, Integrated Detector Electronics AS (IDEAS), cite a 0.35% integral nonlinearity [95]. For a complete analysis of this effect, one must also consider the operating dynamic range. The VAD\_UM2 ASIC offers several dynamic ranges that allow users to tailor their data acquisition for specific applications. This includes a 700 keV dynamic range as well as the 3, 7 and 9 MeV dynamic ranges that are more appropriate for this subject matter. As feedback capacitors in the front-end electronics change to accommodate varying dynamic ranges, the extent to which integral nonlinearity affects the energy resolution at a fixed gamma-ray energy varies. The intent of this work is not to characterize nonlinearity effects for each of the applicable dynamic ranges, but rather to provide a framework that can compensate for the adverse effects of nonlinearity

independently of dynamic range.

Additional systematic error originates in assumptions for the event reconstruction model. The reconstruction methods established for low-energy depositions implicitly assume that the position of interaction resembles a point estimate. This approximation becomes increasingly inaccurate as the energy deposition increases, and the locations at which charge carriers are born frequently extend beyond the virtual voxel boundaries of position-sensitive CdZnTe detectors. Consider the simulated gamma-ray depositions in a CdZnTe detector volume for 500 and 3000 keV incident gamma rays in Figure 6.3<sup>2</sup>. The 500 keV deposition (left pane) is enclosed in a small volume where the extent in the largest dimension is approximately 0.15 mm, whereas the track of a 3000 keV deposition (right pane) consumes a far larger volume. The length of the largest dimension of the 3000 keV track is approximately ten times greater than that of the 500 keV deposition, despite only a factor of six between the energy depositions. Visualizing these two examples of charge clouds offers admittedly anecdotal evidence to the spatial extent of charge carriers, but it provides insight as to how increasing energy deposition affects the underlying assumptions of conventional reconstruction procedures.

In the event of a large energy deposition, charge carriers may originate across regions of disparate weighting potentials. If they terminate their paths at the same location, the resulting variance in their respective charge induction on the collecting pixel obfuscates the actual energy deposition. This phenomenon affects anode-side events more severely due to the higher weighting potential sensitivity to changes in position. Furthermore, some charge may not be collected by any pixel, but rather fall to the gap between anode pixels. In such an event, the recorded signal may have a significant amplitude deficit [63].

Low detection efficiency for high-energy gamma rays further complicates the study

---

<sup>2</sup>Interactions and radiation transport are simulated via the Geant4 simulation toolkit [96, 97] and the associated Livermore low-energy, electromagnetic models [98].

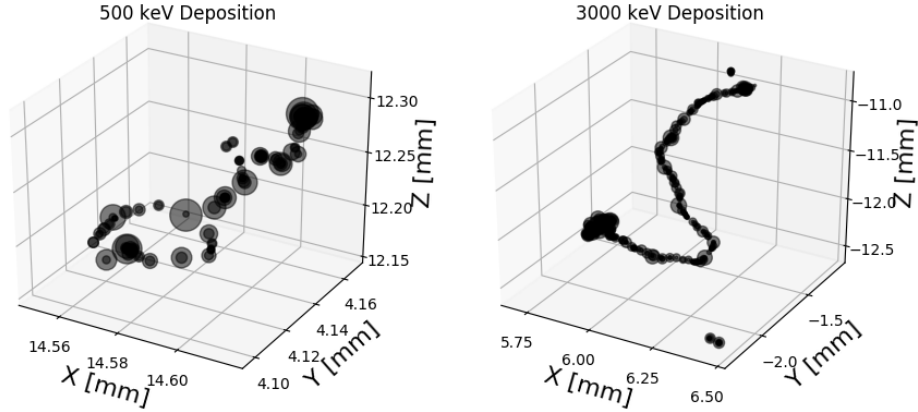


Figure 6.3: Simulated interactions in which 500 keV (left) and 3000 keV (right) are deposited in a CdZnTe detector. The location and size of the circles indicate the location and the relative magnitude of the energy deposition, respectively.

and correction of such events. Meaningful and statistically-significant insights may be derived from the acquisition of high-energy gamma-ray interactions, but they are exceedingly difficult to record with low-activity calibration sources. The methods presented in this text predominantly use a  $^{228}\text{Th}$  check source and its associated 2614 keV emission to acquire such data, but the acquisition includes a litany of low energy and relatively high-probability emissions that accompany it.

## 6.2 Principal Component Regression for Single-Pixel Events

Following the structure of previous chapters, the analysis of principal component regression for high-energy interactions begins with relatively uncomplicated single-pixel events before advancing to the challenges of multiple-pixel events. To achieve optimal single-pixel energy resolution, corrections must address the voxel-specific sources of systematic error as was demonstrated in Chapter IV, and they must also target mechanisms that afflict high-energy interactions in particular. As evidenced by the non-monotonic single-pixel energy resolution trend as a function of incident gamma-ray energy in Figure 6.2, only accounting for voxel-specific systematic error

via principal component corrections is insufficient.

Much like conventional reconstruction techniques, the PCA methodology is not impervious to the effects of integral nonlinearity. Pixel-specific gain amplification must be characterized to properly compensate for any misalignment that may result from the energy-dependent nonlinearity. The nonlinearity is readily quantified without the aid of principal components; to do so with the PCA methodology would require significant modifications that are otherwise unnecessary. Therefore, the nonlinearity calibration is performed in a similar fashion to the method described by Zhang [46], in which the true incident gamma-ray energy is modeled as a function of energy deposition estimates. Nonlinearity is modeled for each anode pixel individually to specifically target differences in front-end electronics and the effects of pixel orientation. As demonstrated in Figure 6.4, the true energy can be accurately regressed as a function of the observed centroids using a polynomial model. The regressed trend closely resembles perfect linearity up to approximately 1 MeV. Beyond this threshold, observed photopeak centroids systematically exceed their true value.

Uncertainty in polynomial regression model parameters transfers to the updated, gain-corrected energy estimate. The independent variable for this gain-correction model, observed photopeak centroid, is severely heteroscedastic due to the single-pixel event efficiency in pixelated CdZnTe detectors. Low-energy centroids may be estimated with greater precision compared to high-energy centroids at which detection occurs infrequently. The heteroscedastic nature of data precludes theoretical estimates of the regression precision as a function of energy. However, the uncertainty in gain-corrected energy deposition can be estimated more effectively via bootstrapping [99]. This method entails replicating the single-pixel energy spectrum from which the observed photopeak centroids were determined. For each realization of this spectrum, regress the nonlinearity model and use it to estimate the gain-corrected energy deposition of an event. By these means, one can estimate the statistical variance in the

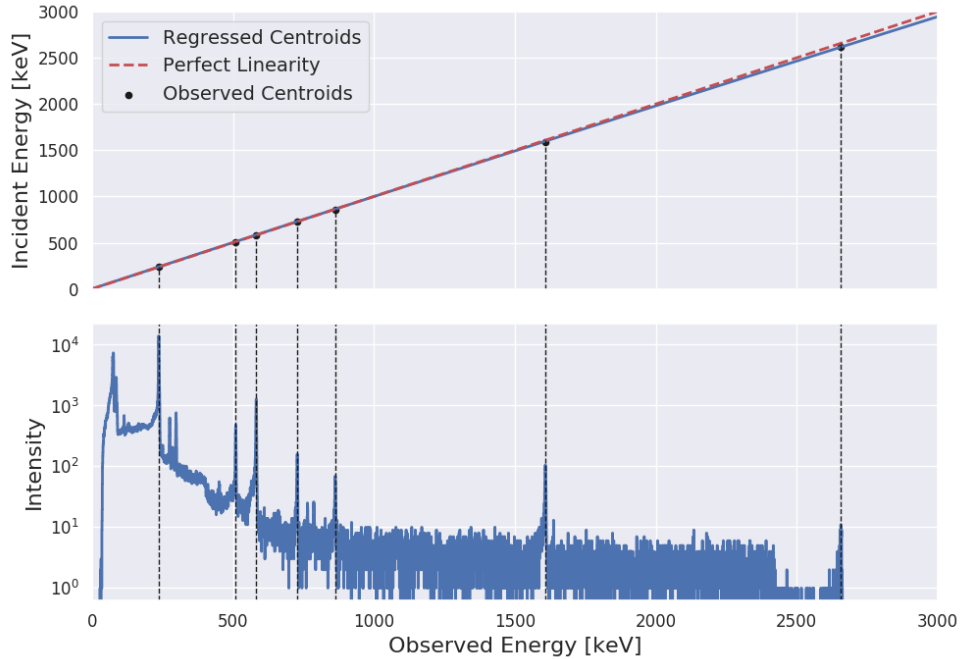


Figure 6.4: Model of nonlinearity derived from the observed photopeak centroids (top) in the spectrum of single-pixel events collected by a single anode pixel (bottom).

gain-corrected energy estimate attributed to the nonlinearity regression model.

Figure 6.5 provides the distributions of gain-corrected energy estimates at various energies for  $1 \times 10^4$  realizations of the single-pixel energy spectrum acquired by an anode pixel. The distributions suggest that nonlinearity compensation induces more uncertainty for gamma-ray events at the high end of the energy spectrum, whereas the uncertainty in gain-corrected below 1 MeV is relatively negligible. Despite the statistical variance at high gamma-ray energy, it is preferable to the systematic error that existed prior to the nonlinearity correction.

After application of nonlinearity corrections, the single-pixel energy resolution achieved by PCA monotonically decreases as a function of incident gamma-ray energy, and it adheres to the behavior that is predicted by conventional thought (Figure 6.6). With the same gain-correction procedure, the energy resolution achieved by SRF also improves at high incident gamma-ray energies, yet fails to produce the same

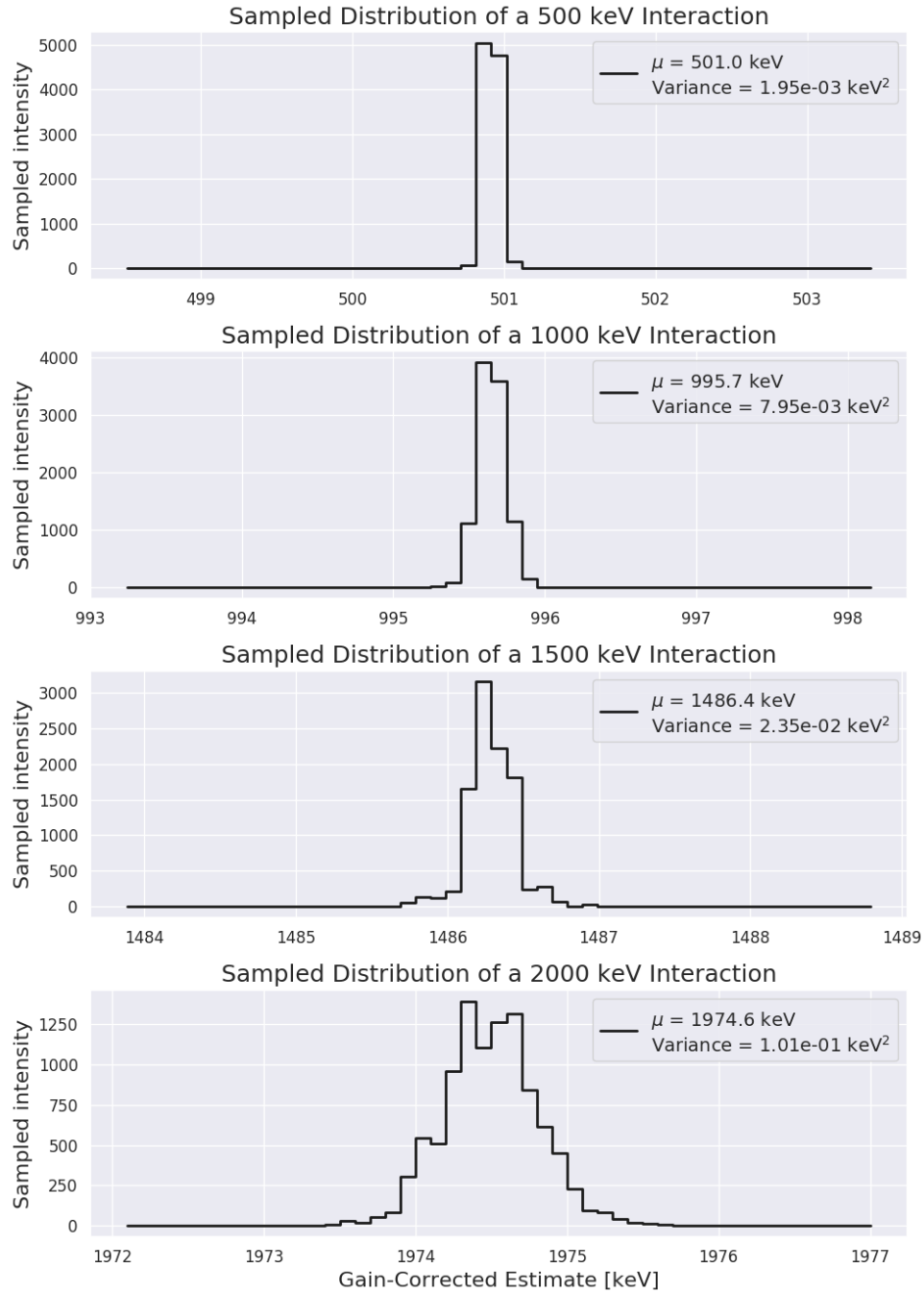


Figure 6.5: Distribution of gain-corrected energy estimates produced from  $1 \times 10^4$  realization of the  $^{228}\text{Th}$  spectrum for various gamma-ray energies.

improvement as that of PCA. Note that the energy resolution at the lower end of the spectrum does not change significantly, as this energy regime is less severely affected by nonlinearity.

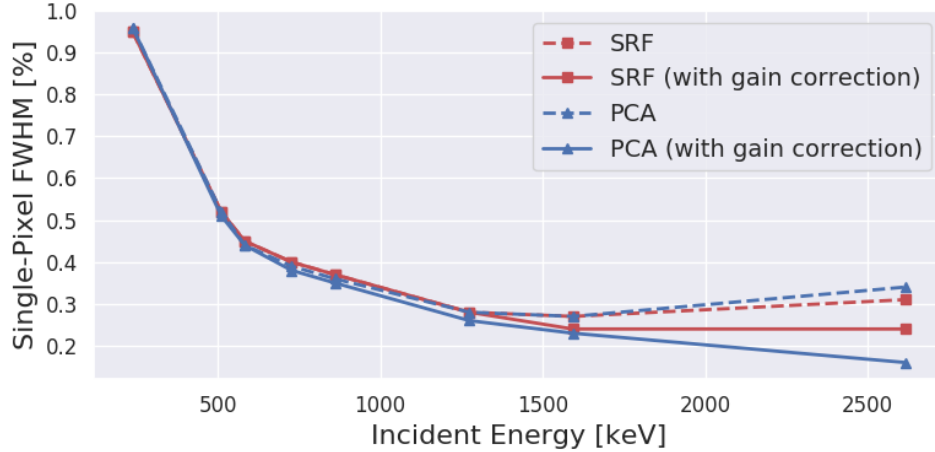


Figure 6.6: Single-pixel energy resolution as a function of incident gamma-ray energy for SRF and PCA with and without gain corrections.

Despite identical gain-correction procedures, the performance of PCA improves more significantly than SRF. The gain correction aligns the pixel-specific photopeaks under one aggregate photopeak with a common centroid. The correction eliminates variance in pixel-specific centroids, but makes no attempt to reduce variance in energy deposition estimates acquired by individual pixels. The nonlinearity correction multiplies the original energy estimates by a factor, which only serves to scale the variance of energy estimates of interactions collected by any given pixel. This is more concisely described by the axiomatic relationship in Equation 6.2, in which  $b$  is analogous to the nonlinearity correction factor and  $E$  represents the energy deposition estimates of a collection of monoenergetic photopeak events. As all samples of  $E$  correspond to a single incident gamma-ray energy, the factor  $b$  remains roughly constant. The correction factor merely scales the variance in a photopeak, implying that a pixel achieving better energy resolution under the PCA methodology remains superior to SRF after nonlinearity correction.

$$\text{Var}(bE) = b^2 \text{Var}(E) \quad (6.2)$$

To illustrate this point, consider the distributions of pixel-specific energy resolution for two select photopeaks in Figure 6.7. The pixel-specific energy resolutions that constitute these distributions are obtained before the application of nonlinearity corrections. Relative to the resolution achieved by SRF, the corresponding distributions for the PCA methodology are more heavily weighted towards lower FWHM values. These observations provide evidence consistent with the greater improvement in single-pixel energy resolution for PCA upon application of nonlinearity correction.

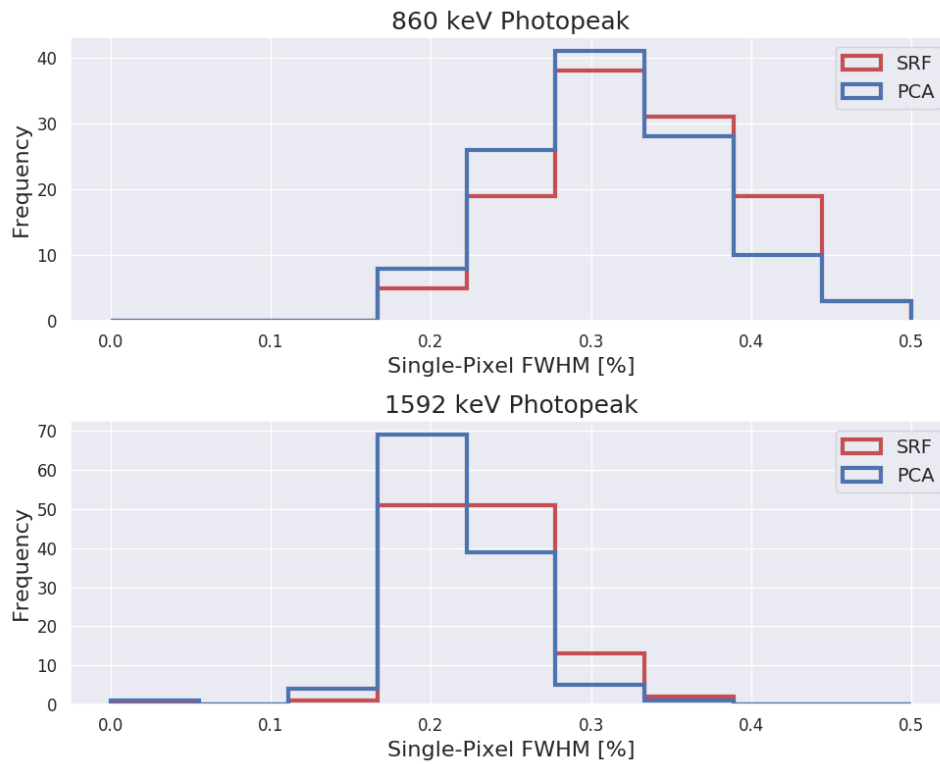


Figure 6.7: Distribution of single-pixel energy resolution achieved by SRF and principal component regression before the application of nonlinearity compensation. The top pane displays the distribution for 860 keV photopeaks, whereas the bottom pane contains the distribution for the 1592 keV single-escape peak.

The next logical question in this analysis is whether PCA can provide some insight into ways in which energy resolution can improve further. As the gain-correction model is determined from aggregate data across all depths of interaction, it does not

account for the depth-specific gain. As detailed in Chapter II, anode-side interactions have lower amplitude response due to the small-pixel effect. Therefore, anode-side interactions still have some deficit in reconstructed energy, as demonstrated in Figure 6.8. Despite the application of nonlinearity compensation, the reconstructed energy of anode-side interactions - indicated by low values of the depth in arbitrary units - appears systematically lower than the 2614 keV incident energy. Given the paucity of empirical data for high-energy interactions, determining a depth-specific nonlinearity correction is impractical. The question now shifts to whether PCA can provide some path for correction that is more resilient to insufficient amounts of empirical data.

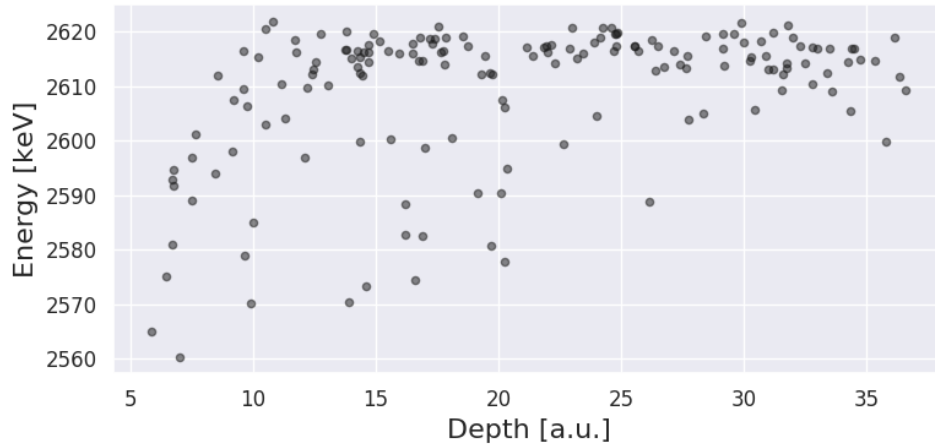


Figure 6.8: Gain-compensated, reconstructed energy of single-pixel, 2614 keV interactions as a function of depth for a single channel.

Up to this point in the analysis, principal components were determined by the eigenvectors from decomposition of observations in which less than or equal to 662 keV was deposited. While these principal components helped construct predictive models for energy deposition in events with less than 1 MeV, they may not necessarily embed pertinent information for interactions at higher energies. In an attempt to target mechanisms more relevant to high-energy interactions, PCA was performed on the observations collected from a separate  $^{228}\text{Th}$  measurement. Only observations that exceeded 1.5 MeV were included in the analysis.

Select eigenvectors produced by this revised analysis are compared to those from the  $^{137}\text{Cs}$  data in Figure 6.9. As in previous plots of eigenvectors, vertical lines separate signals from the collecting anode pixel, cathode, and four pixels adjacent to the collecting pixel. The eigenvector that corresponds to the first principal component (top pane) reveals effectively similar information about the depth of interaction. This is indicated by the substantial weight given to the cathode signal and the neighbor pixel tail regions.

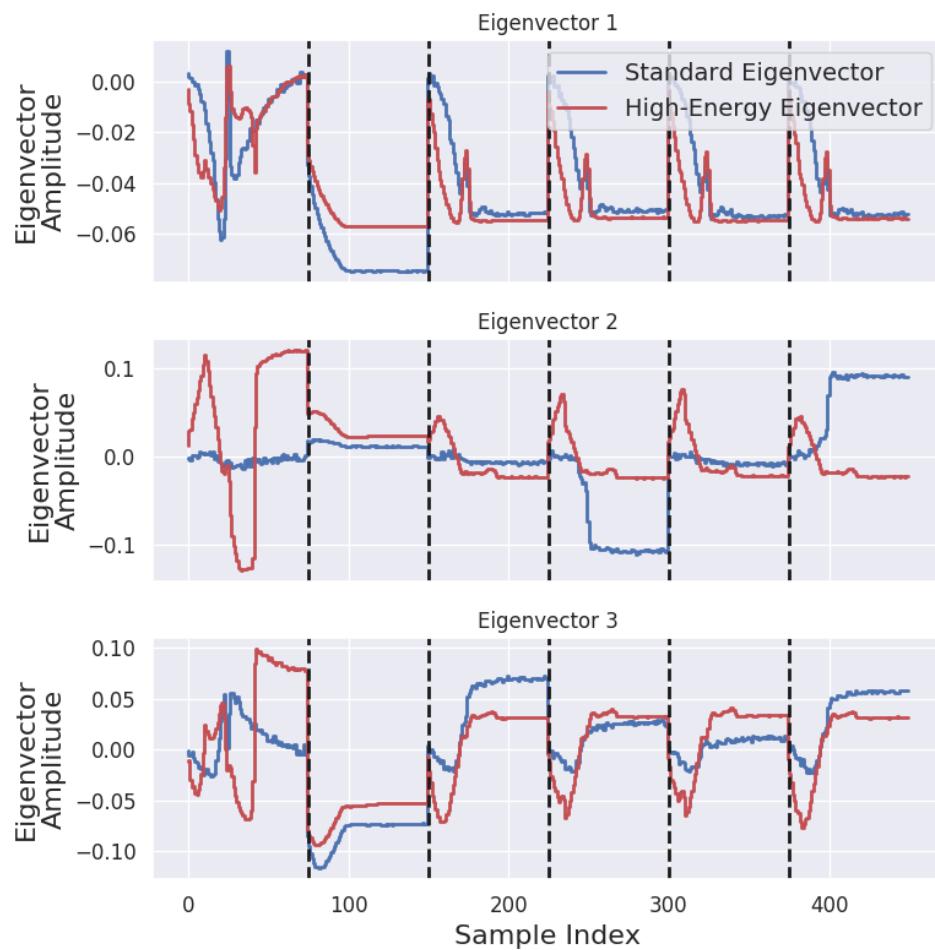


Figure 6.9: Comparison of eigenvectors generated from  $^{137}\text{Cs}$  data and high-energy data for the first three principal components for an anode pixel. The first, second and third principal component eigenvectors are featured in the top, middle and bottom panes, respectively. The vertical, dotted lines separate the signals obtained from the collecting anode pixel, cathode and four neighbor pixels adjacent to the collecting pixel.

However, the two subsequent eigenvectors exhibit demonstrable differences. Consider the eigenvectors for the second principal component (middle pane). The  $^{137}\text{Cs}$  data eigenvectors provide information about subpixel position, as indicated by the opposite polarities of the top and bottom neighbor pixel tail regions (fourth and sixth segments, respectively). The high-energy eigenvector provides no preference for any neighbor pixel tails, and it implies that this eigenvector does not embed subpixel position information. This observation also applies to the third eigenvector (bottom pane).

These observations are consistent with intuition regarding high-energy, single-pixel events. When a large amount of energy is deposited, interactions near pixel boundaries generally trigger at least one of the neighboring pixels. Only interactions that occur in the lateral center of a pixel generate single-pixel events eligible for this analysis. For this reason, high-energy events cannot be distinguished effectively by lateral, subpixel position.

Upon gathering these high-energy-specific eigenvectors, principal component regression was evaluated once again to obtain new calibration parameters. The resulting energy resolution was tabulated, and the results are compared to those obtained with the standard set of calibration parameters in Figure 6.10. Despite changes in the eigenvectors, there are negligible changes in the achievable energy resolution across the energy domain. As with the results presented in Chapters IV and V, most of the improvement is achieved after the first principal component correction. The first principal component is effectively unchanged between the two approaches, and the results in Figure 6.10 suggest that the subsequent principal component corrections mitigate systematic error in energy reconstruction to nearly similar effect.

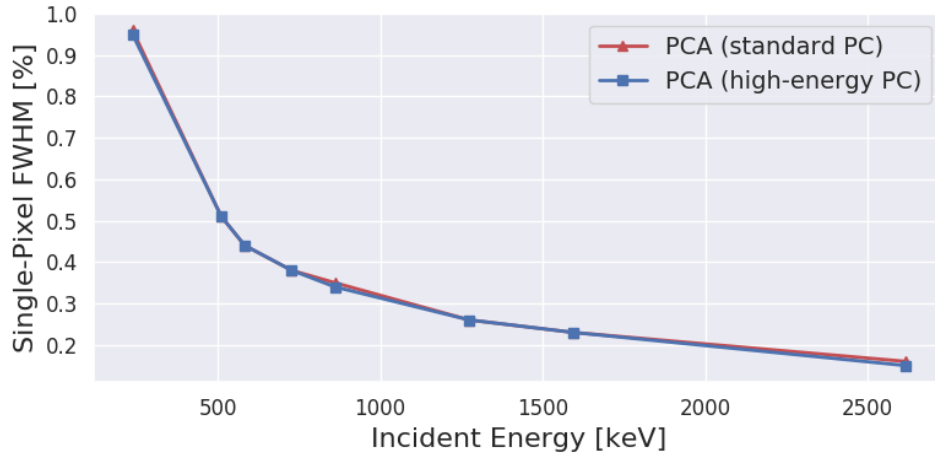


Figure 6.10: Single-pixel energy resolution as a function of incident gamma-ray energy for principal component regression with standard and high-energy principal components.

### 6.3 Principal Component Regression for Multiple-Pixel Results

As with single-pixel events, the interactions constituting multiple-pixel events are subject to integral nonlinearity from the front-end electronics. The gain-compensation model regressed from single-pixel events provides the requisite information to compensate for this nonlinearity. These corrections are applied before application of the principal component corrections to preserve consistent relationships between total energy deposition and principal components. The resulting two-pixel energy resolution is compared to the results achieved by SRF in Figure 6.11.

The energy resolution obtained with the PCA methodology compares favorably to SRF, but the advantage diminishes at progressively higher incident energy. The two approaches feature nearly identical gain-correction procedures. As discussed in the previous section, the uncertainty introduced by nonlinearity compensation is negligible at low energies. However, this uncertainty increases in energy due to statistical uncertainty in the training data for high-energy centroids. Principal component regression fails to mitigate statistical uncertainty of this nature, which accounts for the

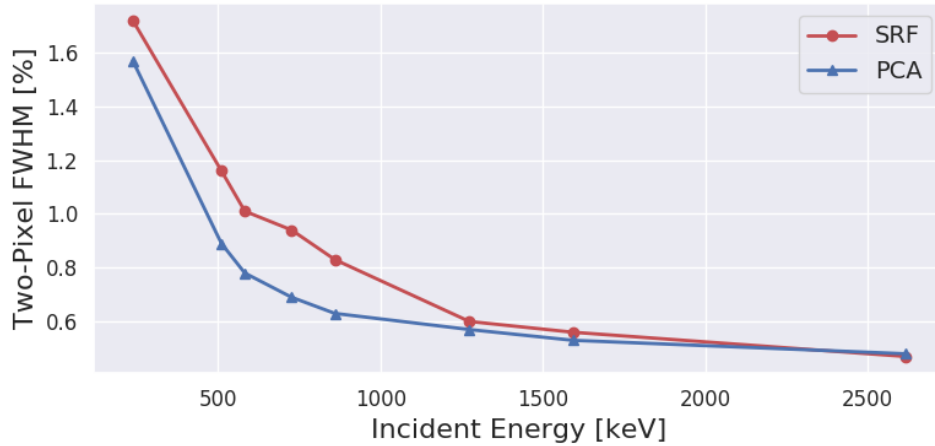


Figure 6.11: Two-pixel energy resolution as a function of incident gamma-ray energy for SRF and PCA.

diminishing returns in achievable energy resolution at high incident energy.

Similar to the methods presented for single-pixel events, PCA can be performed on a set of high-energy observations exclusively. However, statistical uncertainty in the nonlinearity compensation still afflicts the results obtained with the PCA methodology as demonstrated in Figure 6.12. Therefore, the modified principal components obtained with these high-energy eigenvectors do not yield significant improvement over the standard principal components for  $^{137}\text{Cs}$ . Despite the additional statistical uncertainty associated with nonlinearity correction, it remains necessary to achieve the optimal performance from principal component regression.

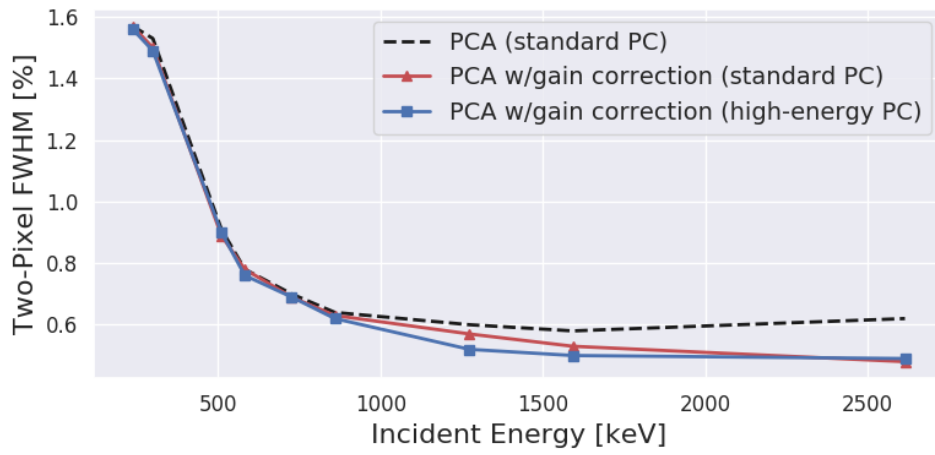


Figure 6.12: Two-pixel energy resolution as a function of incident gamma-ray energy for PCA with a variety of modifications.

## CHAPTER VII

### Summary and Future Work

#### 7.1 Summary

Judicious use of digitized waveforms has been an elusive goal for event reconstruction with 3-D position-sensitive CdZnTe detector technology since the introduction of the digital ASIC front-end architecture. Previous reconstruction methods such as SRF partially achieved this goal, but it did not diminish the reliance on *a posteriori* corrections for sources of systematic error that obfuscate the estimation of gamma-ray interaction attributes. Despite marginal improvements in energy resolution for certain subsets of gamma-ray interactions, it requires computationally intensive inverse methods that render it impractical for applications that need rapid event processing.

The novel methods presented in this work provide yet another approach to leveraging the full extent of digitized waveforms by means of PCA. As demonstrated in Chapter III, the decomposition provided by PCA identifies gamma-ray interaction characteristics in the form of principal components from digitized samples. This methodology allows one to extract valuable information embedded within digitized waveforms that may be otherwise neglected by methods developed by human intuition and physics-based models. It does so without sacrificing the capability to interpret physical meaning from these latent variables that would otherwise be obscured by alternative, statistically-driven methods like deep learning.

The principal component regression methodology described in Chapter IV models the relationship between principal components and energy deposition. It reveals the ways in which systematic error manifests in the initial estimates of energy deposition, and it corrects for this error accordingly. This methodology offers on the order of 10% improvement relative to established reconstruction techniques with respect to FWHM and FWTM for single-pixel events. This performance relies on computational subroutines with  $O(n)$  complexity. As such, the processing time per single-pixel event for principal component regression consumes approximately 75% of the time required to process an event with the fastest alternative, trapezoidal filtering.

The proposed PCA methodology is extended to multiple-pixel events in Chapter V, albeit with the aid of feature engineering to address challenges specific to these increasingly complex events. Under this framework, the two-pixel event FWHM at 662 keV was improved by 10% compared to the leading alternative technique for this metric, SRF. The improved energy resolution comes at a minor expense of event processing speed, as it requires approximately 10% more time to process a two-pixel using the default configurations than that of the expedient trapezoidal filtering approach. This PCA framework was generalized for application to higher-order events, and the performance was presented for three and four-pixel events. Three-pixel event FWHM improves by an order of 10% with principal component regression, but the results become comparable to alternative methods for four-pixel events. The results for the latter reveal the sensitivity to systematic error in depth reconstruction of interactions with small energy depositions for the PCA methodology.

Energy reconstruction for high-energy events entails additional sources of systematic error, but not all of which require principal components. Integral nonlinearity in front-end electronics comprises a significant component of systematic error, and it is readily quantified and modeled without principal components. After application of nonlinearity compensation, single-pixel energy resolution obtained with principal

component regression improves considerably. This improvement becomes increasingly more significant as a function of incident gamma-ray energy, and it enables PCA to achieve an approximately 30% reduction in FWHM at 2614 keV relative to SRF. An alternative set of eigenvectors were computed using high-energy events exclusively to target the remaining sources of systematic error, but this new set of information yielded negligible improvement relative to the performance achieved with eigenvectors produced by the decomposition of relatively low-energy  $^{137}\text{Cs}$  data. The reconstruction of high-energy, multiple-pixel events also benefited significantly from nonlinearity compensation. Upon this correction, PCA consistently provided better two-pixel energy resolution up to events with 1500 keV energy deposition. However, the statistical uncertainty introduced by gain correction limited the ability to mitigate systematic error at higher energies. Consequently, SRF and PCA produced nearly similar two-pixel energy resolution beyond 1500 keV.

## 7.2 Future Work

The principal component regression methods presented in this work address the elusive goal of achieving full utilization of the sampled waveforms. The PCA methodology decomposes such waveforms in pursuit of the fundamental properties that distinguish waveforms, and the implications of this analysis with regards to performing energy reconstruction have been detailed thoroughly in Chapters IV, V and VI. However, event reconstruction describes the process by which all interaction parameters are estimated, not just energy deposition. The event reconstruction process also entails the estimation of the position of interaction.

The application of principal component regression towards the estimation of 3-D position was investigated, but the efforts towards this task yielded uninspiring results. The presented methods provided promising results for energy reconstruction due in part to a well-characterized ground truth. The energy of emitted gamma

rays are known with a small degree of uncertainty, and this enables the judicious use of supervised regression to model the estimated energy as a function of principal components.

The position parameters for gamma-ray interactions do not have known values with which to perform supervised learning. Having precise position estimates is theoretically achievable, but it requires inefficient, collimated measurements to restrict the position of interaction to within a small volume in a detector. The best estimates of such parameters are derived from physics-based models. Consequently, any hypothetical regression models designed to estimate these parameters in a supervised fashion cannot achieve better precision than those predicted by the established methods discussed in Section 2.4. Doing so would undermine the use of principal component regression.

This does not imply that the information embedded within sampled waveforms provides no predictive capability for 3-D gamma-ray interaction position. One may resort to forms of unsupervised learning to properly leverage such information without relying on the presence of a ground truth. At the time of this writing, these methods are well-established for numerous classification and regression tasks. With adequate knowledge of such methods, the author speculates that systematic error may be mitigated to the same extent as that of energy reconstruction. This achievement offers profound implications for improving the performance of Compton imaging with 3-D position-sensitive CdZnTe detectors, as imaging resolution tends to be more sensitive to errors in position estimates than energy estimates [48].

The implications for progress in position estimation are not limited to Compton imaging performance. In the context of multiple-pixel event reconstruction, the accuracy of energy reconstruction in higher-order events - and in particular those containing interactions in which only a small amount of energy is deposited - depend on accurate depth reconstruction to an extent. Systematic error in depth reconstruction

propagates into energy reconstruction, and it is not completely mitigated by principal component regression. If the position were estimated using the underlying statistical properties embedded within sampled waveforms rather than the existing, heavy reliance on physics-based models, it is expected that principal component regression can yield better energy resolution for higher-order events than that demonstrated in this work.

The recommendations for future work are not limited to position reconstruction; aspects of PCA for energy reconstruction also require attention. The methods detailed in this work implicitly assume that the data on which PCA is performed is homoscedastic across and within observations despite the overwhelming evidence to suggest otherwise. The difference in noise between the anode and cathode signals accounts for heteroscedasticity within samples, and low-amplitude events have higher noise compared to observations with higher amplitude.

Future work on this subject matter should consider the impact of heteroscedastic data - within and across observations - more thoroughly. As indicated by Hong et al., asymptotic recovery of the principal subspace is sensitive to heteroscedasticity across observations [100]. With regards to heteroscedasticity within samples, it is expected that a more appropriate scaling strategy for the input signals would promote homoscedastic tendencies. In a closely-related matter, future developments should evaluate the impact of outlier data on subspace recovery. This impact was ignored throughout this work, but it merits consideration as indicated by the work of [101].

## BIBLIOGRAPHY

## BIBLIOGRAPHY

- [1] P. Kennedy, *The rise and fall of the great powers*. Vintage, 2010.
- [2] G. P. Shultz, W. J. Perry, H. A. Kissinger, S. Nunn, *et al.*, “A world free of nuclear weapons,” *Wall Street Journal*, vol. 4, no. 01, p. 2007, 2007.
- [3] T. B. Taylor, “Nuclear safeguards,” *Annual Review of Nuclear Science*, vol. 25, no. 1, pp. 407–421, 1975.
- [4] G. F. Knoll, *Radiation detection and measurement*. John Wiley & Sons, 2010.
- [5] A. Perez-Andujar and L. Pibida, “Performance of cdte, hpge and nai (tl) detectors for radioactivity measurements,” *Applied radiation and isotopes*, vol. 60, no. 1, pp. 41–47, 2004.
- [6] R. Harry, J. Aaldijk, and J. Braak, “Gamma-spectrometric determination of isotopic composition without use of standards,” *Safeguarding Nuclear Materials*, p. 235, 1976.
- [7] R. Hagenauer, “Nondestructive determination of uranium enrichment using low energy x and gamma rays,” *Nuclear Materials Management/1982, Inmm Proceedings*, 1983.
- [8] B. Deb, J. F. Ross, A. Ivan, and M. J. Hartman, “Radioactive source estimation using a system of directional and non-directional detectors,” *IEEE Transactions on Nuclear Science*, vol. 58, no. 6, pp. 3281–3290, 2011.
- [9] D. Goodman, M. Streicher, Y. Zhu, and Z. He, “Identification of intervening materials in gamma-ray spectroscopy measurements using angularly deconvolved spectra with multiple sources in the field of view,” *IEEE Transactions on Nuclear Science*, vol. 65, no. 3, pp. 924–931, 2018.
- [10] H. O. Anger, “Scintillation camera with multichannel collimators,” 1964.
- [11] D. Everett, J. Fleming, R. Todd, and J. Nightingale, “Gamma-radiation imaging system based on the compton effect,” in *Proceedings of the Institution of Electrical Engineers*, vol. 124, p. 995, IET, 1977.
- [12] E. E. Fenimore and T. M. Cannon, “Coded aperture imaging with uniformly redundant arrays,” *Applied optics*, vol. 17, no. 3, pp. 337–347, 1978.

- [13] N. Dogan, D. K. Wehe, and G. F. Knoll, “Multiple Compton scattering gamma ray imaging camera,” *Nuclear Instruments and Methods in Physics Research Section A: Accelerators, Spectrometers, Detectors and Associated Equipment*, vol. 299, no. 1-3, pp. 501–506, 1990.
- [14] D. Reilly, N. Ensslin, H. Smith Jr, and S. Kreiner, “Passive nondestructive assay of nuclear materials,” tech. rep., Nuclear Regulatory Commission, Washington, DC (United States). Office of , 1991.
- [15] L. Kull and R. Ginaven, “Guidelines for gamma-ray spectroscopy measurements of  $^{235}\text{U}$  enrichment,” tech. rep., Brookhaven National Lab., Upton, NY (USA), 1974.
- [16] J. Parker and T. Reilly, “Plutonium isotopic determination by gamma-ray spectroscopy,” *Nuclear analysis research and development program status report*, 1974.
- [17] R. Gunnink, J. Niday, and P. Siemens, “System for plutonium analysis by gamma ray spectrometry. part i. techniques for analysis of solutions,” tech. rep., California Univ., 1974.
- [18] T. Dragnev and K. Schärff, “Non-destructive gamma spectrometry measurement of  $^{239}\text{Pu}/^{240}\text{Pu}$  and  $\text{Pu}/^{240}\text{Pu}$  ratios,” *The International Journal of Applied Radiation and Isotopes*, vol. 26, no. 3, pp. 125–129, 1975.
- [19] S. Hsue, T. Crane, W. Talbert Jr, and J. C. Lee, “Nondestructive assay methods for irradiated nuclear fuels,” tech. rep., Los Alamos Scientific Lab., N. Mex.(USA), 1978.
- [20] A. Ramalho and W. Payne, “Spent fuel measurements using high resolution gamma systems,” *Nuclear Materials Management*, vol. 8, no. 3, pp. 76–82, 1979.
- [21] J. Phillips, J. K. Halbig, D. Lee, S. Beach, T. Bement, E. Dermendjiev, C. Hatcher, K. Kaieda, and E. Medina, “Application of nondestructive gamma-ray and neutron techniques for the safeguarding of irradiated fuel materials,” tech. rep., Los Alamos Scientific Lab., 1980.
- [22] M. Streicher, S. Brown, Y. Zhu, D. Goodman, and Z. He, “Special nuclear material characterization using digital 3-d position sensitive CdZnTe detectors and high purity germanium spectrometers,” *IEEE Transactions on Nuclear Science*, vol. 63, no. 5, pp. 2649–2656, 2016.
- [23] H. Barber, H. Barrett, E. Dereniak, N. Hartsough, D. Perry, P. Roberts, M. Rogulski, J. Woolfenden, and E. Young, “A gamma-ray imager with multiplexer readout for use in ultra-high-resolution brain spect,” *IEEE Transactions on nuclear science*, vol. 40, no. 4, pp. 1140–1144, 1993.

- [24] H. Barber, F. Augustine, H. Barrett, E. Dereniak, K. Matherson, T. Meyers, D. Perry, J. Venzon, J. Woolfenden, and E. Young, "Semiconductor arrays with multiplexer readout for gamma-ray imaging: results for a  $48 \times 48$  ge array," *Nuclear Instruments and Methods in Physics Research Section A: Accelerators, Spectrometers, Detectors and Associated Equipment*, vol. 353, no. 1-3, pp. 361–365, 1994.
- [25] D. Marks, H. Barber, H. H. Barrett, E. Dereniak, J. Eskin, K. Matherson, J. Woolfenden, E. Young, F. Augustine, W. Hamilton, *et al.*, "A  $48 \times$  cdznte array with multiplexer readout," *IEEE Transactions on Nuclear Science*, vol. 43, no. 3, pp. 1253–1259, 1996.
- [26] P. Luke, "Unipolar charge sensing with coplanar electrodes-application to semiconductor detectors," *IEEE Transactions on Nuclear Science*, vol. 42, no. 4, pp. 207–213, 1995.
- [27] J. M. Ryan, J. R. Macri, M. L. McConnell, B. K. Dann, M. L. Cherry, T. G. Guzik, F. P. Doty, B. A. Apotovsky, and J. F. Butler, "Large-area submillimeter resolution cdznte strip detector for astronomy," in *EUV, X-Ray, and Gamma-Ray Instrumentation for Astronomy VI*, vol. 2518, pp. 292–302, International Society for Optics and Photonics, 1995.
- [28] C. M. Stahle, A. M. Parsons, L. M. Bartlett, P. Kurczynski, J. F. Krizmanic, L. M. Barbier, S. D. Barthelmy, F. Birsa, N. A. Gehrels, J. L. Odom, *et al.*, "Cdznte strip detector for arcsecond imaging and spectroscopy," in *Hard X-Ray/Gamma-Ray and Neutron Optics, Sensors, and Applications*, vol. 2859, pp. 74–85, International Society for Optics and Photonics, 1996.
- [29] Z. He, "Review of the shockley–ramo theorem and its application in semiconductor gamma-ray detectors," *Nuclear Instruments and Methods in Physics Research Section A: Accelerators, Spectrometers, Detectors and Associated Equipment*, vol. 463, no. 1-2, pp. 250–267, 2001.
- [30] F. Doty, H. Barber, F. Augustine, J. Butler, B. Apotovsky, E. Young, and W. Hamilton, "Pixellated cdznte detector arrays," *Nuclear Instruments and Methods in Physics Research Section A: Accelerators, Spectrometers, Detectors and Associated Equipment*, vol. 353, no. 1-3, pp. 356–360, 1994.
- [31] H. H. Barrett, J. Eskin, and H. Barber, "Charge transport in arrays of semiconductor gamma-ray detectors," *Physical Review Letters*, vol. 75, no. 1, p. 156, 1995.
- [32] H. Spieler, *Semiconductor detector systems*, vol. 12. Oxford university press, 2005.
- [33] D. Olego, J. Faurie, S. Sivananthan, and P. Raccah, "Optoelectronic properties of cd1- x zn x te films grown by molecular beam epitaxy on gaas substrates," *Applied physics letters*, vol. 47, no. 11, pp. 1172–1174, 1985.

- [34] G. Bertolini and A. Coche, “Semiconductor detectors.,” 1968.
- [35] E. Sakai, “Present status of room temperature semiconductor detectors,” *Atomnaya Tekhnika za Rubezhom*, pp. 29–35, 1984.
- [36] D. McGregor and H. Hermon, “Nucl. instrum. methods phys. res. a,” 1997.
- [37] Z. Burshtein, H. Jayatirtha, A. Burger, J. Butler, B. Apotovsky, and F. Doty, “Charge-carrier mobilities in  $\text{Cd}_0.8\text{Zn}_0.2\text{Te}$  single crystals used as nuclear radiation detectors,” *Applied physics letters*, vol. 63, no. 1, pp. 102–104, 1993.
- [38] S. Taherion, E. Chen, P. Lu, J. Kumar, P. Wang, P. Kharzaei, Z. He, Y. Zhu, M. Streicher, B. Williams, and J. Xia, “Cadmium-zinc-telluride fabrication and material improvements, a few steps closer to hpge performance.” IEEE Nuclear Science Symposium and Medical Imaging Conference, 2017.
- [39] W. Shockley, “Currents to conductors induced by a moving point charge,” *Journal of applied physics*, vol. 9, no. 10, pp. 635–636, 1938.
- [40] S. Ramo, “Currents induced by electron motion,” *Proceedings of the IRE*, vol. 27, no. 9, pp. 584–585, 1939.
- [41] W. A. Strauss, *Partial differential equations: An introduction*. Wiley, 2007.
- [42] J. Eskin, H. Barrett, and H. Barber, “Signals induced in semiconductor gamma-ray imaging detectors,” *Journal of applied physics*, vol. 85, no. 2, pp. 647–659, 1999.
- [43] Y. Zhu, “Digital signal processing methods for pixelated 3-d position sensitive room-temperature semiconductor detectors.,” 2012.
- [44] H. Yang, “Applications of digital asic array system for noise analysis, non-linearity correction, event classification and reconstruction.,” 2013.
- [45] M. Streicher, “Applications of digitized 3-d position-sensitive  $\text{CdZnTe}$  spectrometers for national security and nuclear nonproliferation,” 2017.
- [46] F. Zhang, “Events reconstruction in 3-d position sensitive  $\text{CdZnTe}$  gamma-ray spectrometers,” 2005.
- [47] W. R. Kaye, “Event reconstruction in pixelated  $\text{CdZnTe}$  detectors,” *University of Michigan, Ann Arbor, MI, PhD Thesis*, 2011.
- [48] W. Wang, “Techniques and applications of compton imaging for position-sensitive gamma-ray detectors,” 2011.
- [49] Z. He, G. F. Knoll, D. K. Wehe, R. Rojeski, C. H. Mastrangelo, M. Hammig, C. Barrett, and A. Uritani, “1-d position sensitive single carrier semiconductor detectors,” *Nuclear Instruments and Methods in Physics Research Section A: Accelerators, Spectrometers, Detectors and Associated Equipment*, vol. 380, no. 1-2, pp. 228–231, 1996.

- [50] W. Li, Z. He, G. Knoll, D. Wehe, and C. Stahle, “Spatial variation of energy resolution in 3-d position sensitive czts gamma-ray spectrometers,” in *Nuclear Science Symposium, 1998. Conference Record. 1998 IEEE*, vol. 1, pp. 628–633, IEEE, 1998.
- [51] Y. Zhu, S. E. Anderson, and Z. He, “Sub-pixel position sensing for pixelated, 3-d position sensitive, wide band-gap, semiconductor, gamma-ray detectors,” *IEEE Transactions on Nuclear Science*, vol. 58, no. 3, pp. 1400–1409, 2011.
- [52] F. Zhang, Z. He, D. Xu, G. F. Knoll, D. K. Wehe, and J. E. Berry, “Improved resolution for 3-d position sensitive cdznte spectrometers,” *IEEE Transactions on Nuclear Science*, vol. 51, no. 5, pp. 2427–2431, 2004.
- [53] V. T. Jordanov and G. F. Knoll, “Digital synthesis of pulse shapes in real time for high resolution radiation spectroscopy,” *Nuclear Instruments and Methods in Physics Research Section A: Accelerators, Spectrometers, Detectors and Associated Equipment*, vol. 345, no. 2, pp. 337–345, 1994.
- [54] K. Levenberg, “A method for the solution of certain non-linear problems in least squares,” *Quarterly of applied mathematics*, vol. 2, no. 2, pp. 164–168, 1944.
- [55] D. W. Marquardt, “An algorithm for least-squares estimation of nonlinear parameters,” *Journal of the society for Industrial and Applied Mathematics*, vol. 11, no. 2, pp. 431–441, 1963.
- [56] L. N. Trefethen and D. Bau III, *Numerical linear algebra*, vol. 50. Siam, 1997.
- [57] G. H. Golub and C. F. Van Loan, *Matrix computations*, vol. 3. JHU Press, 2012.
- [58] H. Hotelling, “Analysis of a complex of statistical variables into principal components.,” *Journal of educational psychology*, vol. 24, no. 6, p. 417, 1933.
- [59] G. Strang, *Linear algebra and its applications*. Belmont, CA: Thomson, Brooks/Cole, 2006.
- [60] Y. Nakatsukasa and N. J. Higham, “Stable and efficient spectral divide and conquer algorithms for the symmetric eigenvalue decomposition and the svd,” *SIAM Journal on Scientific Computing*, vol. 35, no. 3, pp. A1325–A1349, 2013.
- [61] R. K. Narang, *Inside the Black Box: A Simple Guide to Quantitative and High Frequency Trading*, vol. 883. John Wiley & Sons, 2013.
- [62] C. O’Neil, *Weapons of math destruction: How big data increases inequality and threatens democracy*. Broadway Books, 2017.
- [63] A. Bolotnikov, G. Camarda, G. Wright, and R. James, “Factors limiting the performance of cdznte detectors,” *IEEE transactions on nuclear science*, vol. 52, no. 3, pp. 589–598, 2005.

- [64] G. Yang, A. Bolotnikov, Y. Cui, G. Camarda, A. Hossain, and R. James, “Impurity gettering effect of te inclusions in cdznte single crystals,” *Journal of Crystal Growth*, vol. 311, no. 1, pp. 99–102, 2008.
- [65] A. Shor, Y. Eisen, and I. Mardor, “Edge effects in pixelated cdznte gamma detectors,” in *Nuclear Science Symposium Conference Record, 2003 IEEE*, vol. 5, pp. 3342–3345, IEEE, 2003.
- [66] T. Alharbi, “Principal component analysis for pulse-shape discrimination of scintillation radiation detectors,” *Nuclear Instruments and methods in Physics Research Section A: Accelerators, Spectrometers, Detectors and Associated Equipment*, vol. 806, pp. 240–243, 2016.
- [67] H. Theil, “A rank-invariant method of linear and polynomial regression analysis,” in *Henri Theils contributions to economics and econometrics*, pp. 345–381, Springer, 1992.
- [68] P. K. Sen, “Estimates of the regression coefficient based on kendall’s tau,” *Journal of the American statistical association*, vol. 63, no. 324, pp. 1379–1389, 1968.
- [69] P. J. Rousseeuw and A. M. Leroy, *Robust regression and outlier detection*, vol. 589. John wiley & sons, 2005.
- [70] C. Bishop, *Pattern recognition and machine learning*, vol. 4. Springer New York, 2006.
- [71] M. Kuhn and K. Johnson, *Applied predictive modeling*, vol. 26. Springer, 2013.
- [72] M. Frigo and S. G. Johnson, “The design and implementation of fftw3,” *Proceedings of the IEEE*, vol. 93, no. 2, pp. 216–231, 2005.
- [73] M. Frigo and S. G. Johnson, “Fftw: An adaptive software architecture for the fft,” in *Acoustics, Speech and Signal Processing, 1998. Proceedings of the 1998 IEEE International Conference on*, vol. 3, pp. 1381–1384, IEEE, 1998.
- [74] E. Wang, Q. Zhang, B. Shen, G. Zhang, X. Lu, Q. Wu, and Y. Wang, “Intel math kernel library,” in *High-Performance Computing on the Intel® Xeon Phi*, pp. 167–188, Springer, 2014.
- [75] N. M. Josuttis, *The C++ standard library: a tutorial and reference*. Addison-Wesley, 2012.
- [76] J. D. HUTCHINSON and D. J. LOAIZA, “Plutonium sphere reflected by beryllium,” tech. rep., Los Alamos National Lab.(LANL), Los Alamos, NM (United States), 2006.
- [77] E. Bair, T. Hastie, D. Paul, and R. Tibshirani, “Prediction by supervised principal components,” *Journal of the American Statistical Association*, vol. 101, no. 473, pp. 119–137, 2006.

- [78] J. Gill, “The insignificance of null hypothesis significance testing,” *Political Research Quarterly*, vol. 52, no. 3, pp. 647–674, 1999.
- [79] H. Akaike, “A new look at the statistical model identification,” *IEEE transactions on automatic control*, vol. 19, no. 6, pp. 716–723, 1974.
- [80] G. Schwarz *et al.*, “Estimating the dimension of a model,” *The annals of statistics*, vol. 6, no. 2, pp. 461–464, 1978.
- [81] E. Barshan, A. Ghodsi, Z. Azimifar, and M. Z. Jahromi, “Supervised principal component analysis: Visualization, classification and regression on subspaces and submanifolds,” *Pattern Recognition*, vol. 44, no. 7, pp. 1357–1371, 2011.
- [82] A. Gretton, O. Bousquet, A. Smola, and B. Schölkopf, “Measuring statistical dependence with hilbert-schmidt norms,” in *International conference on algorithmic learning theory*, pp. 63–77, Springer, 2005.
- [83] C. R. Turner, A. Fuggetta, L. Lavazza, and A. L. Wolf, “A conceptual basis for feature engineering,” *Journal of Systems and Software*, vol. 49, no. 1, pp. 3–15, 1999.
- [84] J. C. Kim, S. E. Anderson, W. Kaye, F. Zhang, Y. Zhu, S. J. Kaye, and Z. He, “Charge sharing in common-grid pixelated cdznte detectors,” *Nuclear Instruments and Methods in Physics Research Section A: Accelerators, Spectrometers, Detectors and Associated Equipment*, vol. 654, no. 1, pp. 233–243, 2011.
- [85] C. H. Chen, W. R. Cook, F. A. Harrison, J. Y. Lin, P. H. Mao, and S. M. Schindler, “Characterization of the heft cdznte pixel detectors,” in *Hard X-Ray and Gamma-Ray Detector Physics V*, vol. 5198, pp. 9–19, International Society for Optics and Photonics, 2004.
- [86] A. Hyvärinen and E. Oja, “Independent component analysis: algorithms and applications,” *Neural networks*, vol. 13, no. 4-5, pp. 411–430, 2000.
- [87] S. Lombard, T. Isenhour, P. Heintz, G. Woodruff, and W. Wilson, “Neutron-capture gamma-ray activation analysis. design of apparatus for trace analysis,” *The International Journal of Applied Radiation and Isotopes*, vol. 19, no. 1, pp. 15–22, 1968.
- [88] R. Henkelmann and H. Born, “Analytical use of neutron-capture gamma-rays,” *Journal of Radioanalytical and Nuclear Chemistry*, vol. 16, no. 2, pp. 473–481, 1973.
- [89] M. P. Failey, D. L. Anderson, W. H. Zoller, G. E. Gordon, and R. M. Lindstrom, “Neutron-capture prompt. gamma.-ray activation analysis for multielement determination in complex samples,” *Analytical Chemistry*, vol. 51, no. 13, pp. 2209–2221, 1979.

- [90] J. Polf, S. Peterson, M. McCleskey, B. Roeder, A. Spiridon, S. Beddar, and L. Trache, “Measurement and calculation of characteristic prompt gamma ray spectra emitted during proton irradiation,” *Physics in Medicine & Biology*, vol. 54, no. 22, p. N519, 2009.
- [91] J. C. Polf, S. Avery, D. S. Mackin, and S. Beddar, “Imaging of prompt gamma rays emitted during delivery of clinical proton beams with a compton camera: feasibility studies for range verification,” *Physics in Medicine & Biology*, vol. 60, no. 18, p. 7085, 2015.
- [92] W. Van Roosbroeck, “Theory of the yield and fano factor of electron-hole pairs generated in semiconductors by high-energy particles,” *Physical review*, vol. 139, no. 5A, p. A1702, 1965.
- [93] A. Owens, “Spectral degradation effects in an 86 cm<sup>3</sup> ge (hp) detector,” *Nuclear Instruments and Methods in Physics Research Section A: Accelerators, Spectrometers, Detectors and Associated Equipment*, vol. 238, no. 2-3, pp. 473–478, 1985.
- [94] F. Zhang, W. R. Kaye, and Z. He, “Performance of 3-d position sensitive cdznte detectors for gamma-ray energies above 1 mev,” in *Nuclear Science Symposium Conference Record (NSS/MIC), 2009 IEEE*, pp. 2012–2016, IEEE, 2009.
- [95] J. T. Dirk Meier, *VAD\_UM2 Preliminary Datasheet for CDR*. Integrated Detector Electronics AS.
- [96] S. Agostinelli, J. Allison, K. a. Amako, J. Apostolakis, H. Araujo, P. Arce, M. Asai, D. Axen, S. Banerjee, G. . Barrand, *et al.*, “Geant4a simulation toolkit,” *Nuclear instruments and methods in physics research section A: Accelerators, Spectrometers, Detectors and Associated Equipment*, vol. 506, no. 3, pp. 250–303, 2003.
- [97] M. Asai, G. Cosmo, A. Dotti, L. Garnier, I. Hrivnácová, S. Incerti, V. Ivantchenko, A. Ribon, M. Verderi, and D. H. Wright, “Geant4 version 10 series,” in *Joint International Conference on Mathematics and Computation, Supercomputing in Nuclear Applications and the Monte Carlo Methods*, 2015.
- [98] J. Apostolakis, M. Pia, S. Giani, P. Nieminen, M. Maire, and L. Urban, “Geant4 low energy electromagnetic models for electrons and photons,” tech. rep., 1999.
- [99] B. Efron and R. J. Tibshirani, *An introduction to the bootstrap*. CRC press, 1994.
- [100] D. Hong, L. Balzano, and J. A. Fessler, “Asymptotic performance of pca for high-dimensional heteroscedastic data,” *Journal of Multivariate Analysis*, vol. 167, pp. 435–452, 2018.

- [101] S. J. Devlin, R. Gnanadesikan, and J. R. Kettenring, “Robust estimation of dispersion matrices and principal components,” *Journal of the American Statistical Association*, vol. 76, no. 374, pp. 354–362, 1981.